Characterization of a 1D magic wavelength lattice for increasing the coherence time of Rydberg superatoms

Jan Adrianus de Haan

Masterarbeit in Physik
angefertigt im Institut für Angewandte Physik

vorgelegt der
Mathematisch-Naturwissenschaftlichen Fakultät
der
Rheinischen Friedrich-Wilhelms-Universität
Bonn

Oktober 2024

I hereby declare that this thesis was formulated by myself and that no sources or tools other than those cited were used.

Bonn, ...
Date Signature

1. Gutachter: Prof. Dr. Sebastian Hofferberth
2. Gutachter: Prof. Dr. Michael Köhl

Contents

Introduction

Rydberg superatoms are ensembles of many ultracold atoms that act as a single quantum two-level system, that is strongly coupled to light and emits light into the mode from which it was excited [1]. These properties make them interesting for applications in nonlinear quantum optics and quantum information [2]. To be useful for these applications, the coupling of the superatom to light must exceed the decay and dephasing rates of the superatom.

In this thesis, different aspects of the influence of a 1D magic wavelength lattice trap on the dephasing rate of Rydberg superatoms are characterized: Inhomogeneous differential light shifts in the trap, thermal movement of the atoms, and density-dependent dephasing effects.

In chapter 1, Rydberg superatoms are introduced, the thermal dephasing of their collective excited state is calculated, and how a standing wave trap can prevent this dephasing. The experimental setup in which the superatoms are created and which contains the standing wave trap is described.

The details of trapping Rydberg atoms in this standing wave trap are discussed in the following chapter 2. The trap potentials for the ground and Rydberg state are calculated, and the impossibility of making such a trap perfectly magic by choosing the trap wavelength, i.e. completely equating the trap potentials for the two states, is discussed. Nonetheless there is an optimal wavelength for the trap, and how it may be found experimentally is the topic of the remainder of the chapter. A simple spectroscopic method is discussed, but found to not be suitable for this purpose. Instead, photon storage experiments enable finding the optimal wavelength, and are found to be sensitive enough to differences of the trap potentials for the two states to measure the difference of optimal detunings for two different trap geometries, an effect specific to magic trapping of Rydberg atoms.

During the photon storage measurements made to determine the optimal trap wavelength, it became apparent that the density of the atom cloud has a large influence on the dephasing rate. These density-dependent effects are investigated in chapter 3, where measurements of the influence of molecular states of one Rydberg atom and one ground state atom on photon storage experiments at lower principal quantum numbers and of density-dependent dephasing at higher principal quantum numbers are discussed.

Finally in chapter 4, the coherence times of Rydberg superatoms in the standing wave trap and the optical trap used so far are compared. An attempt at a quantitative summary of the so far known dephasing effects in the two different traps is given.

CHAPTER 1

Rydberg superatoms in a 1D lattice trap

1.1 Rydberg superatoms for waveguide QED

Atoms whose valence electron is excited to a state with high principal quantum number n are called Rydberg atoms. In Rydberg S-states, atoms interact strongly via van der Waals interactions, with an interaction potential given by $V(r) = C_6/r^6$ at a separation r. The strong interaction causes an effect called the Rydberg blockade: Within a volume containing many atoms, a laser cannot excite more than one of them to the Rydberg state at once. In this blockaded volume, the energy shift of the Rydberg state due to the interaction potential is larger than the effective excitation bandwidth Ω_{eff}, preventing more than one Rydberg excitation. The size of the blockade volume is reduced for higher excitation bandwidth, which can be caused by e.g. power-broadening, the laser linewidth, and the collective enhancement of the Rabi frequency. A measure for the size of this region is the blockade radius $r_b = (\hbar\Omega_{\text{eff}}/C_6)^{1/6}$. It can reach values of more than 10 µm for large principal quantum numbers of around $n = 100$ [3, 2].

The Rydberg blockade enables the creation of a Rydberg superatom: A cloud of N_b atoms excited to Rydberg states, all of them located inside the Rydberg blockaded volume. This makes the cloud act as an effective two-level system, with collective ground and excited states. Because the superatom consists of many atoms, it can interact with light more strongly than a single atom could. This leads to an enhancement of the frequency of Rabi oscillations between these states by a factor $\sqrt{N_b}$ [4]. Using a superatom consisting of a large number of atoms makes it possible to increase the atom-light coupling to a level where few-photon light pulses can drive these collective Rabi oscillations. In addition, the phase of the exciting light is imprinted in the atomic excitation, causing directional emission of light into the mode which excited the superatom [1].

A Rydberg superatom interacting with a few-photon light field may be described by a simple effective model involving only three states, which is described in detail in refs. [2, 5]. This model describes the superatom in the terms of waveguide quantum-electrodynamics (waveguide QED), where a two-level system, called an emitter, is coupled to the electric field in a waveguide with a coupling rate κ. This is possible even though there is no waveguide, just a superatom in free space, because light is emitted by the superatom back into the exciting mode. The model and its prediction for the effect of a single superatom on a few-photon driving field is briefly summarized here.

We call the ground state of the atoms of which the superatom is made $|g\rangle$ and their Rydberg state $|r\rangle$. The driving field has the phase $e^{i\vec{k}\cdot\vec{r}}$ at the location $\vec{r}$ and a photon rate R_{in}. The internal states of the

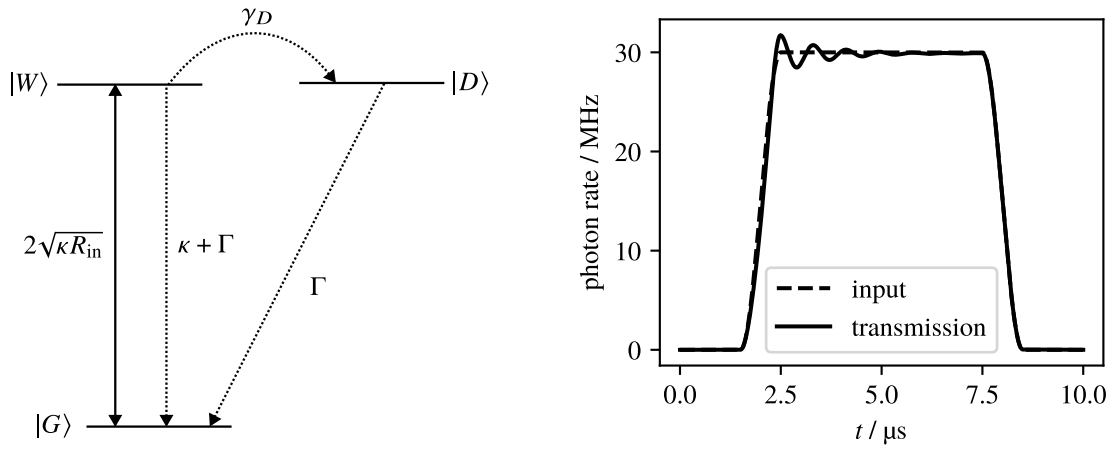

Figure 1.1: Left: Level scheme of the effective model of a superatom, showing the collective ground, excited, and dark states $|G\rangle$, $|W\rangle$, and $|D\rangle$, with coupling by light between the ground and excited state at rate $2\sqrt{\kappa R_{\text{in}}}$, decay of excitations at rate Γ for the dark state and the enhanced rate $\Gamma + \kappa$ for the bright state, and dephasing of the collective excited state into the dark state at rate γ_D. Right: Predicted oscillations of the transmitted photon rate due to Rabi oscillations between $|G\rangle$ and $|W\rangle$ caused by driving with a Tukey-shaped input light pulse, as predicted by eq. 1.4. Parameters: $\kappa = 0.5\,\text{MHz}$, $\Gamma = 0.1\,\text{MHz}$, $\gamma_D = 1\,\text{MHz}$.

superatom are called $|G\rangle$, $|W\rangle$, and $|D\rangle$. In the collective ground state $|G\rangle = |g_1, \ldots, g_{N_b}\rangle$, all atoms are in their ground state. In the collective excited state

$$|W\rangle = \sum_{i=1}^{N_b} e^{i\vec{k}\cdot\vec{r}_i} |g_1, \ldots, r_i, \ldots, g_{N_b}\rangle\,, \tag{1.1}$$

the system is in a a superposition of all singly-excited states. The phase between the different singly-excited states is that of the exciting light field, here a plane wave with position-dependent phase $e^{i\vec{k}\cdot\vec{r}_i}$ at the location $\vec{r}_i$ of the atom i. When the Rydberg state is excited by two-photon excitation, $\vec{k}$ is the effective wave vector for the two fields used (see section 1.3 for details). The phase relation between the constituent states of the superposition state $|W\rangle$ is crucial for its properties: It leads to light being emitted preferentially back into the exciting mode [6]. For this reason $|W\rangle$ is called the bright state. States in which there is a single Rydberg excitation, but that do not emit photons preferentially into the exciting mode are called dark states. In the model, all of them are described by a single dark state $|D\rangle$.

The collective nature of the bright state $|W\rangle$ leads to enhanced coupling to light: If a single atom performs Rabi oscillations between $|g\rangle$ and $|r\rangle$ with Rabi frequency Ω_R, Rabi oscillations between the collective states $|G\rangle$ and $|W\rangle$ will occur at the enhanced Rabi frequency $\Omega_{\text{col}} = \sqrt{N_b}\Omega_R$ [7]. The enhanced Rabi frequency depends on the strength of the coupling rate κ to the light field, and the amount of light, given by the photon rate R_{in} of the exciting mode. Decay of the Rydberg state at rate Γ causes decay of the collective excited states into the ground state at this rate. While this spontaneous decay leads to the emission of photons into many spatial modes, there is also an enhanced decay of the collective excited state into the ground state at rate κ, in which photons are emitted back into the mode that excited the superatom. When the Rydberg excitation does not decay, but the relative phases of the singly-excited

states making up the superposition state $|W\rangle$ change, it dephases into the collective dark state $|D\rangle$. The rate of this process is called γ_D, and there are many possible reasons for it to occur.

A level scheme of this model is shown in the left panel of figure 1.1, and its Hamiltonian is

$$\hat{H}/\hbar = \delta\hat{\sigma}_{WW} + \delta\hat{\sigma_{DD}} + \sqrt{\kappa R_{\text{in}}}(\hat{\sigma}_{GW} + \hat{\sigma}^{\dagger}_{GW}). \tag{1.2}$$

using $\sigma_{ij} = |i\rangle\langle j|$. δ is the detuning of the exciting laser from the Rydberg transition. For $\delta = 0$, the populations of the system described by this Hamiltonian perform Rabi oscillations between $|G\rangle$ and $|W\rangle$ at the Rabi frequency $2\sqrt{\kappa R_{\text{in}}}$. The decays may be modeled using a Lindblad master equation (see e.g. ref. [8]), which in full is

$$\frac{\mathrm{d}\hat{\rho}}{\mathrm{d}t} = -\frac{i}{\hbar}[\hat{H}, \hat{\rho}] + (\kappa + \Gamma)D[\hat{\sigma}_{WG}]\hat{\rho} + \Gamma D[\hat{\sigma}_{DG}]\hat{\rho} + \gamma_D D[\hat{\sigma}_{WD}]\hat{\rho} \tag{1.3}$$

with the Lindblad superoperator $D[\hat{O}]\hat{\rho} = \hat{O}\hat{\rho}\hat{O}^{\dagger} - \frac{1}{2}(\hat{O}^{\dagger}\hat{O}\hat{\rho} + \hat{\rho}\hat{O}^{\dagger}\hat{O})$.

Rabi oscillations between $|G\rangle$ and $|W\rangle$ lead to oscillations of the transmitted photon rate, which is given by [2, eq. 49]

$$R_{\text{out}} = |\alpha(t)|^2 + \kappa\langle\hat{\sigma}^{\dagger}_{GW}(t)\hat{\sigma}_{GW}(t)\rangle - i\sqrt{\kappa}\left[\alpha^*(t)\langle\hat{\sigma}_{GW}(t)\rangle - \alpha(t)\langle\hat{\sigma}^{\dagger}_{GW}(t)\rangle\right] \tag{1.4}$$

where $\alpha(t)$ is proportional to the expectation value of the electric field. It is related to the input photon rate by $R_{\text{in}}(t) = |\alpha(t)|^2$. The expectation values needed to compute the outgoing photon rate are obtained by numerically solving the Lindblad master equation using the Python package Qutip [9, 10]. The result is shown in the right panel of figure 1.1 for parameters that are currently achievable in the experiment.

From the parameters κ, Γ, and γ_D, the ratio of emission back into the input mode and into other modes may be defined as $\beta_{\text{coh}} = \frac{\kappa}{\kappa+\gamma_D+\Gamma}$ [2]. This number quantifies the duration of coherent evolution of the system, allowing the comparison of different physical systems that may all be described as emitters coupled to a waveguide. Ideally, β_{coh} is close to 1. So far, in the Rubidium Quantum Optics experiment described in section 1.3, $\beta_{\text{coh}} \approx 0.23$ has been achieved, at $\kappa = 0.428\,\text{MHz}$, $\Gamma = 0.069\,\text{MHz}$, and $\gamma_D = 1.397\,\text{MHz}$ [1]. In order to increase β_{coh}, it is necessary to either increase κ or to decrease γ_D or Γ.

The coupling rate κ can be increased by using a superatom made of more atoms. However, it is not possible to increase the number of atoms too much, because all atoms must be within the Rydberg blockade radius, and large densities lead to decoherence [11], increasing γ_D. Alternatively, the dephasing rate γ_D may be reduced by combating dominant dephasing mechanisms.

1.2 Reduction of thermal dephasing by confining atomic motion

Thermal dephasing is expected to be the most important dephasing mechanism present in the RQO experiment [1, p. 3]. To calculate its effect, we follow ref. [12]. It is caused by movement of the atoms that are part of the superposition state $|W\rangle$. In order to emit light into the exciting mode, the atomic phases must match those of the exciting field. This is the defining property of the bright state $|W\rangle$, and when the atoms change their position, different atomic phases are required for emission to occur into the exciting mode. The effective model only considers the internal states of the atoms and therefore has only a single bright state, where the atomic phases match the phases of the light field at the positions of the atoms. If we considered the external state of the atoms as well, there would be many bright states, one

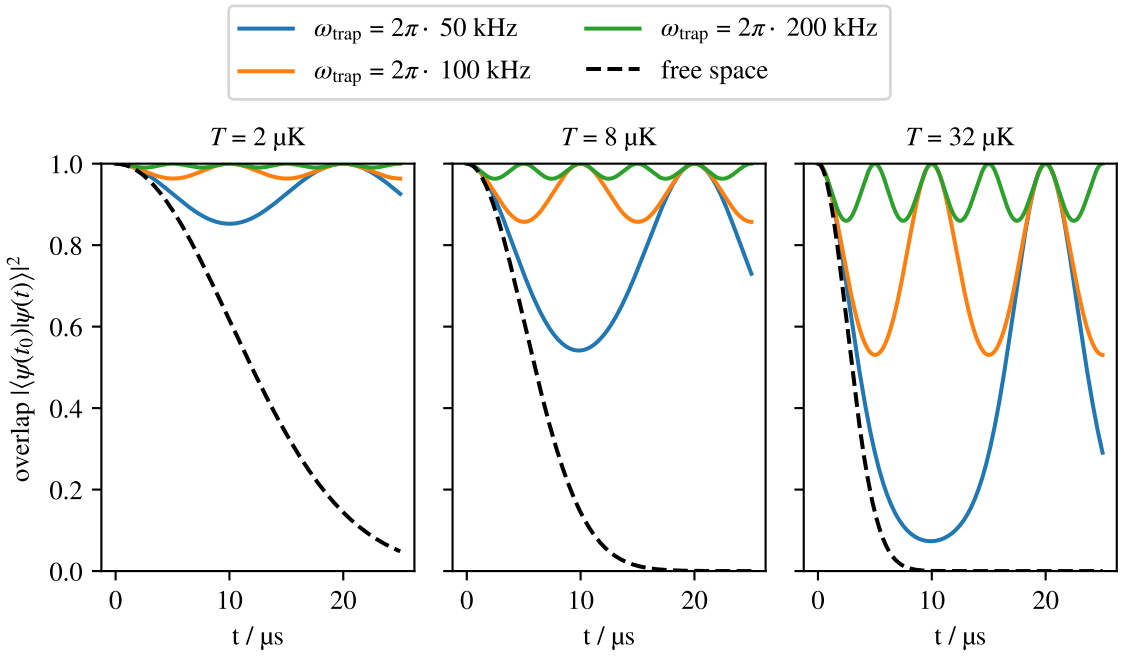

Figure 1.2: Comparison of the overlap of the bright states for the initial positions of the atoms and for their positions after thermal movement, at different temperatures. Free movement, which leads to Gaussian decay, is compared to movement in harmonic traps of different trap frequencies, where all atoms return to their original positions after one oscillation period.

for each set of positions of the atoms, in which the atomic phases match the phases of the light field at the atoms' positions. The movement of the atoms does not affect their internal state, but for the locations where the atoms have moved, the bright state has a different internal state. We calculate the overlap of the internal states of the required bright state at the new atomic positions and the actual internal state of the atoms, which is that of the bright state at their initial positions.

We choose the direction of the exciting light to be $\vec{k} = k\hat{e}_y$. The distribution of the velocity component in the y-direction is given by the Boltzmann distribution as

$$P(v_y) = \sqrt{\frac{m}{2\pi k_B T}} \exp\left(-\frac{m}{2k_B T} v_y^2\right).$$

The bright state for the location of the atoms at time t is

$$|\psi(t)\rangle = \sum_{i=1}^{N_b} e^{i\vec{k}\cdot\vec{r}_i(t)} \, |g_1, \ldots, r_i, \ldots, g_{N_b}\rangle$$

with $\vec{k} \cdot \vec{r}_i(t) = k(y(0) + v_{i,y}t)$, so $|\psi(0)\rangle = |W\rangle$. The sum can be replaced with an integral over the distribution of velocities, $\frac{1}{\sqrt{N_b}} \sum_i f(v_{y,i}) \mapsto \int \mathrm{d}v_y \, P(v_y) f(v_y)$. The overlap with the bright state for

the location of the atoms at time 0 is

$$
\begin{aligned}
|\langle\psi(0)|\psi(t)\rangle|^2 &= \left|\sum_{i=1}^{N_b} e^{-iky(0)} \langle g_1,\ldots,r_i,\ldots,g_{N_b}| \sum_{j=1}^{N_b} e^{ik(y(0)+v_{j,y}t)} |g_1,\ldots,r_j,\ldots,g_{N_b}\rangle\right|^2 \\
&= \left|\sum_{i=1}^{N_b} e^{ikv_{i,y}t}\right|^2 = \left|\int \mathrm{d}v_y\, P(v_y) e^{ikv_y t}\right|^2 = \exp\left(-\frac{k_B T}{m} k^2 t^2\right) \\
&= \exp\left(-t^2/\tau_T^2\right)
\end{aligned}
$$

with $\tau_T = \sqrt{\frac{m}{k^2 k_B T}}$. The overlap with the bright state for the new atom locations exhibits a Gaussian decay, which is shown in figure 1.2 for different temperatures and the excitation configuration described in section 1.3.

This decay into the dark state can be reduced by confining the atomic motion along the direction of the exciting light, which is possible using a 1D lattice trap. Instead of moving away ever further from their initial position, the atoms in each lattice site oscillate around their initial position.

We calculate the trap depth required to achieve a certain reduction of the thermal dephasing rate. To do this, the overlap of the bright state for the atoms at their initial positions with the bright state for the atoms at their new positions is calculated just like in the free space case, but assuming classical harmonic motion along the y-direction in a trap with trap frequency ω_{trap}.

For simplicity, the calculation is done by numerically sampling the Boltzmann distribution. The position of an atom of energy E_i with initial motional phase ϕ_i in the harmonic trap is given by $y_i(t) = A_i \sin\left(\omega_{\mathrm{trap}} t + \phi_i\right)$. At time 0, the position of the atom is $y_i(0) = \sin(\phi_i)$. The overlap of the bright state at the initial atomic positions, $|\psi(0)\rangle$ and at the positions at time t, $|\psi(t)\rangle$, is

$$
\begin{aligned}
f_{T,\omega_{\mathrm{trap}}}(t) = |\langle\psi(0)|\psi(t)\rangle|^2 &= \left|\sum_{i=1}^{N_b} e^{ikA(E_i)(\sin\left(\omega_{\mathrm{trap}} t+\phi_i\right)-\sin(\phi_i))}\right|^2 \\
&= \left|\int \mathrm{d}E\, P(E) \int \mathrm{d}\phi\, P(\phi) e^{ikA(E)[\sin\left(\omega_{\mathrm{trap}} t+\phi\right)-\sin(\phi)]}\right|^2 .
\end{aligned}
$$

for distributions $P(E)$ and $P(\phi)$ of the energies of the atoms and their initial phases. The amplitude of the motion of an atom with energy E is given by $A(E) = 2E/(m\omega_{\mathrm{trap}}^2)$.

The overlap $|\langle\psi(0)|\psi(t)\rangle|^2$ is evaluated numerically for a discretized Boltzmann distribution $P(E) \propto \exp\left(-\frac{E}{k_B T}\right)$ and a discretized uniform random distribution of initial phases $P(\phi)$. The results are shown in figure 1.2 for different trap frequencies and temperatures.

Initially, the overlap decays just like in free space. The reason for this is that it takes some time until the motion in free space and in the trap differ significantly due to the trapping force. While in free space, the atoms move ever further away from their initial positions, causing the Gaussian decay to zero overlap, the movement of trapped atoms away from their initial positions is slowed and then inverted. Because the trap is harmonic, the period of the motion is the same for all amplitudes, so all atoms return to their initial positions at the same time, leading to a full rephasing: The overlap returns to 1. Even though a complete rephasing always happens in a harmonic trap, how small the overlap becomes between rephasing events

depends on how far the atoms can move in the trap. To achieve consistently large overlaps with the initial state, the trap must be as deep as possible. The higher the temperature of the atoms, the deeper the trap has to be to confine their motion to an amplitude that leads to an acceptable maximal dephasing between rephasing events.

Such a harmonic potential along the propagation direction of the exciting light can be created using an optical standing wave trap made of two counterpropagating laser beams. Because the $\cos^2(k_t y)$-shaped potential is only approximately harmonic near the potential minima, a deeper trap will show behavior closer to the ideal case calculated above, while a shallower trap will not lead to perfect rephasing, because the period after which each atom returns to its original position will depend on the amplitude of the motion.

1.3 Experimental setup

This section describes the experimental setup of the RQO experiment, in which Rydberg superatoms made of ultracold clouds of Rubidium-87 can be created and in which the standing wave trap for slowing their thermal dephasing is implemented. The setup is quite complex, but since it already existed prior to the work on this thesis, we refer to earlier theses [13, 14, 15] for details instead of trying to comprehensively describe it here. Beam waist sizes are the $1/e^2$ intensity radius.

A heavily simplified sketch of the experimental setup is shown in figure 1.3. Rb-87 atoms are loaded from a background gas using a magneto-optical trap (not shown), they are cooled and loaded into a crossed-beam optical dipole trap (two beams at 1064 nm with $w_0 \approx 50\,\mu\text{m}$, of orthogonal polarization to avoid the formation of a standing wave, which would cause rapid heating of atoms when turning this trap on and off, crossing at an angle between the two beams of $2 \cdot 31.4^\circ$ – not shown in the sketch), producing a cigar-shaped cloud (sketched) of atoms at a few µK (characterizations of the temperature and atom number are done in section 3.1). This atom cloud may be transferred into other optical traps before any measurements are performed.

There are two other optical traps available. The first one is the so-called dimple trap, consisting of a variable number of cylindrical beams at 805 nm (taller in the z-direction, $w_{0,z} = 28.8\,\mu\text{m}$, than wide in the y-direction, $w_{0,y} = 7.5\,\mu\text{m}$), which allow reducing the size of the cloud in the y-direction, to make the cloud behave as a Rydberg superatom [16]. In this thesis, only a single dimple beam is ever used. The second trap, which has only been implemented in the experiment recently, is a standing wave trap at 1012 nm running along the y-axis, with $w_0 = 24.8\,\mu\text{m}$. It tightly confines the atoms along the y-direction, i.e. along the direction of the effective wave vector of the Rydberg excitation, as shown in figure 1.4.

The standing wave trap should prevent thermal dephasing as described in section 1.2. It is formed by reflecting the trapping beam back onto itself. Due to the glass chamber walls and various optical elements in the path of the trapping light, the power in the backward propagating beam is 87 % of the power in the forward propagating beam. When the trapping beam is blocked behind the chamber, there is no retroreflection and no standing wave anymore, but only a running wave, which still provides confinement in the x- and z-directions, but only very little in the y-direction. Atoms may be loaded from the dimple trap into the standing wave trap to produce an ensemble small in the y-direction, or the atoms may be loaded into the standing wave trap directly from the crossed beam optical dipole trap, which creates a cloud that is long in the y-direction. Depending on whether we want to work with an ensemble that is completely blockaded by a single Rydberg excitation or not, either of these two possibilities may be used. In addition to these two traps, the crossed beam trap used for the preparation of the atom cloud

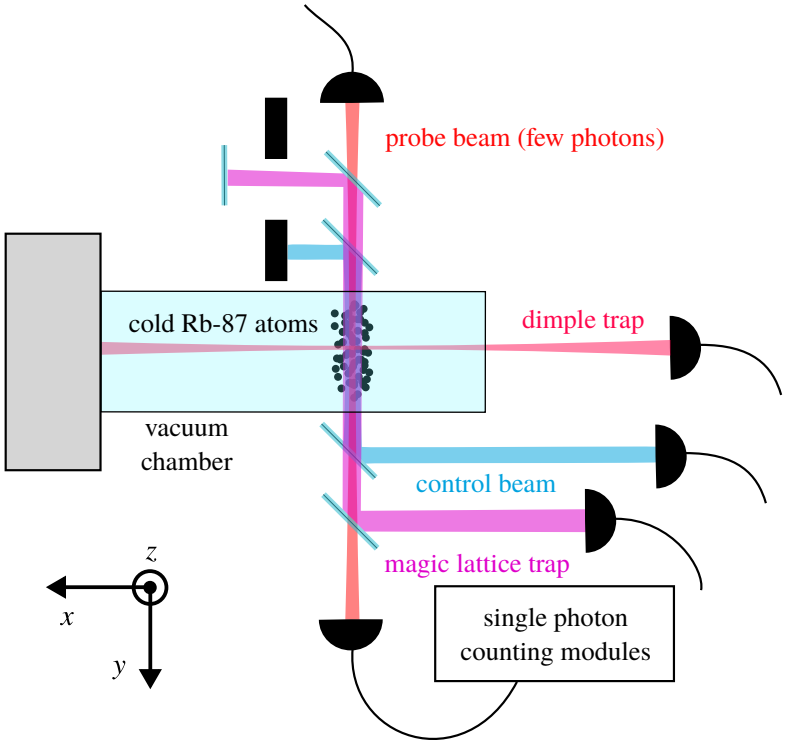

Figure 1.3: The experimental setup produces an ultracold Rb-87 gas in a vacuum chamber, prepared in the ground state $|g\rangle$, that is excited to Rydberg states using a strong control field and a weak probe field. From the initially loaded cigar shaped cloud, clouds smaller than the Rydberg blockade radius along the propagation axis of the probe beam (y-axis) may be prepared using a cylindrical so-called dimple trap. During superatom experiments, confinement along the y-axis is provided by either keeping the dimple trap on, or by loading to the lattice trap. Photon storage experiments may be performed using such a small completely Rydberg-blockaded ensemble, or directly using the initially prepared large cloud, which is then loaded into the running wave or lattice trap. For the running wave trap, the crossed-beam dipole trap (not shown) in which the initial cloud is prepared is used to confine the atoms between experiments.

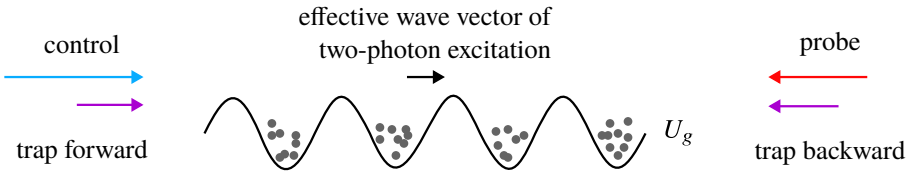

Figure 1.4: This figure visualizes the atom distribution along the y-axis and the lattice trap potential U_g for the ground state, in whose minima the atoms are confined. The wave vectors of the trapping beams, of the counterpropagating Rydberg excitation beams, and the effective wave vector of the two-photon Rydberg excitation process are shown.

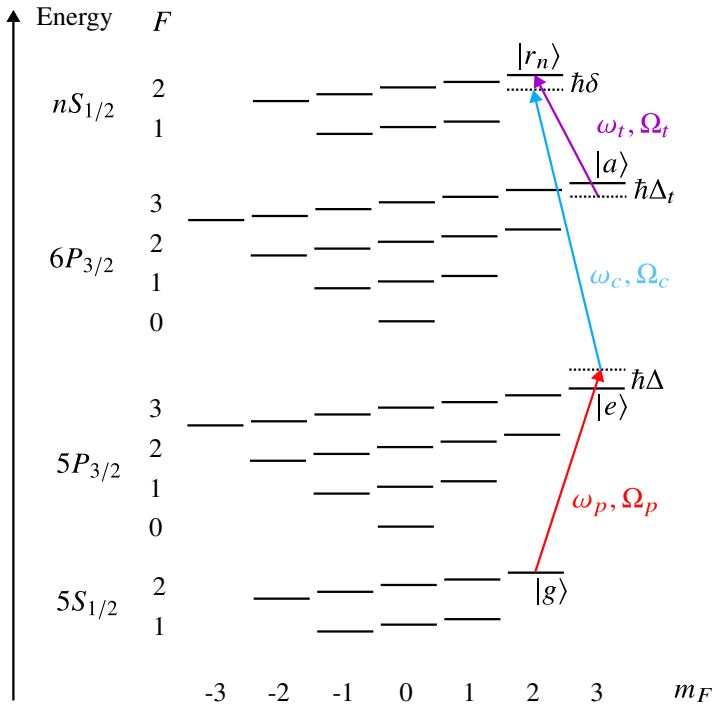

Figure 1.5: This figure shows relevant levels of Rb-87 and the lasers used in the experiment. A magnetic bias field $\vec{B} = B\hat{e}_y$ in the y-direction is applied, and the quantization axis is chosen along this axis. The states used are the hyperfine ground state $|g\rangle = |5S_{1/2}, F = 2, m_F = 2\rangle$, in which the atoms are prepared, the intermediate state $|e\rangle = |5P_{3/2}, F = 3, m_F = 3\rangle$, the Rydberg state $|r_n\rangle = |nS_{1/2}, F = 2, m_F = 2\rangle$, and the auxiliary state $|a\rangle = \left|6P_{3/2}, F = 3, m_F = 3\right\rangle$, which is used to trap the atoms in the Rydberg state. The Rydberg state $|r_n\rangle$ is excited using a two-photon Raman transition via the intermediate state $|e\rangle$, with a weak probe laser with Rabi frequency Ω_p and a strong control laser with Rabi frequency Ω_c, where the single-photon detuning of the probe and control lasers from the intermediate state is $\pm\Delta$, and the two-photon detuning from the Rydberg state energy is δ. The trapping laser is close to resonant to the $|a\rangle$ to $|r_n\rangle$ transition, with detuning Δ_t.

may also be turned on between experiments to provide additional confinement.

In summary, five different combinations of traps and atom clouds are used in this thesis: A large cloud in free space, a large cloud in the standing wave trap, a large cloud in the running wave trap, a small cloud in the dimple trap, and a small cloud in the standing wave trap. The latter two are called the dimple and lattice dimple configurations.

The atoms in the cloud are initially prepared in the ground state $|g\rangle$ and excited to the Rydberg state $|r_n\rangle$ using a probe laser at 780 nm with $w_0 = 5\,\mu$m and a control laser at 480 nm with $w_0 \approx 45.1\,\mu$m. The probe needs to be very tightly focused to only excite atoms within the Rydberg blockade radius. The states and light polarizations used are shown in the level scheme in figure 1.5. The two lasers are counterpropagating, so for the ladder level scheme used for Rydberg excitation, the effective wave vector for the two-photon excitation is

$$\vec{k} = \vec{k}_{\text{probe}} + \vec{k}_{\text{control}} = (k_{\text{control}} - k_{\text{probe}})\hat{e}_y \approx \hat{e}_y \frac{2\pi}{1.25\,\mu\text{m}}, \tag{1.5}$$

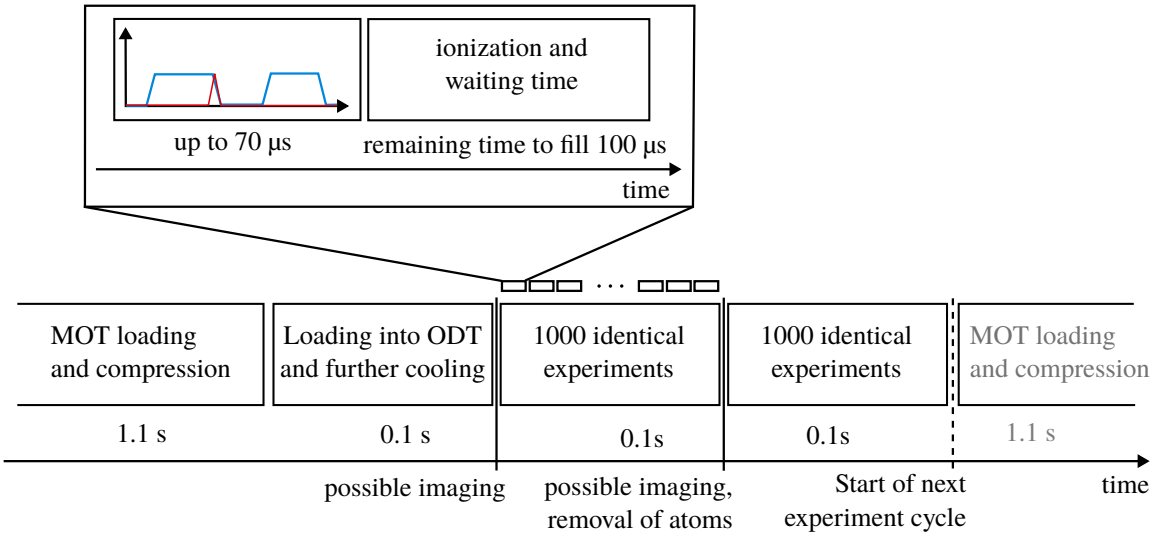

Figure 1.6: Overview of the experiment sequence, consisting of loading Rb-87 atoms from a background gas into a MOT, compressing and transferring the atomic cloud into an optical dipole trap, further cooling it using Raman sideband cooling and evaporative cooling, and using the ultracold cloud for repeated experiments, each consisting of few-photon probe pulses and possibly Rydberg excitation. During the individual experiments, the dipole trap used to load the cloud of atoms and to confine it between experiments is turned off. After each experiment, Rydberg atoms are ionized, and there is some waiting time until the ionization fields have vanished.

so this configuration reduces the effect of motional dephasing compared to copropagating excitation beams, where the effective wave vector would have a magnitude of $\frac{2\pi}{0.30\,\mu\text{m}}$ [17].

While the control beam contains a classical amount of light, the probe beam is attenuated to the few-photon regime. The probe beam is coupled into a single-mode fiber behind the chamber, which distributes the light onto four single photon counting modules. The beams on the y-axis are overlaid with dichroic mirrors.

There are magnetic field coils around the chamber used to apply bias fields during experiments, and there are electrodes inside the chamber for controlling the static electric field and ionizing Rydberg atoms, which is at the moment only used to remove unwanted Rydberg excitations before another experiment starts.

An outline of the experimental sequence is shown in figure 1.6. After preparation of the cloud in the optical traps already described, many identical experiments are performed with the same cloud, since only few probe photons are counted in each experiment, and many repetitions are needed to gather sufficient statistics. Before each experiment, the crossed beam dipole trap is usually turned off. For experiments in the standing wave trap, the crossed beam trap is not turned on again at all, since the standing wave trap provides sufficient confinement. For experiments in the dimple trap or in free space, it is necessary to turn on the crossed beam trap between experiments to avoid losing too many atoms. Each experiment takes 10 µs to 70 µs, where probe light is sent into the cloud and detected, and possibly control light to excite the atoms to the Rydberg state. Pulse shaping is done with acousto-optical modulators. Afterwards, any Rydberg atoms that have been created during the experiment are ionized, and there is some waiting time to ensure the electric fields have settled and all ions are gone. In total,

each repetition takes 100 µs, and there are 1000 repetitions, taking 100 ms overall.

Afterwards, all traps are turned off and the atoms are lost by evaporation and because they fall out of the excitation region under gravity. The same experimental sequence of 1000 repetitions is run again, to be used as reference measurements.

Absorption images may be taken directly after loading and after the repeated measurements, to characterize the atom number and temperature of the atom cloud before and after the experiments (see section 3.1).

The details of trapping not just the ground, but also the Rydberg state in the lattice trap, are treated in chapter 2.

CHAPTER 2

Spectroscopy and photon storage in a magic trap

In section 1.2, the possibility of using a standing wave trap to reduce thermal dephasing has been introduced. Another source of dephasing are inhomogeneous differential light shifts between the ground and Rydberg state. To avoid these in the standing wave trap, it should have the same trap potential for the ground and Rydberg state. Because off-resonant dipole traps rely on broad optical transitions, but optical transitions to Rydberg states are in comparison very narrow, it is necessary to use a trap wavelength that is almost resonant with such a narrow optical transition. In the RQO experiment, this is the $|a\rangle$ to $|r_n\rangle$ transition, as shown in figure 1.5. The detuning of the trap laser from this transition is called Δ_t. The exact choice of the trap detuning Δ_t determines whether the standing wave trap is magic for the ground and Rydberg states.

In this chapter, we investigate whether it is possible to completely equalize the trapping potentials for atoms in ground and Rydberg states in the standing wave trap. Because we will find from calculations that the optimal trap detuning is geometry-dependent, a comparison with a running wave, which is easily implemented in the experiment, is performed. Experimental methods for finding the optimal trap detuning are compared.

We begin by computing the trapping potentials for the ground and Rydberg state, and find that the potential for atoms in the Rydberg state does not have the same shape as the intensity distribution, but is given by a spatial average of the intensity distribution weighed by the Rydberg electron wavefunction, making it impossible to completely equate it to the ground state atom trapping potential (section 2.1).

Then, two methods for determining the trap wavelength at which the trapping potentials for the ground and Rydberg state atoms are as similar as possible are investigated: The shift and broadening of the absorption line observed in spectroscopy of the ground to Rydberg state transition, which is found to be, under the conditions used, unsuitable for finding the optimal lattice wavelength (section 2.2), and photon storage experiments, whose sensitivity to the spatial variance of differential light shifts allows measuring the difference in optimal trap laser wavelengths between a running wave and standing wave trap geometry (section 2.3).

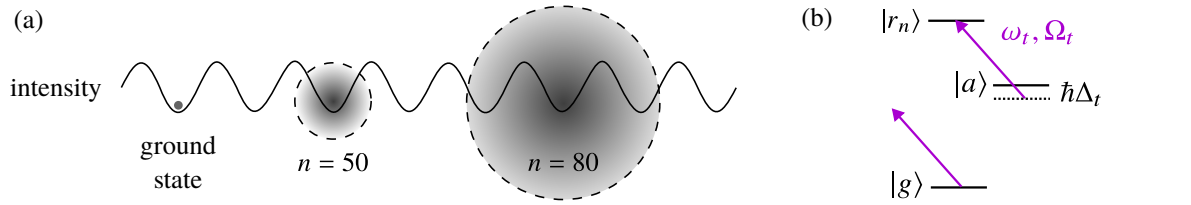

Figure 2.1: (a) This sketch shows a ground state atom and Rydberg atoms at different principal quantum numbers n to scale with the intensity of the standing wave trap, whose minima are separated by 0.5 µm. (b) Level scheme showing the ground state $|g\rangle$, the Rydberg state $|r_n\rangle$, and the auxiliary state $|a\rangle$ that is used to trap the Rydberg state.

2.1 Trap potential calculation

The trapping potential for an Alkali atom in the ground state in a laser beam far-detuned from any transition has the same shape as the intensity [18]

$$U_g(\vec{r}) = -\frac{1}{4}\alpha_g |\vec{E}(\vec{r})|^2.$$

The proportionality factor α_g between the square of the electric field amplitude and the trap potential is the AC-polarizability. However, when the atom is excited to a Rydberg state, the electron wavefunction may become comparable in size to distances over which the intensity of the trapping light changes significantly. A sketch of this situation in the standing wave trap used in the experiment is shown in figure 2.1(a). In this case, the dipole approximation, in which the atom is treated as a point with a dipole moment interacting with the electric field only at that point, breaks down. The calculation of the trapping potential without making the dipole approximation has been done for a standing wave in ref. [19]. Here, the derivation is repeated, some steps are spelled out, and simple general formulas for the trapping potential of a Rydberg atom in a laser field are given.

Since the calculation of the trapping potential for atoms in Rydberg states as done in refs. [19, 20] makes use of the Floquet formalism of quasi-energy states, the relevant parts of it are briefly summarized, and the perturbative energy shifts in the formalism are derived in detail (section 2.1.1), and are then applied to the calculation of the trapping potential.

We want to calculate the potentials for the ground state $|g\rangle$ and for the Rydberg state $|r_n\rangle$ for atoms in a trapping laser beam with electric field $\vec{E}(\vec{r},t) = E(\vec{r})\vec{\epsilon}e^{i\omega_t t}$ with polarization $\vec{\epsilon}$ and amplitude $E(\vec{r})$. The atom is treated quantum mechanically, and the electromagnetic field is treated classically, using the minimal coupling Hamiltonian with the vector potential $\vec{A}(\vec{r},t)$ and the scalar potential $\phi(\vec{r},t)$. In the Coulomb gauge, the scalar potential ϕ is given by only the core potential, the contribution from the trapping field is 0. The vector potential is given by only the trap laser beam's electric field, as

$\vec{A}(\vec{r},t) = \frac{ic}{\omega_t}E(\vec{r})\vec{\epsilon}\cos(\omega_t t)$. The total Hamiltonian operator is

$$\begin{aligned}\hat{H}(t) &= \frac{1}{2m_e}(\hat{\vec{p}} - \frac{e}{c}\vec{A}(\vec{r},t))^2 + e\phi(\vec{r},t) \\ &= \frac{\hat{\vec{p}}^2}{2m_e} + e\phi(\vec{r},t) - \frac{e}{m_e c}\hat{\vec{p}}\cdot\vec{A}(\vec{r},t) + \frac{e^2}{2m_e c^2}|\vec{A}(\vec{r},t)|^2 \\ &= \hat{H}_0 + \hat{V}_1(t) + \hat{V}_2(t) \end{aligned} \tag{2.1}$$

In the expanded form of the Hamiltonian, the first two terms are exactly the Hamiltonian $H_0 = \frac{\hat{\vec{p}}^2}{2m} + e\phi(\vec{r},t)$ of the Rb-87 atom with known eigenstates. The last two terms

$$V_1(t) = -\frac{e}{m_e c}\hat{\vec{p}}\cdot\vec{A}(\vec{r},t) \tag{2.2}$$

and

$$V_2 = \frac{e^2}{2m_e c^2}|\vec{A}(\vec{r},t)|^2 \tag{2.3}$$

may be treated as perturbations to H_0, and will give the trapping potential due to the laser field.

The straightforward application of time-independent perturbation theory is not possible, because of the time-dependence of $\vec{A}(\vec{r},t)$. However, due to the periodicity of the laser field, it is possible to reduce the problem to a time-independent one, using the Floquet theory of quasi-energy states.

2.1.1 Calculation of energy shifts for a dressed atom with Floquet theory

In general, the Schrödinger equation for a time-dependent Hamiltonian cannot be solved as easily as in the case of a time-independent Hamiltonian. However, if the Hamiltonian is periodic with period $T = 2\pi/\omega$, it can be written as a Fourier series $\hat{H} = \sum_n \hat{H}^n e^{in\omega t}$. It is then possible to find solutions in close analogy to the time-independent case. This approach to solving the Schrödinger equation for a time-dependent Hamiltonian is described in refs. [21, 22]. The result is repeated here, and then perturbation theory is applied to find energy shifts for the case at hand.

Choosing as the basis to work in the unperturbed states of H_0, $\psi_\beta^{(0)}$ with energies $E_\beta^{(0)}$, and labeling the components in this basis by greek letters, it is possible to Fourier-decompose the T-periodic Hamiltonian: $H_{\alpha\beta}(t) = \sum_n H^n_{\alpha\beta} e^{in\omega t}$. The Fourier components are labeled with latin letters.

We would like to solve the Schrödinger equation

$$i\hbar\frac{\partial\psi(t)}{\partial t} = \hat{H}(t)\psi(t) \tag{2.4}$$

with the Hamiltonian from eq. 2.1. We treat one perturbation at a time, and look at the Hamiltonian $\hat{H}(t) = \hat{H}_0 + \hat{V}(t)$, where $\hat{V}$ can be $\hat{V}_1$ or $\hat{V}_2$. We label the solutions of the Schrödinger eq. 2.4 $\psi_\beta(t)$. The components in the basis of unperturbed solutions are called $F_{\alpha\beta}(t)$, and fulfill $\psi_\beta(t) = \sum_\alpha F_{\alpha\beta}(t)\psi_\beta^{(0)}$.

The components of the Hamiltonian are $H_{\alpha\beta}(t) = E_\alpha^{(0)}\delta_{\alpha\beta} + V_{\alpha\beta}(t)$. The Fourier components of the perturbation are $V_{\alpha\beta}(t) = \sum_n V^n_{\alpha\beta} e^{i\omega nt}$. Since H_0 is time-independent, its only nonzero Fourier

component is the one for $n = 0$, and it is diagonal in the unperturbed basis, so $(H_0)^0_{\alpha\beta} = \delta_{\alpha\beta}E^{(0)}_\alpha$. Thus the Fourier components of the total Hamiltonian are $H^n_{\alpha\beta} = \delta_{\alpha\beta}\delta_{n0}E^{(0)}_\alpha + V^n_{\alpha\beta}$.

From ref. [22], the solutions of the Schrödinger eq. 2.4 may be obtained by solving the eigenvalue problem

$$q_\beta F^n_{\alpha\beta} = \sum_{\gamma,k}(H^{n-k}_{\alpha\gamma} + n\omega\delta_{\alpha\gamma}\delta_{k,n})F^k_{\gamma\beta} \tag{2.5}$$

for the so-called quasi-energies q_α. The full set of solutions consists of one quasi-energy for each value of β, and state vector components $F_{\alpha\beta}(t)$ with Fourier components $F^k_{\alpha\beta}$. Explicitly, the solutions of the original eq. 2.4 are then given by

$$\psi_\beta(t) = \sum_\alpha e^{-iq_\alpha t/\hbar}\psi_{\alpha\beta}(t)\psi^{(0)}_\alpha = \sum_\alpha e^{-iq_\alpha t/\hbar}\sum_n e^{in\omega t}\psi^n_{\alpha\beta}\psi^{(0)}_\alpha \tag{2.6}$$

From this expression, it is clear why q_α is called quasi-energy: It gives a part of the time-evolution in analogy to the energy in a time-independent system, but only gives a unique time-evolution up to changes of multiples of $\hbar\omega$ – when replacing $q_\alpha \mapsto q_\alpha + m\hbar\omega$, the expression on the right hand side of eq. 2.6 does not change because of the sum over all n.

Upon inserting the Fourier components of our Hamiltonian into eq. 2.5, it becomes

$$q_\beta F^n_{\alpha\beta} = \sum_{\gamma,k}(E^{(0)}_\alpha\delta_{\alpha\gamma}\delta_{n-k,0} + V^n_{\alpha\gamma} + n\omega\delta_{\alpha\gamma}\delta_{k,n})F^k_{\gamma\beta} = E^{(0)}_\alpha F^n_{\alpha\beta} + \sum_{\gamma,k}(V^n_{\alpha\gamma} + n\omega\delta_{\alpha\gamma}\delta_{k,n})F^k_{\gamma\beta}$$

or

$$(q_\beta - E^{(0)}_\alpha - n\omega)F^n_{\alpha\beta} = \sum_{\gamma,k}V^n_{\alpha\gamma}F^k_{\gamma\beta}. \tag{2.7}$$

This equation is very similar to the one that comes up in time-independent perturbation theory, as described in component form e.g. in ref. [23], and can be solved in the same way. The calculation has been carried out in detail in appendix A. It results in the first and second order shifts of the quasi-energy:

$$q^{(1)}_\beta = V^0_{\beta\beta} \tag{2.8}$$

$$q^{(2)}_\beta = \sum_{\gamma\neq\beta,k}\frac{(V^k_{\gamma\beta})^2}{E^{(0)}_\beta - E^{(0)}_\gamma - k\omega} \tag{2.9}$$

These results may be interpreted in the dressed atom picture, in which the energy term $q_\beta + n\hbar\omega$ is the total energy of an atom in a field with n photons [22]. These results are also used in the usual derivation of the optical trapping potential [18].

The interpretation of these energy corrections is aided by the following calculation of the mean value of a periodic function $f(t) = \sum_n f_n e^{in\omega t}$ times $e^{-iq\omega t}$ over its period $T = 2\pi/\omega$ in terms of its Fourier

components:

$$\frac{1}{T}\int_0^T f(t)e^{-iq\omega t}\,\mathrm{d}t = \frac{1}{T}\sum_n f_n \int_0^T e^{i(n-q)\omega t}\,\mathrm{d}t$$
$$= \sum_n f_n \delta_{q+n,0} = f_q$$

The Fourier component f_q is the average value of the function f over its period in a frame rotating at $q\omega$. Thus one can interpret the quasi-energy shifts computed using Floquet theory as involving the averages of the perturbation matrix elements in rotating frames closest to the transition frequency between relevant states.

Without any perturbation, the quasi-energies are the same as the unperturbed energies, $q_\beta = E_\beta^{(0)}$. The quasi-energy shifts $q_\beta^{(1)}$ and $q_\beta^{(2)}$ are the potential for an atom initially in state $\psi_\beta^{(0)}$. In the dipole approximation, they give the usual optical potentials [18]. We can now use them to compute the optical potential for Rydberg states without making the dipole approximation for the $\vec{A}^2$-term, where it is not justified.

2.1.2 $\vec{A}\cdot\hat{\vec{p}}$ term

We evaluate eqs. 2.8 and 2.9 for $V_1(t) = -\frac{ie}{m\omega_t}\vec{E}(\vec{r})\hat{\vec{p}}\cdot\vec{\epsilon}\cos(\omega_t t)$. Thus the first-order correction, involving V^0, is zero. In the perturbation sum for the second-order correction, we need to calculate the matrix elements $\langle\gamma|V^1|\beta\rangle$. In this case, we can make the dipole approximation, because only matrix elements where at least one of the states is a low-lying state will be relevant (this argument is taken directly from ref. [19, p. 2]). For the ground state, this is because transitions to low-lying states are the only relevant contributors, so the spatial extent of all wavefunctions involved is smaller than the lengths over which significant intensity variations occur. For the Rydberg state, only the matrix element between $|r_n\rangle$ and $|a\rangle$ will be relevant. The Rydberg state electron wavefunction might be comparable in size to the lengths over which intensity fluctuations occur, but the electron wavefunction in the low-lying $|a\rangle$ state is not, and in the matrix element the overlap is what counts.

When the dipole approximation can be made, the perturbation $V_1(t) = -\frac{ie}{m\omega_t}\vec{E}(\vec{r})\hat{\vec{p}}\cdot\vec{\epsilon}\cos(\omega_t t) = -\frac{1}{m_e c}\hat{\vec{p}}\cdot\vec{A}$ is the same as $V_1(t) = -\hat{\vec{d}}\cdot\vec{E}(\vec{r})\cos(\omega_t t)$ [24]. The only nonzero Fourier components of the Hamiltonian in the dipole approximation are $V_1^{\pm 1} = -\frac{1}{2}\hat{\vec{d}}\cdot\vec{E}(\vec{r})$.

For the ground state shift, there are relevant contributions from many low-lying states, the most important ones from the $D1$ and $D2$ lines, as described e.g. in [18], where the same expression for the energy shift

$$q_g^{(2)} = \sum_{\gamma,k}\frac{(V_{\gamma g}^k)^2}{E_g^{(0)} - E_\gamma^{(0)} - k\omega_t}$$

is given. The shift may be expressed using the ground-state polarizability $\alpha_g/h \approx 6.20\times10^{-7}\,\mathrm{Hz/(V/m)^2}$

(calculated using the ARC Python package [25]) at $\lambda_t \approx 1012\,\mathrm{nm}$ as

$$q_g^{(2)} = -\frac{1}{4}\alpha_g E(\vec{r})^2.$$

The factor $1/4$ occurs because the ground state polarizability is defined such that the energy shift for a field $E(\vec{r},t)$ is $-\frac{1}{2}\alpha_g \overline{E(\vec{r},t)^2}$. The overline denotes the time-average over one period, but $E(\vec{r})$ is the amplitude of the field, and the two are related by a factor $1/2$:

$$\overline{E(\vec{r},t)^2} = \frac{1}{T}\int_0^T E(\vec{r},t)^2\,\mathrm{d}t = \frac{1}{T}\int_0^T \left(E(\vec{r})\cos(2\pi t/T)\right)^2\,\mathrm{d}t = \frac{E(\vec{r})^2}{2}$$

For the Rydberg state, only the contribution from the $|a\rangle$ state is relevant, because the trapping laser is tuned close to the $|a\rangle$ to $|r_n\rangle$ resonance ($\Delta_t/2\pi$ is at most about 1 GHz), so $E_{r_n}^{(0)} - E_a^{(0)} - \hbar\omega_t = \hbar\Delta_t \ll E_\beta^{(0)} - E_\gamma^{(0)} - k\omega_t$ for any other states $|\beta\rangle$ and $|\gamma\rangle$ and any k. We thus have

$$\begin{aligned} q_r^{(2)} &= \sum_{\gamma\neq r, k\in\mathbb{N}} \frac{(V_{\gamma r}^k)^2}{E_r^{(0)} - E_\gamma^{(0)} - k\hbar\omega_t} = \sum_k \frac{(V_{ar}^k)^2}{E_r^{(0)} - E_a^{(0)} - k\hbar\omega_t} \\ &= \frac{(V_{ar}^1)}{(E_r^{(0)} - E_a^{(0)}) - \hbar\omega_t} = -\frac{V_{ar}^{(1)}}{\hbar\Delta_t} \\ &= -\frac{|\langle a|\hat{\vec{d}}\cdot\vec{\epsilon}|r_n\rangle|^2}{4\hbar\Delta_t}E^2(\vec{r}). \end{aligned}$$

The minus sign occurs because $|r_n\rangle$ is a higher-lying state than $|a\rangle$, and the detuning of the trap laser frequency ω_t from the transition frequency ω_0 is conventionally defined as $\Delta_t = \omega_t - \omega_0$, i.e. such that it is negative for red-detuned light. For red-detuned light, the potential for the lower state is attractive toward higher intensity, and the excited state is repelled, and vice-versa for blue-detuned light. For σ^--polarized light and using the J-reduced [1] dipole matrix element D_n, we have $\langle a|\hat{\vec{d}}\cdot\vec{\epsilon}|r_n\rangle = \frac{1}{2}D_n$. The contribution to the potential of the Rydberg state due to the V_1 term is thus

$$q_r^{(2)} = -\frac{1}{16}\frac{D_n^2}{\hbar\Delta_t}E^2(\vec{r}). \tag{2.10}$$

2.1.3 $\vec{A}^2$ term

Again, we evaluate eqs. 2.8 and 2.9, this time for $V_2 = \frac{e^2}{2m_e c^2}|\vec{A}(\vec{r},t)|^2$. Inserting $\vec{A}(\vec{r},t) = \frac{ic}{\omega_t}\vec{\epsilon}E(\vec{r})\cos(\omega_t t)$ gives

$$V_2 = \frac{e^2}{8m_e\omega_t^2}E^2(\vec{r})(2 + e^{2i\omega_t t} + e^{-2i\omega_t t}) = -\frac{1}{8}\alpha_f E^2(\vec{r})(2 + e^{2i\omega_t t} + e^{-2i\omega_t t}),$$

[1] this is the matrix element that may be calculated in ARC using `ARC.getReducedMatrixElementJ(6,1,3/2,n,0,1/2)` (note the convention used by ARC is different from the one used by e.g. Steck)

having introduced the polarizability of the free electron in the trap laser field, $\alpha_f = -\frac{e^2}{m\omega_t^2}$. It is always negative, the free electron is repulsed by the light. Intuitively, the free electron polarizability corresponds to periodic motion of the electron in an oscillating field. The amplitude of the motion gets larger when the field amplitude increases. This causes the electron to be repulsed from regions of high intensity, because it leads to a larger energy of the electron in a higher intensity field. The resulting potential is called the ponderomotive potential. The nonzero Fourier components are $V_2^0 = -\frac{\alpha_f}{2}E(\vec{r})$ and $V_2^{\pm 2} = -\frac{\alpha_f}{4}E^2(\vec{r})$. Only the first-order correction to the energy is computed, because it is already of second order in the field strength, i.e. of the same order as the correction computed for the dipole term.

For the ground state, the $\vec{A}^2$-term is not relevant: Only the contribution from the $\vec{A}\cdot\hat{\vec{p}}$-term, which is also the only contribution given in ref. [18], is relevant. Reasons for this are beyond the scope of this calculation.

For the Ryberg state, one has to average the intensity weighed by the wavefunction.

$$q_r^{(1)} = -\frac{\alpha_f}{4}\left\langle r_n\middle|E^2(\vec{R}+\vec{r}_e)\middle|r_n\right\rangle = -\frac{\alpha_f}{4}\int \mathrm{d}^3 r_e\, |\psi_n(\vec{r})|^2 E^2(\vec{R}+\vec{r}_e) \tag{2.11}$$

This leads to a dependence of the trap potential on the intensity around the Rydberg atom core, which depends on the exact trap geometry. In some cases, the average in eq. 2.11 may be performed analytically, but in other cases it must be computed numerically. Calculating such an average in practice is treated in section 4.2.

2.1.4 Summary of trap potentials for ground and Rydberg state

In summary, the total energy shifts for the ground state due to the $\vec{A}\cdot\hat{\vec{p}}$ term and for the Rydberg state due to the $\vec{A}\cdot\hat{\vec{p}}$ and $\vec{A}^2$ terms are given here. In general, since the Rydberg state shift depends not only on a single intensity value, only the energy shift, not the shift per intensity is given.

$$U_g(\vec{r}) = -\frac{1}{4}\alpha_g E^2(\vec{r}) \tag{2.12}$$

$$U_r(\vec{r}) = -\frac{1}{16}\frac{D_n^2}{\hbar\Delta_t}E^2(\vec{r}) - \frac{\alpha_f}{4}\left\langle r_n\middle|E^2(\vec{r}+\vec{r}_e)\middle|r_n\right\rangle \tag{2.13}$$

The matrix element is given by

$$\left\langle r_n\middle|E^2(\vec{r}+\vec{r}_e)\middle|r_n\right\rangle = \int \mathrm{d}^3 r_e\, |\psi_{r_n}(\vec{r}_e)|^2 E^2(\vec{r}+\vec{r}_e),$$

where ψ_{r_n} is the wavefunction of the Rydberg state r_n.

2.1.5 Potentials for running and standing wave traps

For some intensity distributions, calculating the trap potentials requires numerical evaluation of eqs. 2.10 and 2.11. For the simple case of a running and standing wave (see figure 2.2), it is however possible to proceed analytically, which gives some insight into the conditions under which one can expect to make a magic trap, and also serves as a sanity check for numerical calculations.

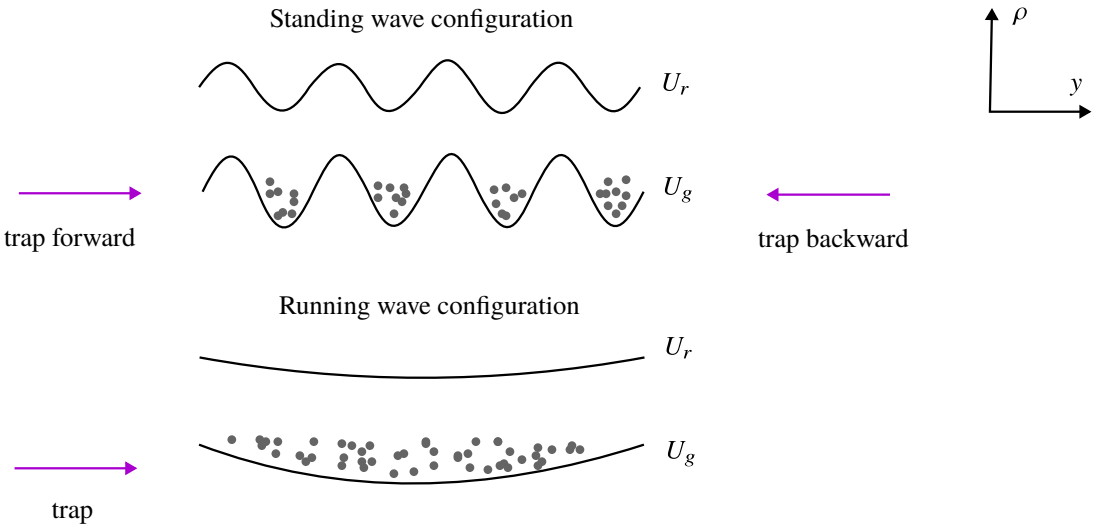

Figure 2.2: This figure shows the trap potentials in the case of a standing wave, where the trapping beam is retroreflected (top), and in the case of a running wave, where this is not done (bottom). The atom density distribution is sketched in the ground state potentials along the y-direction.

The standing wave trap in the experiment is formed by interfering a Gaussian beam with its reflection. The waists and waist positions of the two beams are very similar and are taken to be identical in the following calculation. The forward-propagating (backward-propagating) Gaussian beam along the y-direction, whose polarization $\vec{\epsilon}$ is left-handed circular (right-handed circular), corresponding to σ^-, is given by the electric field $\vec{E}_\pm = \mathrm{Re}(\vec{\epsilon} E_\pm)$. In cylindrical coordinates along the y-axis, ρ being the radial coordinate,

$$E_\pm(\rho, y) = E_{0,\pm} \frac{w_0}{w(y)} e^{-\rho^2/w^2(y)} e^{ik_t \rho^2/(2R(y))} e^{\pm i k_t y - i\eta(y)}$$

where

$$w(y) = w_0 \sqrt{1 + (y/y_0)^2}$$

is the beam radius at y, w_0 is the waist of the beam, and $y_0 = \pi w_0^2/\lambda$ is the Rayleigh range. We neglect the Gouy phase $\eta(y)$ and the phase due to the wavefront curvature $R(y)$, since the atoms will be trapped close to the focus of the beam, where these terms are small. Thus we have

$$E_\pm(\rho, y) \approx E_{0,\pm} \frac{w_0}{w(y)} e^{-\rho^2/w^2(y)} e^{\pm i k_t y}$$

We define the amplitudes $A_\pm(\rho, y) = E_{0,\pm} \frac{w_0}{w(y)} e^{-\rho^2/w^2(y)}$ such that $E_\pm(\rho, y) = A_\pm(\rho, y) e^{\pm i k_t y}$. Since a phase shift between E_+ and E_- only shifts the position of the standing wave minima and maxima, we assume the phase shift to be zero, and $A_\pm$ to both be real. The standing wave intensity is proportional to

(not writing out the ρ and y dependence of $A_\pm$ from here on)

$$|E_+(\rho,y)+E_-(\rho,y)|^2 = 4A_+A_-\cos^2(k_t y)+(A_+-A_-)^2.$$

The running wave intensity is proportional to

$$|E_+(\rho,y)|^2 = |A_+|^2.$$

For the Rydberg state, the total potential is

$$U_r(\vec{r}) = -\frac{1}{16}\frac{D_n^2}{\hbar\Delta_t}E^2(\vec{r}) - \frac{\alpha_f}{4}\left\langle r_n\middle|E^2(\vec{r}+\vec{r}_e)\middle|r_n\right\rangle$$

To perform the average $\left\langle r_n\middle|E^2(\vec{r}+\vec{r}_e)\middle|r_n\right\rangle$, it is useful to introduce the landscape factor $\theta_n = \left\langle r_n\middle|\cos(2ky_e)\middle|r_n\right\rangle$. Since the Rydberg electron probability density in an S-state is symmetric in the y-direction, and sin is antisymmetric, the integral $\left\langle r_n\middle|\sin(2ky_e)\middle|r_n\right\rangle$ is 0. Writing $\cos^2(k_t(y+y_e)) = \frac{1}{2}(1+\cos(2k_t y)\cos(2k_t y_e)-\sin(2k_t y)\sin(2k_t y_e))$, we find

$$\begin{aligned}
-\frac{1}{4}\alpha_f\left\langle r_n\middle|E^2(\vec{r}+\vec{r}_e)\middle|r_n\right\rangle &= -\frac{1}{4}\alpha_f\left\langle r_n\middle|4A_+A_-\cos^2(k_t(y+y_e))+(A_+-A_-)^2\middle|r_n\right\rangle \\
&= -\frac{1}{4}\alpha_f\left\langle r_n\middle|2A_+A_-(1+\cos(2k_t y)\cos(2k_t y_e)-\sin(2k_t y)\sin(2k_t y_e))+(A_+-A_-)^2\middle|r_n\right\rangle \\
&= -\frac{\alpha_f}{2}A_+A_-(1+\theta_n\cos(2k_t y))-\frac{\alpha_f}{4}(A_+-A_-)^2 \\
&= -\frac{\alpha_f}{2}A_+A_-\theta_n(2\cos^2(k_t y)-1)-\frac{\alpha_f}{2}A_+A_- - \frac{\alpha_f}{4}(A_+-A_-)^2 \\
&= -\alpha_f A_+A_-\theta_n\cos^2(k_t y)-\frac{\alpha_f}{2}(1-\theta_n)A_+A_- - \frac{\alpha_f}{4}(A_+-A_-)^2
\end{aligned}$$

Since the amplitudes $A_\pm$ by themselves only vary on scales much larger than the Rydberg wavefunction, it is not necessary to average over them. Overall, we have the standing wave potential for the Rydberg state

$$U_{r,sw}(\vec{r}) = -\frac{1}{16}\frac{D_n^2}{\hbar\Delta_t}(4A_+A_-\cos^2(k_t y)+(A_+-A_-)^2)-\alpha_f A_+A_-\theta_n\cos^2(k_t y)-\frac{\alpha_f}{2}(1-\theta_n)A_+A_- - \frac{\alpha_f}{4}(A_+-A_-)^2. \tag{2.14}$$

This consists of terms that involve a factor $\cos^2(k_t y)$, which are periodic in the y-direction, and other terms that do not. We separate these terms, with the periodic part of the potential (denoted by $\sim$) being

$$U^{\sim}_{r,sw}(\vec{r}) = -\left(\frac{D_n^2}{4\hbar\Delta_t}+\alpha_f\theta_n\right)A_+A_-\cos^2(k_t y) \tag{2.15}$$

and the non-periodic part (denoted by −) being

$$U^{-}_{r,sw}(\vec{r}) = -\left(\frac{D_n^2}{16\hbar\Delta_t} + \frac{\alpha_f}{4}\right)(A_+ - A_-)^2 - \frac{\alpha_f}{2}(1-\theta_n)A_+A_-. \tag{2.16}$$

For the ground state, the trapping potential is

$$U_g(\vec{r}) = -\frac{1}{4}\alpha_g E^2(\vec{r}) = -\alpha_g A_+A_- \cos^2(k_t y) - \frac{\alpha_g}{4}(A_+ - A_-)^2. \tag{2.17}$$

The periodic part is given by

$$U^{\sim}_{g,sw}(\vec{r}) = -\alpha_g A_+A_- \cos^2(k_t y) \tag{2.18}$$

and the non-periodic part is given by

$$U^{-}_{g,sw}(\vec{r}) = -\frac{\alpha_g}{4}(A_+ - A_-)^2. \tag{2.19}$$

2.1.6 Magic trap detunings

In a magic trap, we would like to choose Δ_t such that $U_{g,sw} = U_{r,sw}$. This is however not possible. What is possible is to equate the periodic parts of the potential, $U^{\sim}_{g,sw} = U^{\sim}_{r,sw}$, which leads to the condition

$$\alpha_g = \frac{D_n^2}{4\hbar\Delta_t} + \alpha_f\theta_n$$

which is fulfilled for

$$\hbar\Delta_t = \frac{D_n^2}{4(\alpha_g - \theta_n\alpha_f)} \tag{2.20}$$

For 1012 nm light, the ground state polarizability α_g is positive. α_f is negative, so the magic detuning is positive, i.e. the trap laser needs to be blue-detuned with respect to the $|a\rangle$ to $|r_n\rangle$ transition, as expected to balance the anti-trapping ponderomotive potential for an excited state. If this is done, the non-periodic parts still differ:

$$U^{-}_{r,sw} - U^{-}_{g,sw} = -\frac{\alpha_f}{4}(1-\theta_n)(A_+^2 + A_-^2)$$

At this condition, the trap is therefore not fully magic.

For the running wave, we can simply set $A_- = 0$ to obtain the relevant trapping potentials. No distinction between a periodic and a non-periodic part is made, since there is no periodic part of the potential.

$$U_{g,rw}(\vec{r}) = -\frac{\alpha_g}{4}A_+^2 \tag{2.21}$$

$$U_{r,rw}(\vec{r}) = -\left(\frac{D_n^2}{16\hbar\Delta_t} + \frac{\alpha_f}{4}\right) A_+^2 \tag{2.22}$$

In this case, it is possible to completely equate the potentials, which leads to the condition

$$\frac{D_n^2}{16\hbar\Delta_t} + \frac{\alpha_f}{4} = \frac{\alpha_g}{4}$$

which is fulfilled for

$$\hbar\Delta_t = \frac{D_n^2}{4(\alpha_g - \alpha_f)} \tag{2.23}$$

Discussion The difference between this magic detuning for the running wave (eq. 2.23) and the one for the standing wave (eq. 2.20) is given by the landscape factor θ_n, which is 1 when intensity variations only occur on scales much larger than the electron wavefunction, and takes other values greater than 0 otherwise.

These results are the same as those of the same calculation in ref. [19], except for a factor of 4 because of a different convention for the amplitudes $A_\pm$, and a difference of the $\vec{A}\cdot\hat{\vec{p}}$ contribution, which is $D_n^2/(6\hbar\Delta_t)$ in ref. [19] instead of $D_n^2/(4\hbar\Delta_t)$ in our case due to different light polarization[2].

The computation of the landscape factor $\theta_n = \langle r_n|\cos(2ky_e)|r_n\rangle = \int \mathrm{d}^3 r_e\, |\psi_n(\vec{r}_e)|^2 \cos(2ky_e)$ may be done efficiently by expanding it in terms of Bessel functions (also from ref. [19]). We have compared the approximation to a brute-force 3D numerical integration, the two give results within an expected numerical error.

In figure 2.3, the trapping potential differences between the ground and Rydberg state according to the final equations in section 2.1.5 are shown, for our experimental parameters and principal quantum number $n = 94$ of the Rydberg state. The potentials for the ground and Rydberg state have been computed for a few different trap detunings, including the magic detuning for just the periodic part of the standing wave potential and the magic detuning for the running wave. From the ground state potentials, which are almost constant over this range of trap detunings, the extent of the atom cloud in the trap is computed. It is shown in the figure with dashed lines. From the figure one can estimate that the optimal detuning for the standing wave trap is between the magic detunings for the running wave and standing wave.

To determine the value of this optimal trap detuning, the variance of the differential light shifts experienced by the atoms is computed. The variance shown for the different traps in figure 2.4. As expected from the definition of a magic detuning, the variance becomes zero at the magic detunings for the running wave and the periodic part of the standing wave. While the magic detunings only depend on the trap parameters, the optimal trap detuning in the standing wave also depends on the position of the atoms. This may be seen in principle using a contrived example by looking at figure 2.3: For a theoretical string of atoms located only at $\rho = 0$, the magic detuning for the periodic part of the standing wave potential would yield the smallest variance, while for a string of atoms only at $y = 0$, the magic detuning for the nonperiodic part of the standing wave would yield the smallest variance. One might thus expect the optimal trap detuning to depend on the temperature of the atoms, which determines up to where they fill the lattice sites.

[2] Ref. [19] uses linearly polarized light, requiring an average over different Clebsch-Gordan coefficients

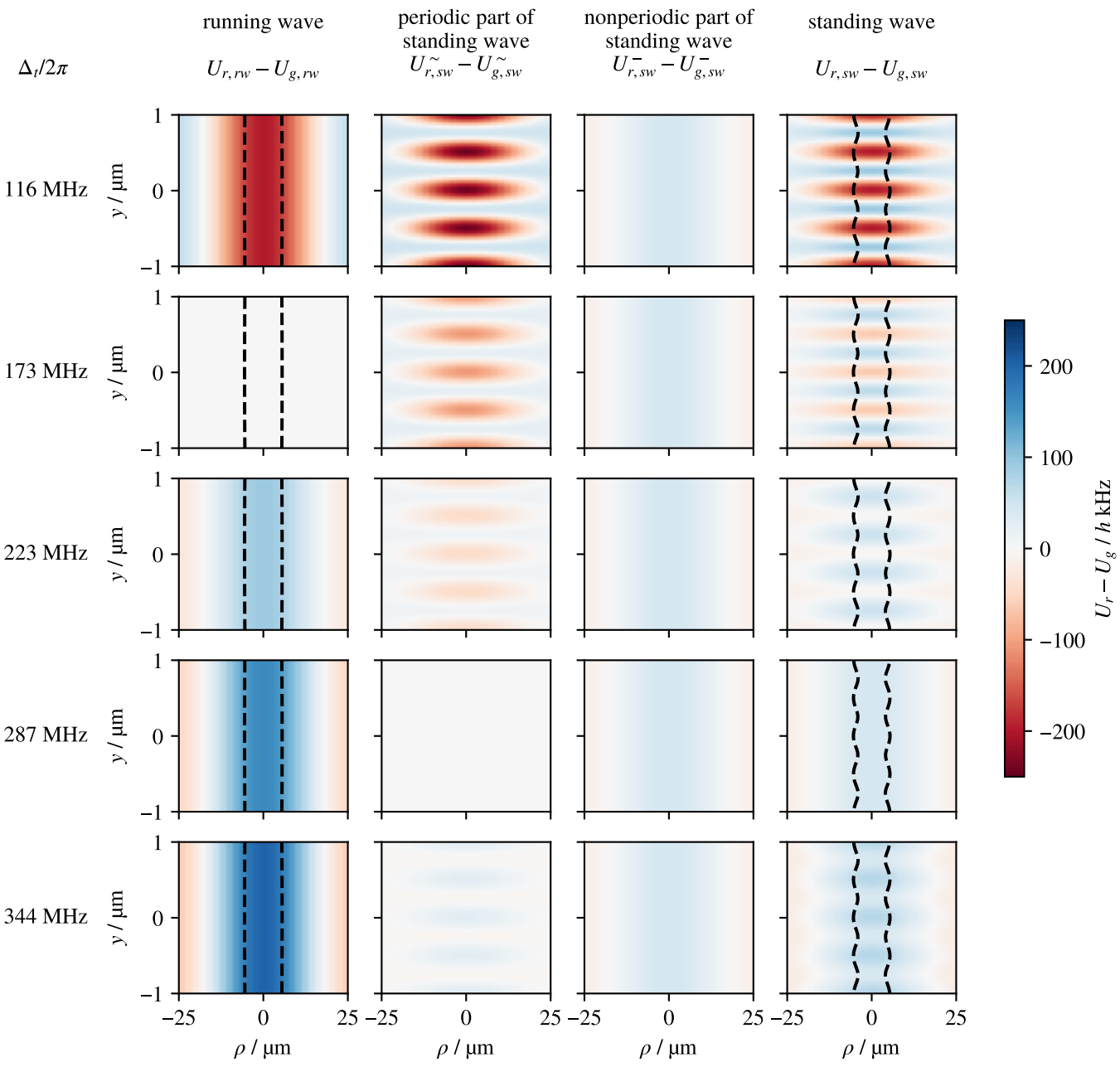

Figure 2.3: Differences of the trap potential for the ground and Rydberg state ($n = 94$) for the running wave (left) and standing wave (right) case, as well as the periodic and nonperiodic parts into which the standing wave potential may be decomposed (center left and center right). The mean value of the differential light shift has been subtracted for each case individually. The magic point, i.e. the trap detuning Δ_t where the variance of the differential light shift experienced by the excited atoms is smallest, depends on the trap geometry: For the parameters used for this figure, the magic point for the running wave is at $\Delta_t = 2\pi \cdot 173\,\mathrm{MHz}$, the one for the standing wave is at $\Delta_t = 2\pi \cdot 223\,\mathrm{MHz}$. The standing wave magic point differs from the magic point for just the periodic part, which would be at $\Delta_t = 2\pi \cdot 287\,\mathrm{MHz}$. The magic detuning also depends on the distribution of atoms in the trap. The region where 80 % of the atoms are located is indicated with dashed lines.

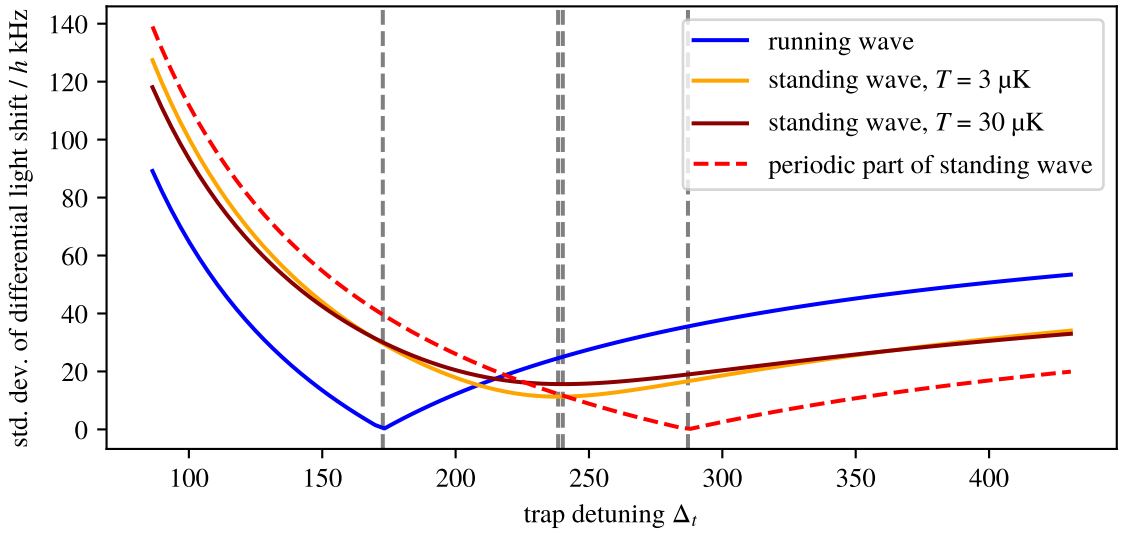

Figure 2.4: Standard deviation of differential light shifts across a cloud in the different traps ($n = 94$, $T = 9\,\mu$K). Since it is possible to completely equalize the trapping potentials for the ground and Rydberg state for the running wave trap and for the periodic part of the standing wave trap, the minimal standard deviation across the cloud is 0 in these cases. Since it is not possible to completely equalize the trapping potentials for the standing wave trap, for a cloud of finite size the minimal standard deviation is always greater than zero.

The variance of the differential light shifts is computed for clouds at different temperatures. The results are also shown in figure 2.4. While the smallest achievable differential light shift variance is lower for the low-temperature cloud, as expected since it covers a smaller volume, the optimal detuning at which the variance is minimized does not differ significantly.

2.1.7 Summary

The trap potential calculation has shown that the shape of the trap potential for Rydberg states differs from the shape of the intensity distribution. For a standing wave trap, this makes it impossible to perfectly match the trap potentials for the ground and Rydberg state. However, an optimal trap detuning that minimizes the variance of differential light shifts across the cloud does exist. For the case of a running wave trap, due to the absence of variations of the intensity on the scale of the Rydberg electron wavefunction, a magic detuning does exist. The optimal trap detuning in the standing wave significantly differs from the optimal (magic) trap detuning in the running wave.

2.2 Spectroscopy for finding the magic wavelength

To find the optimal trap detuning, we initially considered a spectroscopic measurement. If it were possible to equate the trapping potentials for the ground state $|g\rangle$ and Rydberg state $|r_n\rangle$ completely, then this magic point could be found using spectroscopy of the $|g\rangle$ to $|r_n\rangle$ transition, which would have its free-space resonance frequency only at the magic trapping wavelength. For the running wave trap, where it is possible to completely equate the potentials for $|g\rangle$ and $|r_n\rangle$, this approach is expected to work.

However, for the real standing wave trap, which differs from an idealized plane standing wave, it is impossible to reach completely identical trapping potentials for $|g\rangle$ and $|r_n\rangle$. The optimal trap detuning, where the variance of the differential light shift across the cloud is smallest, does not coincide with the trap laser wavelength where the mean differential light shift across the cloud is smallest, so the simple approach of matching the free-space resonance frequency is not expected to work. In principle, the width of the $|g\rangle$ to $|r_n\rangle$ resonance is influenced by the variance of the differential light shift across the cloud, so in this section we investigate whether it is possible to extract the optimal trap detuning from the width of the resonance.

To be able to determine the trap detuning Δ_t from the $|a\rangle$ to $|r_n\rangle$ resonance, this resonance must be found, which is done using three-photon spectroscopy, since there is no 420 nm laser in the experiment capable of driving the $|g\rangle$ to $|a\rangle$ transition directly. The calibration measurements for the trap detuning are shown and explained in this section.

2.2.1 Probe susceptibility of the cloud in steady state

Explaining the width of the $|g\rangle$ to $|r_n\rangle$ resonance and the probe transmission on $|a\rangle$ to $|r_n\rangle$ resonance requires modeling the four-level system consisting of $|g\rangle$, $|e\rangle$, $|a\rangle$, and $|r_n\rangle$, with the probe, control, and trap lasers coupling these states (see figure 1.5), and calculating the probe transmission in steady-state. The polarization of the lasers and the preparation of the atoms in $|g\rangle$ ensure that these four states are the only populated ones.

We consider the four-level system consisting of the four relevant levels and the three lasers as specified in figure 1.5. The trap and control lasers are σ^--polarized, and the probe laser is σ^+-polarized. The calculation is done as in e.g. ref. [26].

Setup of the Hamiltonian The Hamiltonian consists of two parts, describing the atom itself and the atom-light interaction. When setting the energy of the ground state $|g\rangle$ to 0, the atomic part is

$$\hat{H}_A = \begin{pmatrix} 0 & 0 & 0 & 0 \\ 0 & E_e & 0 & 0 \\ 0 & 0 & E_a & 0 \\ 0 & 0 & 0 & E_r \end{pmatrix}.$$

For the interaction, we make the dipole approximation. This will not capture the details of the light shift of the Rydberg state depending on the trapping beam geometry as described in section 2.1 directly, but they can be taken into account later since off-resonant terms are anyway treated only through their shifting of the atomic energy levels.

The resulting Hamiltonian in a rotating frame given by the unitary transformation

$$\hat{U} = \begin{pmatrix} 1 & 0 & 0 & 0 \\ 0 & e^{i\omega_p t} & 0 & 0 \\ 0 & 0 & e^{i(\omega_p+\omega_c-\omega_t)t} & 0 \\ 0 & 0 & 0 & e^{i(\omega_p+\omega_c)t} \end{pmatrix}$$

using the rotating wave approximation is

$$\hat{\tilde{H}} = -\hbar \begin{pmatrix} 0 & \Omega_{ge}/2 & 0 & 0 \\ \Omega_{ge}/2 & \Delta_p & 0 & \Omega_{er}/2 \\ 0 & 0 & \Delta_p + \Delta_c - \Delta_t & \Omega_{ar}/2 \\ 0 & \Omega_{er}/2 & \Omega_{ar}/2 & \Delta_c + \Delta_p \end{pmatrix}.$$

The effect of far off resonant light has been neglected in making the rotating wave approximation, but it can be taken into account by computing the shifts of the four relevant levels, U_i, and adding them into the Hamiltonian, which then becomes

$$\hat{\tilde{H}} = -\hbar \begin{pmatrix} U_g/\hbar & \Omega_{ge}/2 & 0 & 0 \\ \Omega_{ge}/2 & (U_e/\hbar + \Delta_p) & 0 & \Omega_{er}/2 \\ 0 & 0 & U_a/\hbar + \Delta_p + \Delta_c - \Delta_t & \Omega_{ar}/2 \\ 0 & \Omega_{er}/2 & \Omega_{ar}/2 & U_r/\hbar + \Delta_c + \Delta_p \end{pmatrix}.$$

This way one can even take into account the details of the Rydberg trapping potential described in section 2.1, when performing the calculation done here for multiple locations.

Decoherence and decay To take decay into account, the Lindblad master equation formalism is used (see e.g. ref. [8]). It only considers decay to any of the four levels in the calculation, but no decay into other states. Decay from level $|i\rangle$ to $|j\rangle$ is modeled by expanding the von Neumann equation with a term $\Gamma_{ij} D[\hat{\sigma}_{ij}]\hat{\rho}$, where $\hat{\sigma}_{ij} = |i\rangle\langle j|$ and the Lindblad superoperator is $D[\hat{O}]\hat{\rho} = \hat{O}\hat{\rho}\hat{O}^\dagger - \frac{1}{2}(\hat{O}^\dagger\hat{O}\hat{\rho} + \hat{\rho}\hat{O}^\dagger\hat{O})$. This leads to decay terms for the populations and also for the coherences. Decay of coherences due to other reasons than population decay is not treated in this initial calculation, but will be considered later in chapter 4.

All dipole-allowed transitions between the 4 levels are considered as decay paths, i.e. $|r_n\rangle$ to $|a\rangle$, $|r_n\rangle$ to $|e\rangle$, $|a\rangle$ to $|g\rangle$, and $|e\rangle$ to $|g\rangle$. The final von Neumann equation thus has the form

$$\frac{d\hat{\rho}}{dt} = -\frac{i}{\hbar}[\hat{H}, \hat{\rho}] + \Gamma_{ra} D[\hat{\sigma}_{ra}]\hat{\rho} + \Gamma_{re} D[\hat{\sigma}_{re}]\hat{\rho} + \Gamma_{ag} D[\hat{\sigma}_{ag}]\hat{\rho} + \Gamma_{eg} D[\hat{\sigma}_{eg}]\hat{\rho}.$$

The values for the decay constants are taken to be the transition rates between the states, calculated from the dipole matrix elements, i.e.

$$\Gamma_{ij} = \frac{\omega_{0,ij}^3 \mu_{ij}^2}{3\pi\epsilon_0 \hbar c^3}$$

with the transition frequency $\omega_{0,ij}$ and the dipole matrix element μ_{ij} of the transition [26].

Solving the steady state equations To calculate the steady state, we set $\frac{d\hat{\rho}}{dt} = 0$. This results in a set of 16 linear equations, one for each density matrix element. In addition, the constraints of the normalization of the populations, $\sum_{i=1}^{4} \rho_{ii} = 1$, and of the Hermiticity of the density matrix, $\rho_{ij} = \rho_{ji}^*$, are added to this set of equations. The linear system is constructed symbolically and solved numerically, giving the density matrix elements in the rotating frame.

Probe transmission The probe transmission is calculated from the imaginary part of the electric susceptibility

$$\chi = n\frac{d_{ge}}{\epsilon_0 \mathcal{E}_p}\rho_{ge},$$

which is given by the polarization or density of electric dipoles per probe field strength [26, p. 289]. Here, n is the number density of atoms, d_{ge} is the dipole matrix element for the ground and excited state, and $\mathcal{E}_p$ is the electric field amplitude of the probe light. A plane wave of a single frequency with wave number k propagating through a medium of susceptibility χ experiences a phase shift and gain/loss of $e^{-i\chi kz/2}$ after a distance z. Considering only the absorption/gain, the transmission is given by $T = e^{-\operatorname{Im}\chi\frac{2\pi z}{\lambda}}$.

Since we are using neither a plane wave nor a homogeneous cloud, the transmission we measure is an average over different densities and field strengths, which we approximate by using the electric field corresponding to the peak intensity of the Gaussian probe beam, and by replacing the cloud length and density by a column density that can be calibrated from measurements of the optical density of the cloud when the probe is on resonance, without any control light.

In terms of the column density n_A, the transmission is

$$T = \exp\left(-\frac{2\pi n_A d_{ge} \operatorname{Im}\rho_{ge}}{\epsilon_0 \mathcal{E}_p \lambda}\right) \tag{2.24}$$

By normalizing the lineshape to a function $f(\Delta_p)$, one can also perform a fit in terms of the optical density on resonance,

$$T(\Delta_p) = \exp\Big(-f(\Delta_p)\cdot \mathrm{OD}\Big) \tag{2.25}$$

The column density is useful for computing the expected transmission when the probe is not on resonance and other lasers are involved, while the optical density is a value that is only valid for this particular configuration of the probe being on resonance and the only laser involved.

2.2.2 Finding the $6P_{3/2}$ to $nS_{1/2}$ resonance by three-photon spectroscopy

To find the $|a\rangle$ to $|r_n\rangle$ resonance of the trap laser, the probe and control lasers are close to two-photon resonance, with the single-photon detunings Δ_p and Δ_c either close to 0, which leads to electromagnetically induced transparency (EIT) [27], i.e. an increase in transmission close to two-photon resonance, or far-detuned (by a few 100 MHz), leading to a dip in transmission. Measurements without the trap laser, showing just these features in the transmission spectrum, are shown in the top row of figure 2.6, exemplary for $n = 54$. The trap laser is scanned in the vicinity of the $|a\rangle$ to $|r_n\rangle$ resonance. When it is on resonance, this leads to a splitting of both the EIT peak and of the transmission dip, as predicted by the calculation of the steady state transmission carried out as described in section 2.2.1, whose results are shown in figure 2.5. This splitting is sensitive to relatively small detunings of the trap laser. When the trap laser is off resonance by a few MHz, this leads to an asymmetric splitting of the transmission feature, and for even larger trap detunings to no splitting, but just a shifting of the feature. This behavior is predicted by the calculation, and a similar sensitivity was also observed experimentally. In figure 2.6,

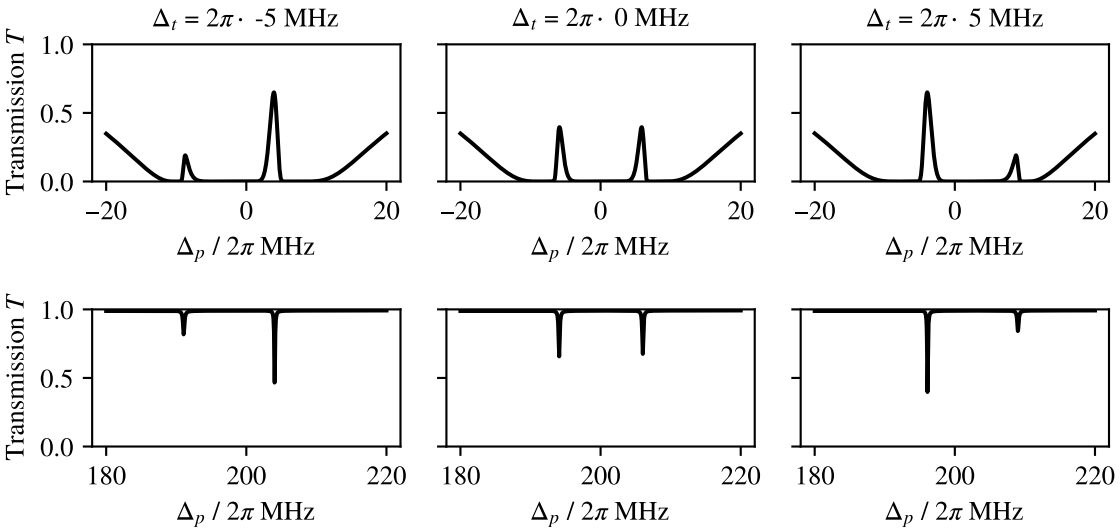

Figure 2.5: Calculated probe transmission close to two-photon resonance for two cases at $n = 54$: With probe and control on single-photon resonance, there are probe transmission peaks in the absorption valley (EIT, top row). With both lasers off single-photon resonance with a single-photon detuning of $\Delta/2\pi = 200\,\mathrm{MHz}$, there are probe transmission dips around Δ. The expected probe transmission is shown for different detunings Δ_t of the trap laser, at very low power of the trap laser. Both the EIT peak and the transmission dip on two-photon resonance are split when the trap laser is on resonance with the $|a\rangle$ to $|r_{54}\rangle$ transition, and this splitting becomes asymmetric when the trap laser is off-resonant.

measurements with small and large single-photon detunings are shown, which display the predicted splitting of the transmission features. Small trap powers are used in the measurements shown here, since the splitting otherwise becomes too large to be easily observable. To determine the trap detuning up to an accuracy of a MHz, the trap power is iteratively increased and the trap laser frequency adjusted to still evenly split the peak.

The splittings observed at the powers used differ from the theoretically predicted splittings computed for the intensity given by the beam geometry of the trap (section 1.3) by about a factor of 2: The observed splitting of the EIT peak at a trap power of 7 mW is about 6 MHz, the observed splitting of the transmission dip at a trap power of 5 mW is about 4 MHz. The calculation with a trap power of 6 mW predicts a splitting of 12 MHz. The reasons for the discrepancy is that the calculation is done only for atoms sitting in the region of peak intensity, but in reality most atoms are both transversally and, since the measurement was done in the long cloud, also longitudinally outside the focus, and do not experience the peak intensity. The number of atoms sitting outside the regions of peak intensity is much larger in this measurement than is usual in the standing wave trap because of the very low power used. This provides a plausible explanation for the discrepancy.

The splitting being smaller than expected has no influence on the accuracy of the calibration of the trap detuning, so no detailed numerical calculation of the expected average intensity is performed here.

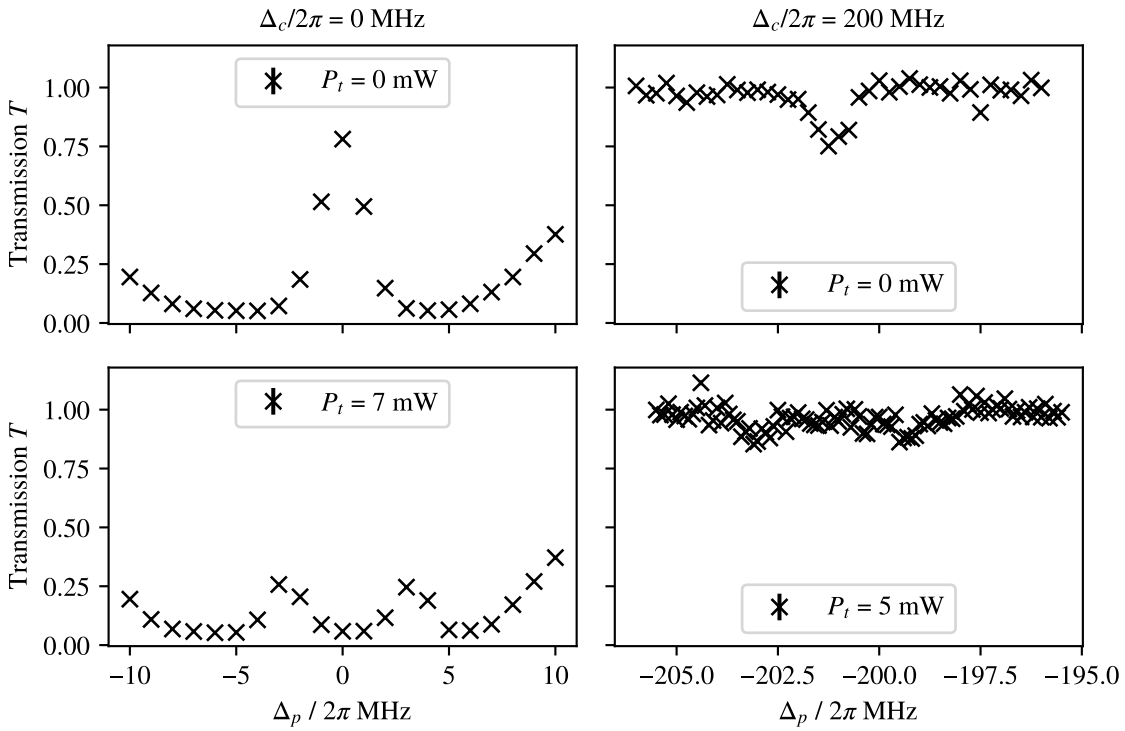

Figure 2.6: Probe transmission on and off single-photon resonance, in both cases close to two-photon resonance, with the trap laser resonant with the $|a\rangle$ to $|r_n\rangle$ transition ($n = 54$), leading to a splitting of the EIT peak and of the two-photon resonance dip as qualitatively predicted (compare to figure 2.5)

2.2.3 Linewidth of the two-photon resonance

To be able to determine whether changes in the linewidth of the absorption line on two-photon resonance are due to a change in the variance of the differential light shifts across the atom cloud, it is necessary to identify the significant contributions to the observed linewidth other than differential light shifts. For this purpose, the absorption line is measured in free space for different powers of the control laser, and an attempt is made to explain the observed linewidths.

In order to be able to calculate the expected transmission of probe light on two-photon resonance, the average column density of atoms in the probe beam needs to be known. It may be measured by scanning the probe detuning Δ_t in a region around the $|g\rangle$ to $|e\rangle$ resonance, and fitting the transmission computed in section 2.2.1. Such a measurement and fit are shown in figure 2.7, giving an average column density of atoms in the probe beam of $n_A = 286\,\mu\text{m}^{-2}$.

Contributions to the linewidth In increasing order of the size of the contribution to the linewidth of the absorption line, the contributing mechanisms are the natural decay of the Rydberg state, blackbody radiation induced decay of the Rydberg state, power-broadening, faster decay of the Rydberg state due to admixture of the intermediate state $|e\rangle$, spatially varying differential light shifts of the ground and Rydberg state due to the control laser, and Doppler broadening due to movement of the atoms, and

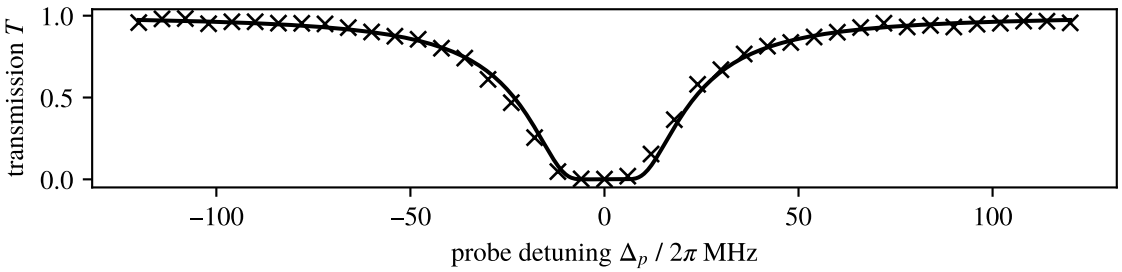

Figure 2.7: Transmission of the probe beam through the cloud at different probe detunings Δ_p. From this measurement, the average column density of atoms for this cloud and the positioning of the probe beam is determined to be $n_A = 286\,\mu\text{m}^{-2}$, by fitting eq. 2.24.

broadening due to Rydberg-Rydberg interactions. The numbers and data given in this section are all for a principal quantum number of $n = 54$

The natural linewidth (Lorentzian FWHM) of the Rydberg state $|r_{54}\rangle$ is 0.97 kHz, including blackbody radiation induced decay at room temperature increases this to 2.07 kHz. For our beam geometry (section 1.3) and a control power of 130 mW, the two-photon Rabi frequency is $\Omega = 2\pi \cdot 2.9\,\text{kHz}$, the power broadened linewidth, if this were much larger than the natural linewidth, which it is not, would be $\sqrt{2}\Omega = 4.1\,\text{kHz}$ [26].

The additional linewidth due to differential light shifts by the control beam is computed as follows: Similarly to the trap laser, the control laser creates a potential for the ground and Rydberg states. Since the polarization is identical (σ^-) and the $|a\rangle = |6P_{3/2}, F = 3, m_F = 3\rangle$ and $|e\rangle = |5P_{3/2}, F = 3, m_F = 3\rangle$ states differ only in the principal quantum number, the trapping potential for the Rydberg state is the same except for the reduced matrix element to be used, i.e. similar to eq. 2.13,

$$U_r(\vec{r}) = -\frac{1}{16}\frac{D_{e,r_n}^2}{\hbar\Delta_t}E^2(\vec{r}) - \frac{\alpha_f}{4}\langle r_n|E^2(\vec{r}+\vec{r}_e)|r_n\rangle \tag{2.26}$$

with the J-reduced dipole matrix element D_{e,r_n} between $|e\rangle$ and $|r_n\rangle$ instead of the one between $|a\rangle$ and $|r_n\rangle$. The ground state potential due to the control laser is, just like for the trap laser (eq. 2.12),

$$U_g(\vec{r}) = -\frac{1}{4}\alpha_g E^2(\vec{r}) \tag{2.27}$$

but using the ground state polarizability for 480 nm light, which is negative, i.e. the potential is repulsive, since the control laser is blue-detuned from the D1 and D2 lines.

The differential light shift is computed on a 3D grid, and the grid points are weighed. The weight consists of the probability of finding an atom at the location based on the temperature of the cloud and the trapping potential given by the crossed beam dipole trap, and the probability of actually exciting it, which is given by the square of the two-photon Rabi frequency (as described in section 4.2).

Then, the probability of an atom experiencing a certain differential light shift is computed. This gives the lineshape due to the differential light shifts. It is shown in figure 2.8 The line is highly asymmetric because most excited atoms are in the region of highest control intensity, which is also the region where the atoms experience the largest differential light shift. Since there is no region of higher control intensity,

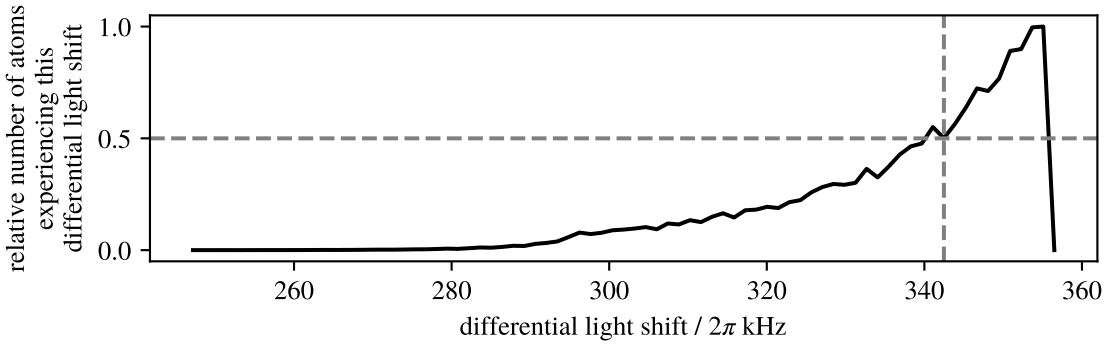

Figure 2.8: Rydberg line broadening due to differential light shifts of the control laser at a control power of 130 mW. The dashed lines mark the FWHM of the line, which is 12.6 kHz. The non-smoothness is due to the limited number of grid sites used in the numerical calculation.

there is a sharp dropoff towards larger differential light shifts. In contrast, since the control intensity is gradually reduced away from the center of the beam, and because there are atoms in those outer beam regions, the dropoff towards lower differential light shifts is very smooth.

Finally, even though the atoms are very cold at $T = 8\,\mu\text{K}$, their movement still leads to Doppler broadening of the spectral line. This gives a Gaussian lineshape with standard deviation $\sigma = \sqrt{\frac{k_B T}{m_{\text{Rb-87}} c^2}} ck$. The Doppler broadening is reduced due to the counterpropagating excitation beams. At 8 µK, this gives a FWHM of 348 kHz, which is by far the largest contribution to the linewidth.

In figure 2.9, measurements of the Rydberg absorption line close to two-photon resonance are shown, along with theoretically expected lines.

The expected lines are computed by convolving $\text{Im}\,\rho_{ge}$ with the lightshift lineshape and with the Doppler broadened lineshape, both normalized to a total probability of 1. This neglects a part of the natural linewidth that is due to decay to states other than the ones included in the four-level calculation, and it also neglects blackbody decay, but since these contributions are very small compared to the other contributions to the lineshape, this does not have a significant impact on the linewidth. The transmission is computed using the previously calibrated atom column density. It is obvious that the calculated lineshapes describe neither the linewidth nor the lineshape of the measured absorption lines. Only the shift of the line, which increases with larger control power, is accurately captured by the calculation. This suggests that the calculation of the differential light shifts is accurate, but that there is another effect dominating the lineshape and -width.

This effect is the interaction between Rydberg atoms: In the measurements shown here, approximately 60 probe photons per pulse were used. At the very small coupling between the ground and Rydberg state, the strong Rydberg-Rydberg interaction prevents the excitation of many atoms to Rydberg states: The number density of Rydberg atoms for a given excitation bandwidth Ω_R between the ground and Rydberg state is $\sqrt{\hbar\Omega_R/C_6}$ [28, p. 12]. For an excitation bandwidth of $\Omega_R = 2\pi \cdot 100\,\text{kHz}$, this gives a mean distance between Rydberg atoms of 7 µm. At the length of the cloud of about 100 µm and a probe waist of 5 µm, it seems plausible that only a small fraction of the probe photons sent into the cloud can actually excite a Rydberg atom, leading to a transmission that is much larger than naively expected. In addition, the strong Rydberg interactions shift the Rydberg level of nearby atoms, causing a broadening

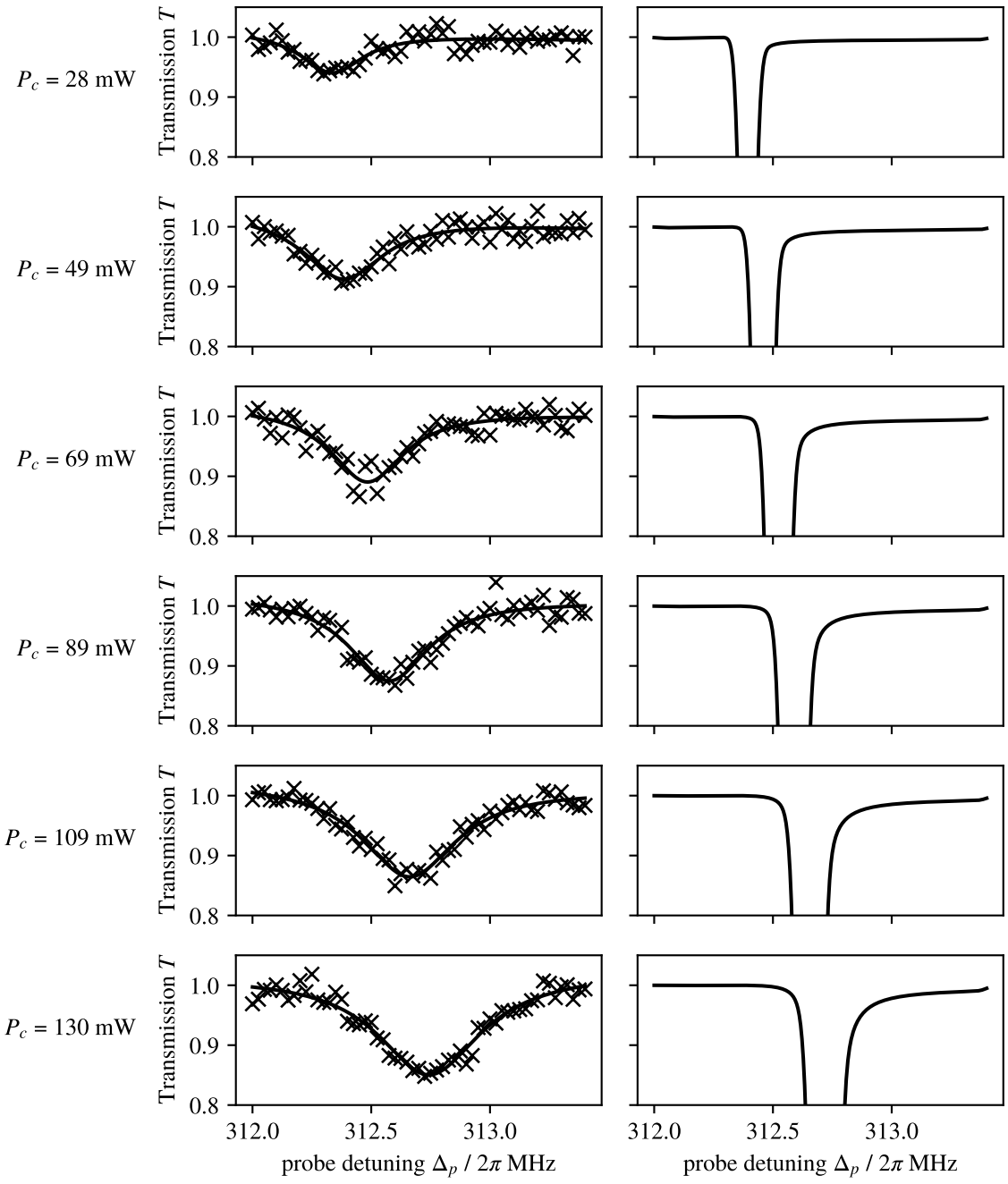

Figure 2.9: Measurement of probe transmission for single photon detuning $\Delta_c \approx -300\,\mathrm{MHz}$ close to two-photon resonance with Lorentzian fits (left) and theoretically expected transmission without considering Rydberg interactions. At increased control powers, the line shifts and broadens, because the ground and Rydberg levels experience a spatially inhomogeneous differential light shift. Much fewer photons are absorbed than a simple calculation suggests due to Rydberg blockade. Rydberg interactions also cause the line to be broader than expected.

of the line. Since larger control powers increase the number density of Rydberg excitations, this also increases the absorption of probe photons, which causes the decrease in transmission seen for higher control powers in figure 2.9.

In conclusion, at the rather large probe photon numbers used, the linewidth of the Rydberg absorption line is dominated by Doppler broadening and Rydberg-Rydberg interactions. This will likely make it difficult to measure the comparatively small effect of the variance of differential light shifts in the linewidth.

2.2.4 Sensitivity of spectroscopic measurements to differences in trapping potential

To determine whether it is possible to find the optimal trap detuning by spectroscopy, probe transmission spectra as a function of the probe detuning Δ_p are taken, and the measured absorption lines are fitted with Lorentzian functions to determine the line centers and widths (FWHM). This is done in the standing wave and in the running wave trap. For the measurements done in the running wave, the crossed beam optical dipole trap is turned on between experiments to prevent the atom cloud from expanding too much in the y-direction, along the trapping beam. For the standing wave, this is not necessary, since it provides sufficient confinement in this direction.

The measured spectra are shown in figure 2.10, for different trap detunings Δ_t. The centers of the lines clearly shift when changing the trap detuning, because the mean differential light shift between $|g\rangle$ and $|r_n\rangle$ experienced by the atoms changes for different trap detunings Δ_t, as described in section 2.1. There is no obviously visible change in the linewidth.

To quantitatively compare the lines at different trap detunings, the line centers and widths extracted from the Lorentzian fits are shown in figure 2.11. The line centers show a clear dependence on the trap detuning, they are shifted towards larger probe detunings for larger trap detunings. The trap detuning at which the line center coincides with the center of the line in free space is not significantly different for the two trap geometries. The mean light shift is thus not suitable for finding an optimal trap detuning, since this should depend on the trap geometry. The line width is very similar to the free space case and mostly independent of the trap detuning for the running wave. For the standing wave, the linewidth is increased when the trap laser is tuned closer to the $|a\rangle$ to $|r_n\rangle$ resonance. While the latter behavior could be explained by increased admixture of the $|a\rangle$ state for smaller trap detunings, it should then also be observed in the standing wave trap, since the powers were chosen to achieve similar peak intensities. The previous measurements in free space showed that the linewidth is dominated by Doppler broadening and Rydberg interactions. This is the likely reason for the inability to resolve a change in linewidth due to a change in differential trap potential.

To reduce the influence of Rydberg interactions on the linewidth, it would be necessary to use far fewer photons. Since a scan over many probe detunings would then require many measurements to gather sufficient statistics, it is also worth considering other measurement schemes that are potentially more sensitive to changes in the variance of the differential light shift.

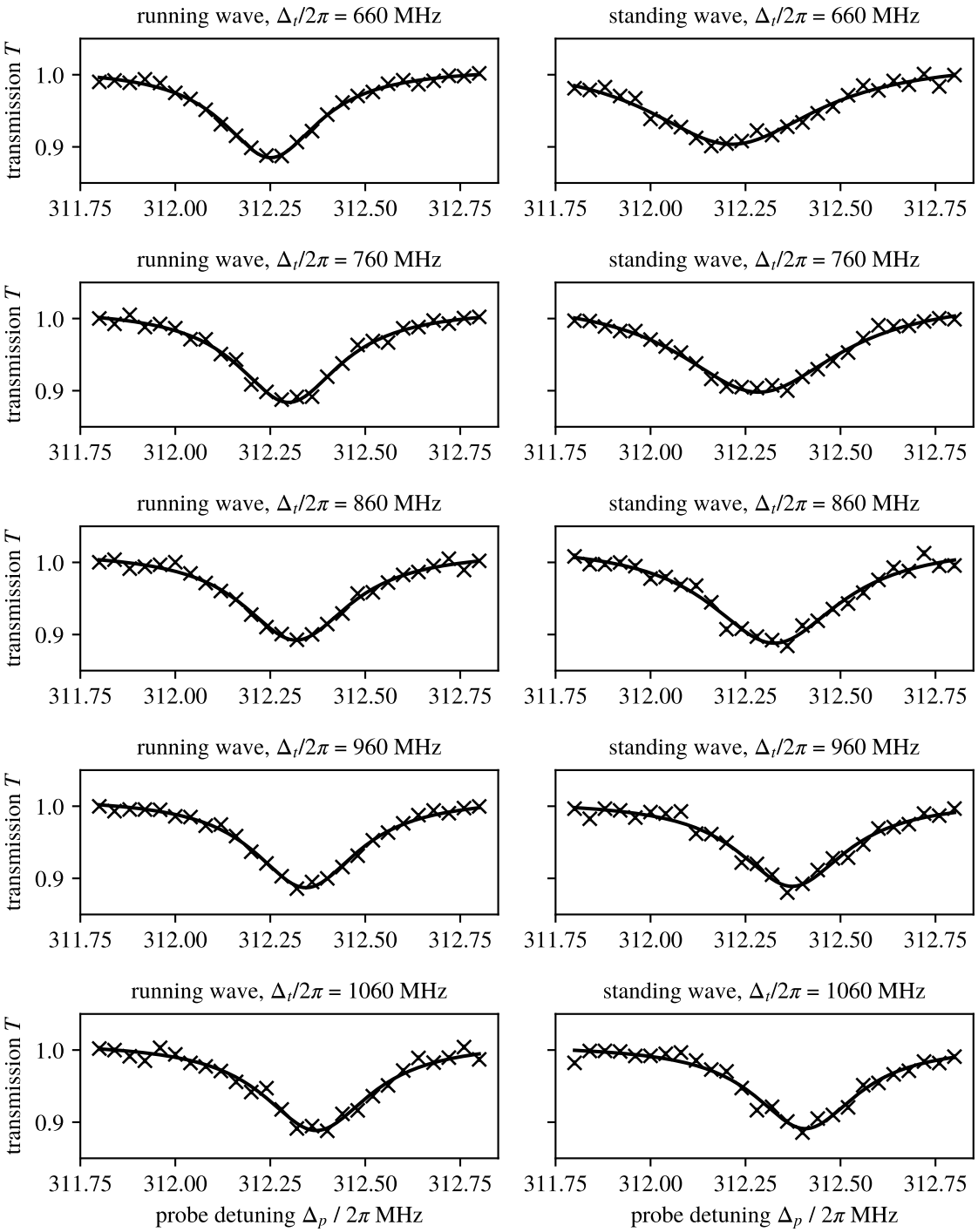

Figure 2.10: Transmission of probe light through the cloud close to two-photon resonance from $|g\rangle$ to $|r_n\rangle$, at $n = 54$ and a single-photon detuning of about $\delta \approx 2\pi \cdot 300\,\mathrm{MHz}$, in the running wave and standing wave trap at different trap detunings. Error bars are standard error of the mean and often smaller than the marker size, Lorentzian lineshapes are fitted to extract the center and width of the absorption lines. A summary of the line centers and widths is given in figure 2.11.

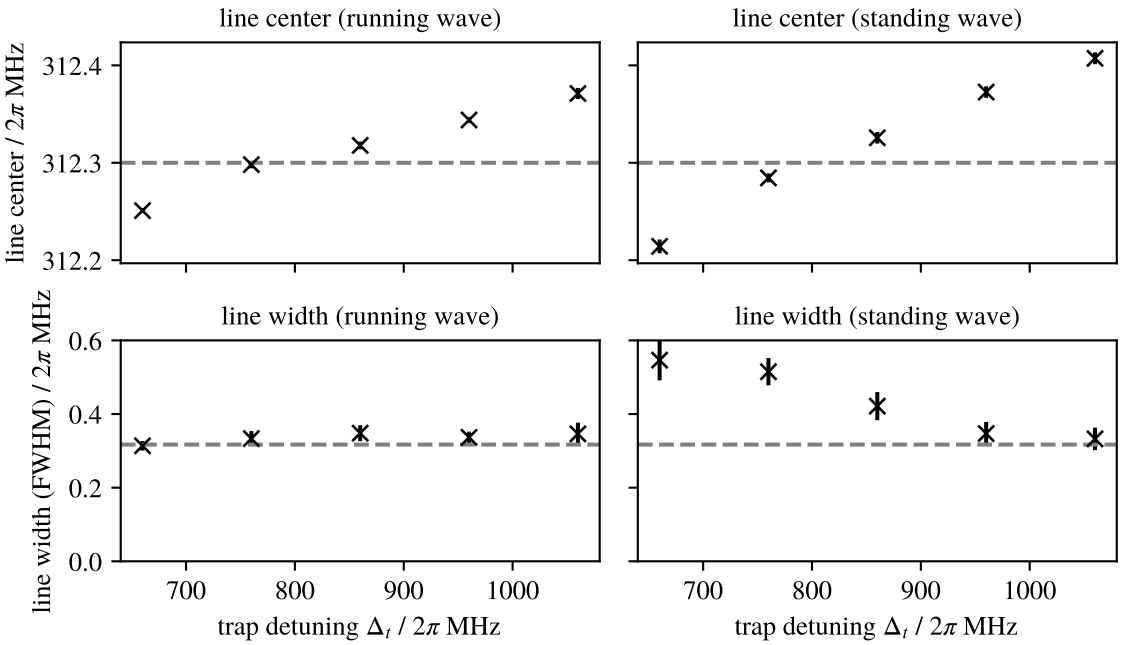

Figure 2.11: Absorption line centers and widths extracted from the data shown in figure 2.10. The magic detuning calculated for the running wave is $\Delta_t = 2\pi \cdot 995\,\mathrm{MHz}$, and $\Delta_t = 2\pi \cdot 1438\,\mathrm{MHz}$ for the periodic part of the standing wave potential. For the standing wave, we expect an optimal detuning of $\Delta_t = 2\pi \cdot 1267\,\mathrm{MHz}$. The linewidth and line center for the free-space measurement at the same control power of $P_c = 28\,\mathrm{mW}$ are drawn as dashed lines.

2.3 Photon storage for finding the magic wavelength

The second measurement scheme that was considered to measure differences of the variance in differential light shifts is the storage of photons as collective excitations in the atom cloud.

2.3.1 Slow light and photon storage

In section 2.2.1, we have used the imaginary part of the probe susceptibility to predict the transmission of the atom cloud for probe photons. However, the susceptibility also has a real part, which corresponds to the refractive index of the cloud. Under conditions where EIT is observed, the rate of change of the refractive index with the probe detuning can get quite large (figure 2.12 left panel). This shape of the dispersion leads to a small group velocity

$$v_g = \frac{c}{n(\Delta_p) + \omega_p \frac{\mathrm{d}n}{\mathrm{d}\Delta_p}},$$

and thereby to the effect of slow light [29, 30]. A measurement of the delay of a probe light pulse due to the atom cloud is shown in figure 2.12 (right panel). It is delayed by 0.27 µs. This is much less than the theoretically possible delay of 2.2 µs. The difference is due to performing the measurement with the probe and control lasers tuned 2.6 MHz off two-photon resonance, and because of a difference between

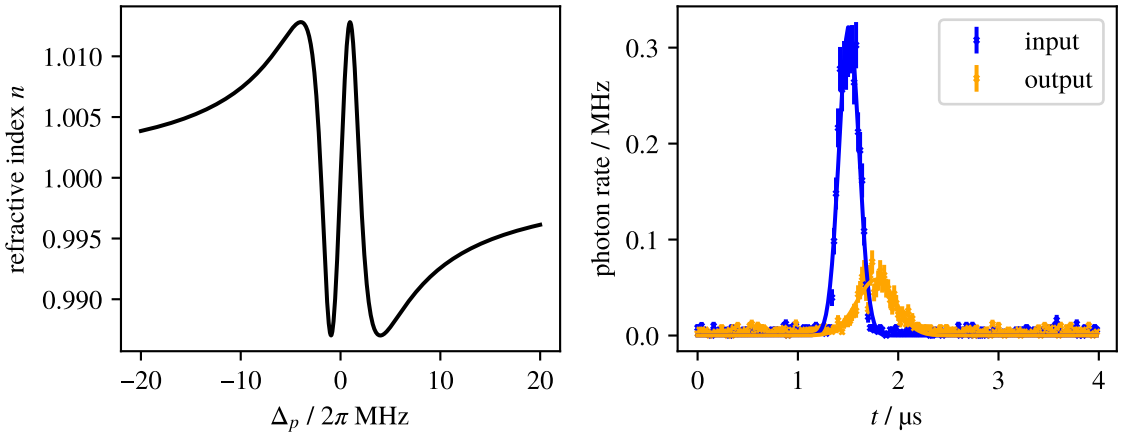

Figure 2.12: Left: Refractive index of the cloud with a length of 100 µm and a column density of atoms in the area hit by the probe beam of 287 μm^{-2}, corresponding to a density of 2.87×10^{12} cm^{-3}, at a control power of 44 mW. On two-photon resonance, this leads to a group velocity of 45 $m\,s^{-1}$ and a delay of 2.2 µs. Right: Measurement of the delay of a Gaussian probe pulse propagating through the atom cloud on EIT. The measured delay extracted from the Gaussian fits is 0.27 µs. For likely reasons for this large discrepancy, see the main text.

the peak control intensity and the one felt by the atoms, which are also located outside the control beam focus. The large two-photon detuning is also the reason for the small amount of transmitted light, since perfect EIT would only be achieved on two-photon resonance. For a control intensity that is lower by a factor of 2 and the used two-photon detuning, the measured delay is reproduced in the calculation.

Slow light can also be interpreted as light propagating through the atomic medium as a collective excitation. Such a collective excitation can be treated as a quasiparticle called polariton, which is a mixture of a photon and an atomic excitation. The more similar it is to a photon, the faster the propagation speed, and the more similar it is to an atomic excitation, the slower its propagation speed [12].

In our case, a Rydberg polariton is created by sending a probe photon into the cloud while the control light is on. This polariton propagates through the cloud. To store the photon in the cloud, the control laser is turned off, and the polariton is converted into a stationary collective excitation, which can be converted back into a propagating polariton by turning the control light back on. In this way, a photon can be stored in the cloud for some time. An example of the probe and control pulses used in photon storage experiments is shown in figure 2.13. The retrieved photon can be emitted into the same mode as the stored photon only because the phase of the exciting light mode is imprinted and stored in the atomic excitation. The retrieval efficiency into the exciting mode depends on whether this phase information is preserved during the waiting time between storage and retrieval. Any dephasing mechanism that leads to a decay of coherence between the ground and Rydberg state will affect the retrieval efficiency.

2.3.2 Measuring coherence time in a photon storage experiment

To measure the effect of decoherence due to spatially inhomogeneous differential light shifts, we would like to measure the efficiency with which photons can be stored in the atom cloud for different storage times. We define the retrieval efficiency to be the ratio of the retrieved photons compared to the number of photons stored in the cloud. For the number of stored photons we use the difference between the

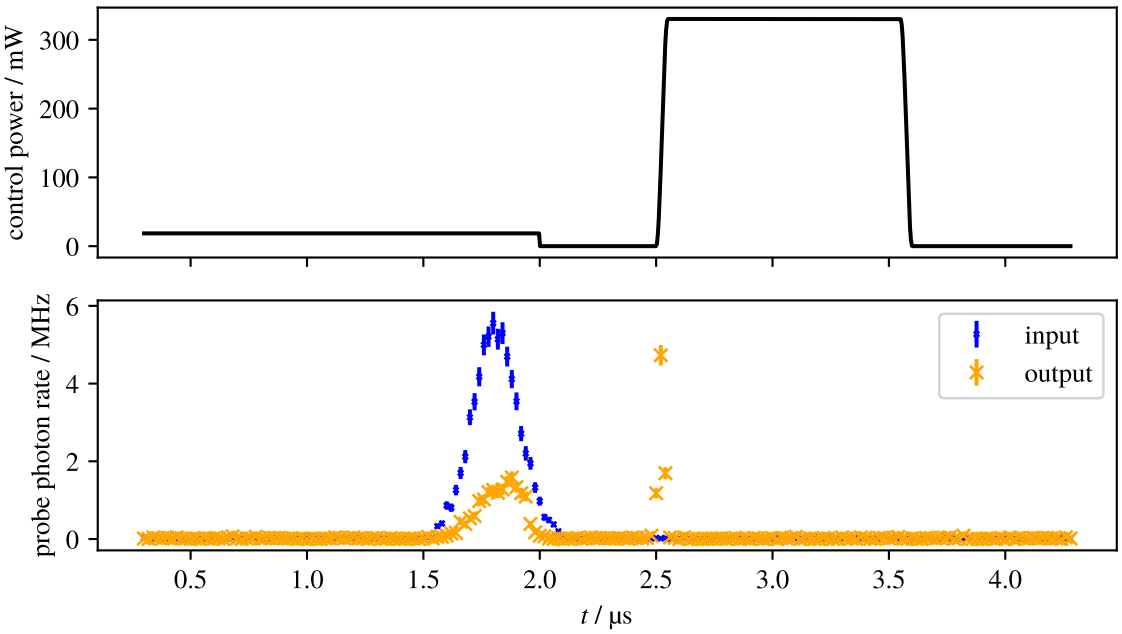

Figure 2.13: Pulse sequence for photon storage experiments. In the top panel, the control power used to store and retrieve probe photons is shown. Tukey pulses are used to avoid Fourier broadening. The control power during storage is kept low to not immediately retrieve the light again, and maximal for retrieval to retrieve the photons as quickly as possible. In the bottom panel, the input pulse sent into the cloud and the transmitted photons are shown. Many photons are already retrieved during storage because the pulse duration is longer than the pulse delay on EIT. At $t = 2.5\,\mu s$, when the control laser is turned back on, the retrieved photon pulse is observed. The storage time may be varied by choosing the timing of the second control pulse.

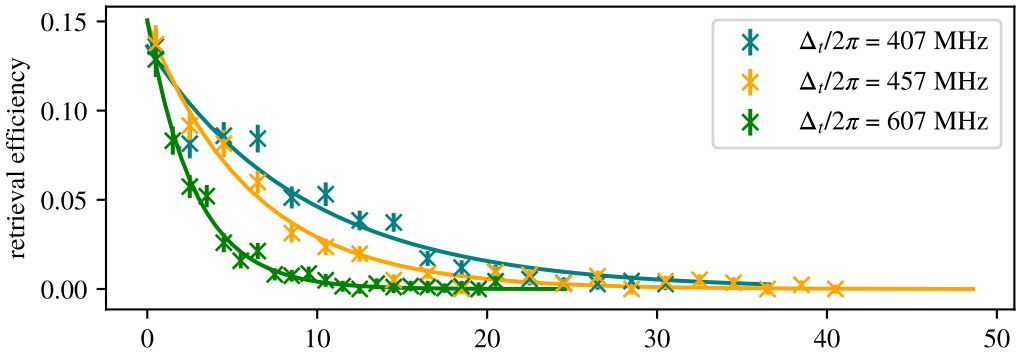

Figure 2.14: Photon storage efficiencies, calculated as described in the main text from the photon count traces, under different conditions, here different trap detunings. The measurements are done in the running wave.

number of photons in the input pulse and the number of immediately retrieved photons. Two example measurements of the retrieval efficiency for different storage times are shown in figure 2.14, at different conditions leading to different dephasing rates of the collective excitation. An exponential function $A\exp(-t/\tau)$ is fitted to the retrieval efficiencies to extract a single coherence time τ that can be used to compare photon storage measurements under different conditions. In the example case in figure 2.14, the coherence times extracted from the fit clearly show that the dephasing rate differs at different trap detunings.

An alternative approach to characterizing the dephasing rate of the stored collective excitation would be to compare the absolute efficiency at a fixed storage time, rather than measuring efficiencies at different times and comparing the decay rates. The fixed storage time approach has e.g. been used in ref. [19]. It has the advantage of requiring fewer measurements, but the disadvantage of also being sensitive to other factors influencing the overall storage efficiency, which also depends on e.g. the exact timing and power of the storage control pulse, and the overall number of atoms excited. In addition, the storage time used must be carefully chosen, since not all retrieval efficiency decays are perfectly exponential, due to effects such as motional rephasing and molecular excitations, which will be treated in detail in chapter 3. To avoid the influence of these factors, we have chosen to take measurements for different storage times and to fit an exponential function, which should be robust to additional oscillations of the storage efficiency.

2.3.3 Measuring the magic detuning by photon storage

To be able to measure the reduction of the inhomogeneity of differential light shifts that can be obtained by choosing the optimal trap detuning, it is necessary that dephasing due to differential light shifts is the dominant source of dephasing. If there are other, far quicker dephasing mechanisms, the overall decay rate of the storage efficiency will not change significantly when altering the trap detuning, making it impossible to find the trap detuning leading to the lowest spatial inhomogeneity of differential light shifts. Especially at higher Rydberg states, a large amount of dephasing is due to interactions between Rydberg atoms and ground state atoms (details in chapter 3). This made it necessary to drastically reduce the density of the cloud in which the photon storage experiments were performed, which also reduced the overall storage efficiency. However, when reducing the density enough, similar coherence times as for lower Rydberg states could be achieved, enabling the measurement of optimal trap detunings over a wide range of principal quantum numbers.

For 8 Rydberg states spanning a range of principal quantum numbers between $n = 45$ and $n = 94$, and for two different trap geometries (standing and running wave), measurements of the storage efficiency decay have been performed at different trap detunings. The data is summarized in figure 2.15. The optimal trap detuning for each Rydberg state and trap geometry are determined to be the trap detuning of maximal coherence time. The errors of the optimal trap detunings are determined manually by considering the spacing of the trap detunings for which measurements were taken, the error bars of the individual data points, and the rate of change of the coherence time close to the maximum. The estimated errors are shown as shaded areas in figure 2.15.

The errors of the optimal trap detunings for the standing wave are generally much larger than for the running wave. The reason for this is that the errors of the individual coherence times are larger, which indicates that the exponential functions do not fit the data as well as for the running wave. This is due to the advantage of the standing wave trap compared to the running wave: It confines the atoms in the y-direction. This does not mean that the atoms stop moving, but that their motion is confined to a smaller region, in which the atoms oscillate. For a very deep trap, the spatial amplitude of the oscillation may

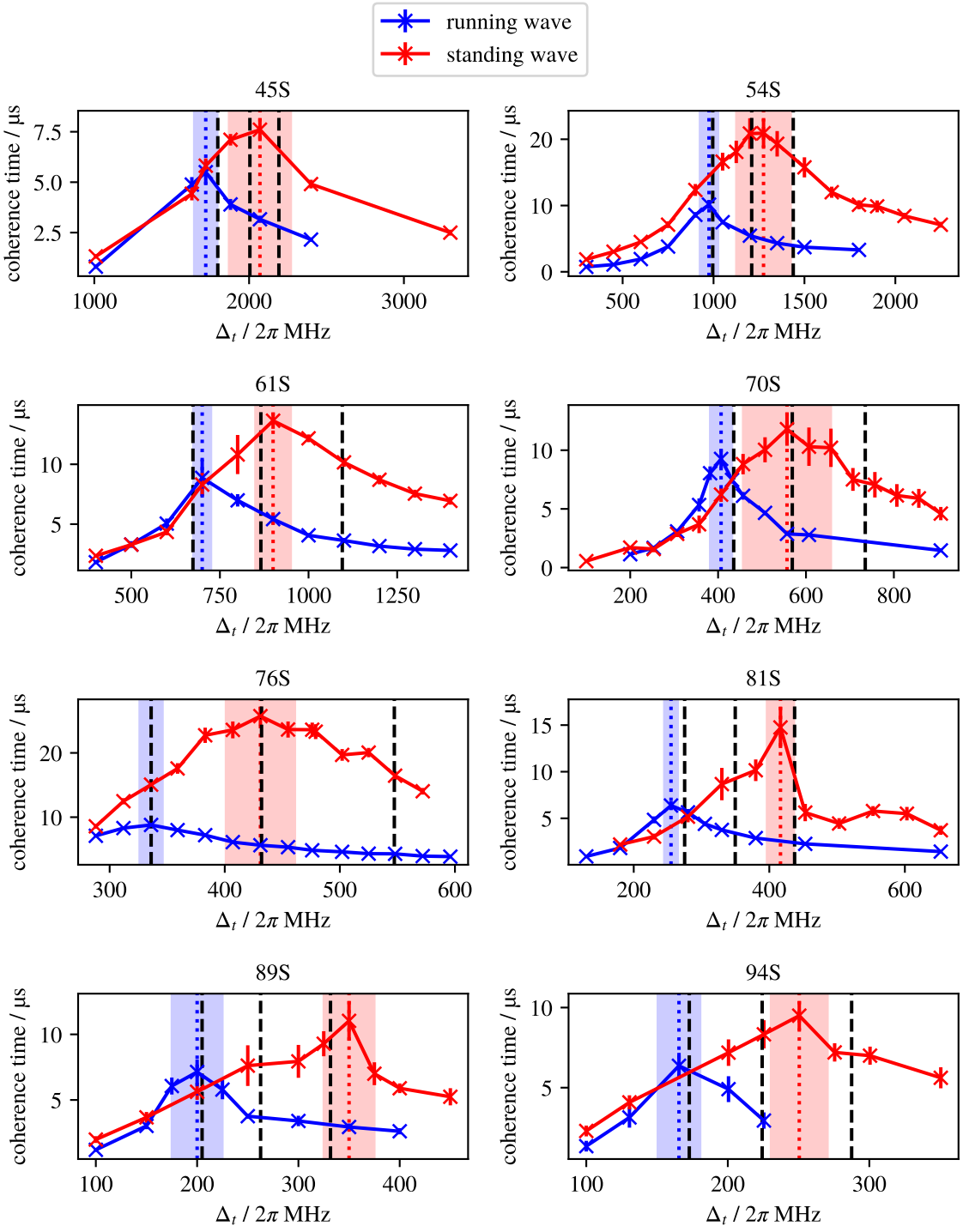

Figure 2.15: Measured coherence times obtained by fitting exponential functions to retrieval efficiencies for different Rydberg states and trap detunings, for the running wave and standing wave. The dashed black lines indicate the theoretically expected magic trap detunings for the running wave, the standing wave, and just the periodic part of the standing wave (they always occur in this order from small to large trap detunings). The best coherence times, which we deem the measured magic detunings, are marked with colored vertical lines, with the shaded areas indicating the estimated error. For discussion, see the main text.

be so small that it does not lead to significant dephasing, but in the case of a shallow standing wave trap, the spatial oscillation amplitude is large, so the motion of the atoms leads to significant dephasing of the collective excitation (a more detailed calculation of motional dephasing is given in chapter 4). As long as the trapping potential is close to harmonic, all atoms will however return to their original position after the same time, restoring the original collective excited state. There is a rephasing of the collective excitation and the storage efficiency increases again after one oscillation period of the atomic motion. Since increasing the trap depth to more tightly confine the atoms locally increases the density of atoms, which leads to faster dephasing, the standing wave power had to be kept low, leading to trap frequencies so small that at most two rephasing events occur within the time where any photons can be retrieved. This leads to a significant deviation of the storage efficiency decay from an exponential decay, and introduces an uncertainty of the coherence time extracted using an exponential fit.

While the confinement in the y-direction provided by the standing wave trap increases the uncertainty of the coherence time, it also increases the overall coherence time, an effect which is clearly visible for all Rydberg states.

2.3.4 Comparison of magic detunings in a running and standing wave trap

Since the optimal detunings extracted from the data shown in figure 2.15 clearly depend on the trap geometry, they can be compared to the theoretically predicted magic and optimal detunings for the running and standing wave from section 2.1. This is done in figure 2.16. In the top panel, the optimal trap detunings for the running wave, the standing wave, and the periodic part of the standing wave along with the measured optimal trap detunings are shown. The overall trend towards lower optimal trap detunings in any trap geometry is due to the scaling of the dipole matrix element between the $|a\rangle$ and $|r_n\rangle$ states. It decreases due to smaller overlap of the wavefunctions of the two states for higher n, so matching the ground state trap potential requires tuning the trap laser closer to resonance. Since the change of the dipole matrix element with the principal quantum number occurs over much larger scales than the difference between the optimal detunings for any Rydberg state, all detunings are divided by the running wave magic detuning to make the differences between the two trap geometries visible.

Dividing by the running wave magic detuning removes the scaling with the dipole matrix element, the result is shown in the bottom panel of figure 2.16. When looking at these normalized detunings, it is clear that while the agreement between measured optimal detunings for the running wave and the measured ones is overall good except for one slight outlier at $n = 81$, there are discrepancies between measurement and theoretical expectations for the standing wave, which are even larger than the error bars, which already take into account the uncertainty due to extracting a single coherence time from a non-exponential decay, and which are comparable in size to the difference between the prediction for the standing wave and just the periodic part of its trap potential.

The largest differences between theory and experiment occur for large principal quantum numbers. For these high Rydberg states, the dephasing due to interactions between Rydberg atoms and ground state atoms is much larger than for smaller n, which required lowering the density by a lot, reducing the retrieval efficiency. However, the loss of signal could mostly be compensated by performing more measurements, and this uncertainty would also be reflected in the error bars.

As calculated in section 2.1, the temperature of the atom cloud does not influence the optimal trap detuning, over the entire range of temperatures that can plausibly be achieved in the experiment. Fluctuations of the temperature of the prepared atom cloud during the measurement, which can take a few hours for the higher Rydberg states, therefore cannot explain the discrepancy.

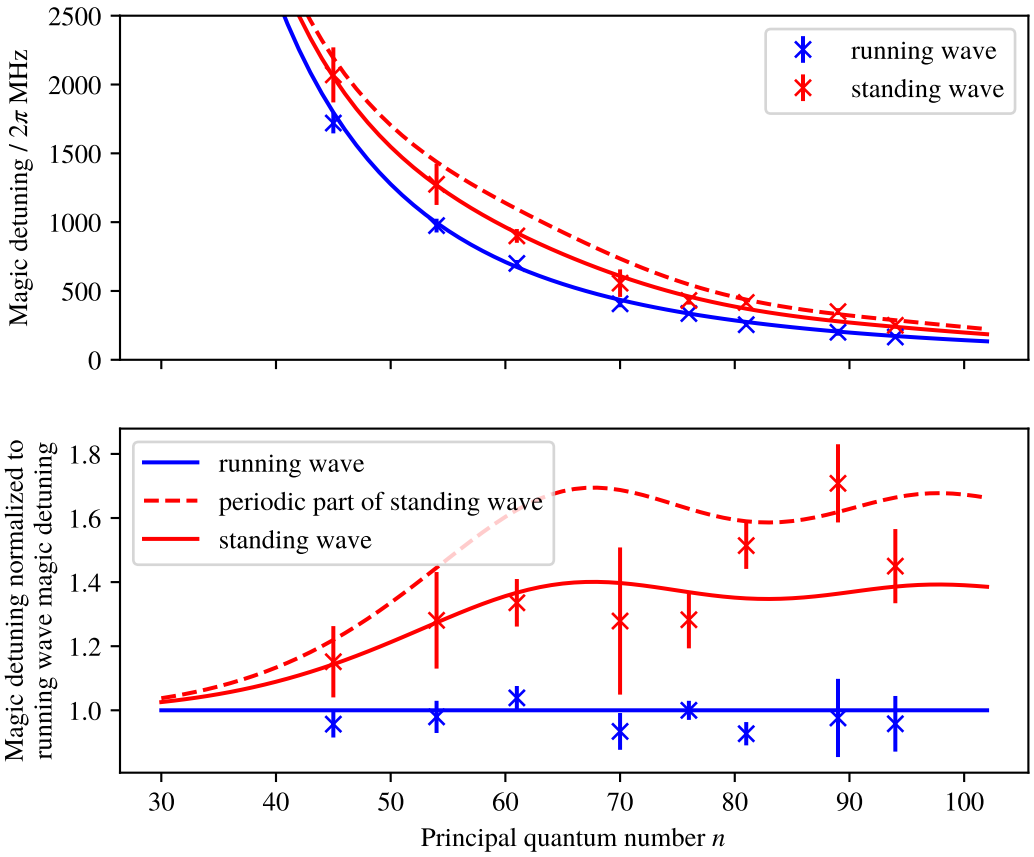

Figure 2.16: Trap detunings measured for optimal coherence time in the running and standing wave trap for different principal quantum numbers n (upper panel), normalized to the theoretical magic detuning for the running wave trap (bottom panel) to more clearly show the effect of the different trap geometries.

If the atom number used for the measurements for two different trap detunings differed, this could easily lead to a change of the shape of the coherence time curve, which could also shift the maximum. Since for higher Rydberg states, the measurement times were longer, and the sensitivity to density changes is larger, this could explain the discrepancies. However, measurements of the optical density of the prepared cloud over a few hours do not show any changes larger than 10 %.

There is thus no explanation with strong evidence for the discrepancies between theoretically expected optimal trap detunings for the standing wave and measurements, but the possible reasons for the discrepancy are not so implausible that they cast serious doubt on the calculations, especially since other experiments have found good agreement in the limiting case of negligible transverse intensity changes, i.e. large waists [19].

Nonetheless, the measured optimal detunings clearly show that the geometry of the trap must be taken into account when choosing the trap detuning, if the trapping light intensity fluctuates on lengths comparable to the size of the trapped Rydberg atoms.

2.4 Conclusion

In this chapter, the differences between trap potentials for ground state and Rydberg atoms were investigated. The influence of spatial changes of the intensity of a similar size as a Rydberg atom was calculated, and consequences for matching the trapping potentials for the ground and Rydberg state were found: In a standing wave trap, it is not possible to completely match the potentials, but there is still an optimal trap detuning that minimizes the spatial inhomogeneities of the differential light shift. Two experimental methods for finding this optimal trap detuning were investigated. It could not be found using a simple spectroscopic method, because not all influences on the linewidth of the absorption line of the ground to Rydberg state transition were reduced sufficiently during the measurements. Specifically, the probe photon number used led to too many Rydberg excitations in the cloud, broadening the transmission line. Photon storage experiments were found to be more sensitive to differential light shifts. They were successfully used to determine the optimal trap detuning. The measurement confirmed the theoretically predicted difference between two trap geometries.

CHAPTER 3

Effect of density on coherence time

Interactions between Rydberg and ground state atoms can lead to density-dependent dephasing [11]. In chapter 2, photon storage experiments were performed to observe the influence of differential light shifts on the dephasing rate. Lowering the density of the atom cloud was necessary to reduce the density-dependent dephasing. The enhancement of the coupling of Rydberg superatoms to light is given by the number of atoms N_b in the superatom as $\sqrt{N_b}$, which must all be within the blockade radius (see section 1.1). Higher coupling rates therefore require increasing the density of the atom cloud. The standing wave trap that has been implemented to reduce thermal dephasing confines the atoms to thin disk-shaped regions perpendicular to the axis of probe and control light. For the same number of atoms inside the blockade radius, the local density of the cloud is therefore increased compared to a cloud of homogeneous density.

Because of this large influence of density-dependent dephasing on the viability of the standing wave trap for increasing the coherence time of Rydberg superatoms, density-dependent effects are investigated in detail in this chapter. First, we will discuss how to measure cloud density in the experimental setup using absorption imaging (section 3.1). Measurements are presented showing that interactions between Rydberg atoms and ground state atoms take place for low principal quantum numbers at the typical densities used, leading to the formation of bound molecular states (section 3.2). The density dependence of the dephasing rate at high principal quantum numbers is discussed (section 3.3).

3.1 Measuring cloud density with absorption imaging

From absorption images, the column density of atoms at each point of the image can be determined if the absorption cross section of a single atom is known. Estimating the density of the cloud from the column density additionally requires information about the distribution of atoms in the direction perpendicular to the imaging plane. We use the approach of calculating this from the trap potentials and the temperature of the atoms. The trap potentials are given by the trap beam powers and sizes. Since this calculation results in the full 3D relative density distribution, only the total number of atoms is necessary to calculate the absolute density, which is the integral of the column densities over the image. The temperature of an atom cloud can be measured using time-of-flight imaging of the expansion of the atom cloud.

In the RQO experiment, there are two imaging setups, each consisting of an imaging beam, magnifying optics, and a camera. The two setups allow taking images of the cloud in two perpendicular planes. Only

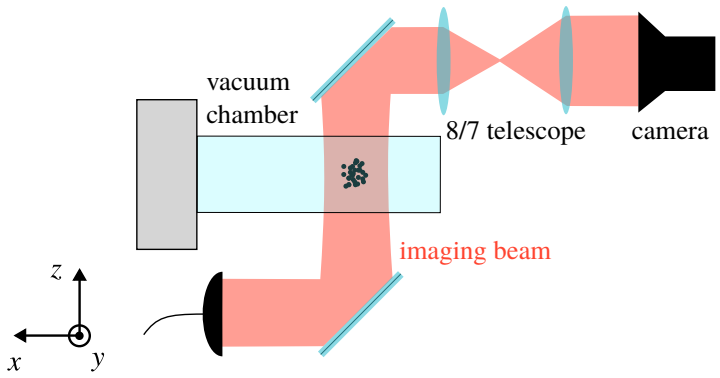

Figure 3.1: Vacuum chamber with optics for imaging of the atoms in the horizontal (x-y) plane. The imaging beam has a waist radius at the atoms of 2.3 mm, significantly larger than the atom cloud. The atoms are located close to the point of peak intensity.

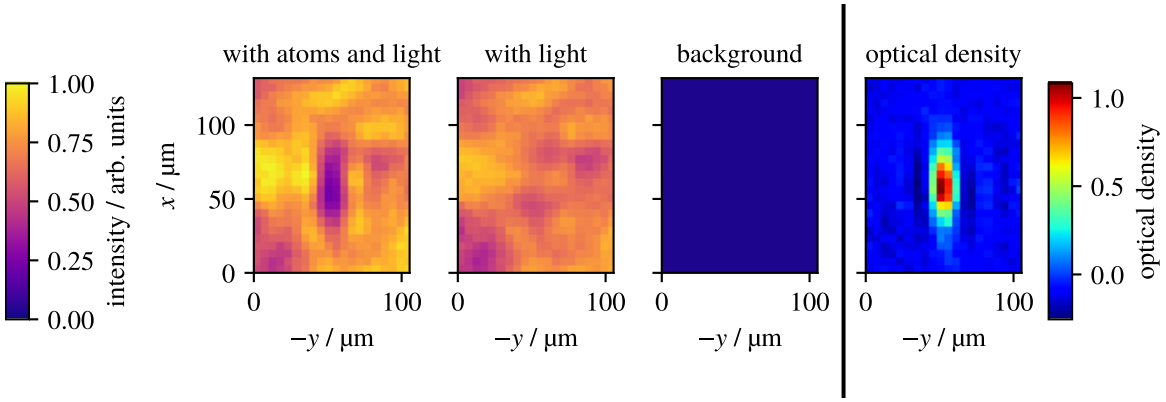

Figure 3.2: The left two images show the intensity measured with the same power of the imaging laser with atoms and without atoms. The shadow cast by the atoms is clearly visible. The third image from the left shows the intensity when the imaging laser is off. The rightmost image shows the optical density of the cloud calculated from the left three images. The peak optical density for the imaging light of the cloud in this image is 1.08.

images of the horizontal plane are used in this thesis. The imaging setup for the horizontal plane is shown in figure 3.1

To determine the optical density of the atom cloud, three images are taken: Two with the imaging laser on, with and without atoms, and one with the imaging laser off. An example of three such images is shown in figure 3.2. The transmission is given by

$$T = \frac{I_{\text{with atoms}} - I_{\text{background}}}{I_{\text{without atoms}} - I_{\text{background}}}$$

and the optical density is $-\ln(T)$. Negative optical densities can occur when there is more light in the image with atoms than in the image without atoms. This may happen when the intensity of the imaging laser fluctuates between the images with and without atoms. When multiple absorption images are averaged, it is important to not cut off negative optical density values, to make it possible for the these

fluctuations to average to zero.

From these absorption images, the atom number in the cloud and its temperature is determined.

3.1.1 Temperature measurement

The temperature of the atom cloud is measured by time-of-flight imaging, as described e.g. in ref. [31]. For the temperature measurement, the atom density distribution is approximated to be of Gaussian shape, which is the case for a thermal cloud in a harmonic trap. The standard deviations of the Gaussian density distribution can differ in different directions, if the atoms are in a trap with different trap frequencies along the three axes. The different directions are considered separately by integrating the column density image along one axis. A Gaussian-shaped atom cloud is still of Gaussian shape after freely expanding for some time t. If its initial standard deviation is σ_0, after expansion for a time t the standard deviation is

$$\sigma(t) = \sqrt{\sigma_0^2 + \sigma_v^2 t^2}. \tag{3.1}$$

The expansion rate at large times is σ_v. If the cloud was in thermal equilibrium before the expansion, the expansion rate is related to the temperature by $m\sigma_v^2 = k_B T$. Eq. 3.1 can be linearly approximated by its asymptote for large expansion times. However, due to the small number of atoms in our cloud, the possible free expansion times after which the cloud density is still sufficient to determine a cloud size is not large enough to allow for this simplification. We obtain the temperature by determining the standard deviations of the cloud after different expansion times from the fit of a Gaussian function $A \exp\left(-x^2/(2\sigma^2)\right)$ to the summed column density profiles. A fit of eq. 3.1 to the standard deviations then yields the temperature of the cloud.

Measurements of the temperature conducted for the standing wave trap, the running wave trap, the crossed beam trap, and the dimple trap are shown in figure 3.3. The different maximal expansion times are determined by when the absorption signal gets too small to measure. While the approximation of a Gaussian cloud holds well for the running wave trap, crossed beam trap, and dimple trap, it does not hold at all for the standing wave trap, where the cloud is actually made up of many very short clouds separated by the period of the standing wave trap potential of 0.5 µm. Because this is much smaller than the resolution of the imaging system, the absorption images do not capture this density modulation, but only the average column density in each pixel. Since the cloud expands by more than 10 µm, which is much larger than the distance between lattice sites of the standing wave trap, the initial density modulations should not influence the temperature measurement. For the purpose of determining the temperature of the cloud, it may be treated as having a Gaussian density distribution, with trap frequencies corresponding to the intensity envelope of the standing wave due to the Gaussian shape of the beams. The absorption images confirm this, as indicated by the small error bars of the standard deviation determined from Gaussian fits shown in figure 3.3.

Two sets of cloud sizes are obtained, along the y-axis and along the x-axis, The running wave, standing wave and crossed beam traps have larger trap frequencies in the x- than in the y-direction (this only holds for the envelope of the standing wave trap). For the dimple trap, the trap frequency in the y-direction is larger than in the x-direction. This leads to different initial cloud sizes. For a thermal cloud, the rate of expansion should be independent of the direction in which the atoms move. In figure 3.3, we see that this is the case for the standing wave trap, where the temperatures measured for both directions agree, for both trap depths. However, for the running wave, crossed beam, and dimple traps, the temperatures in

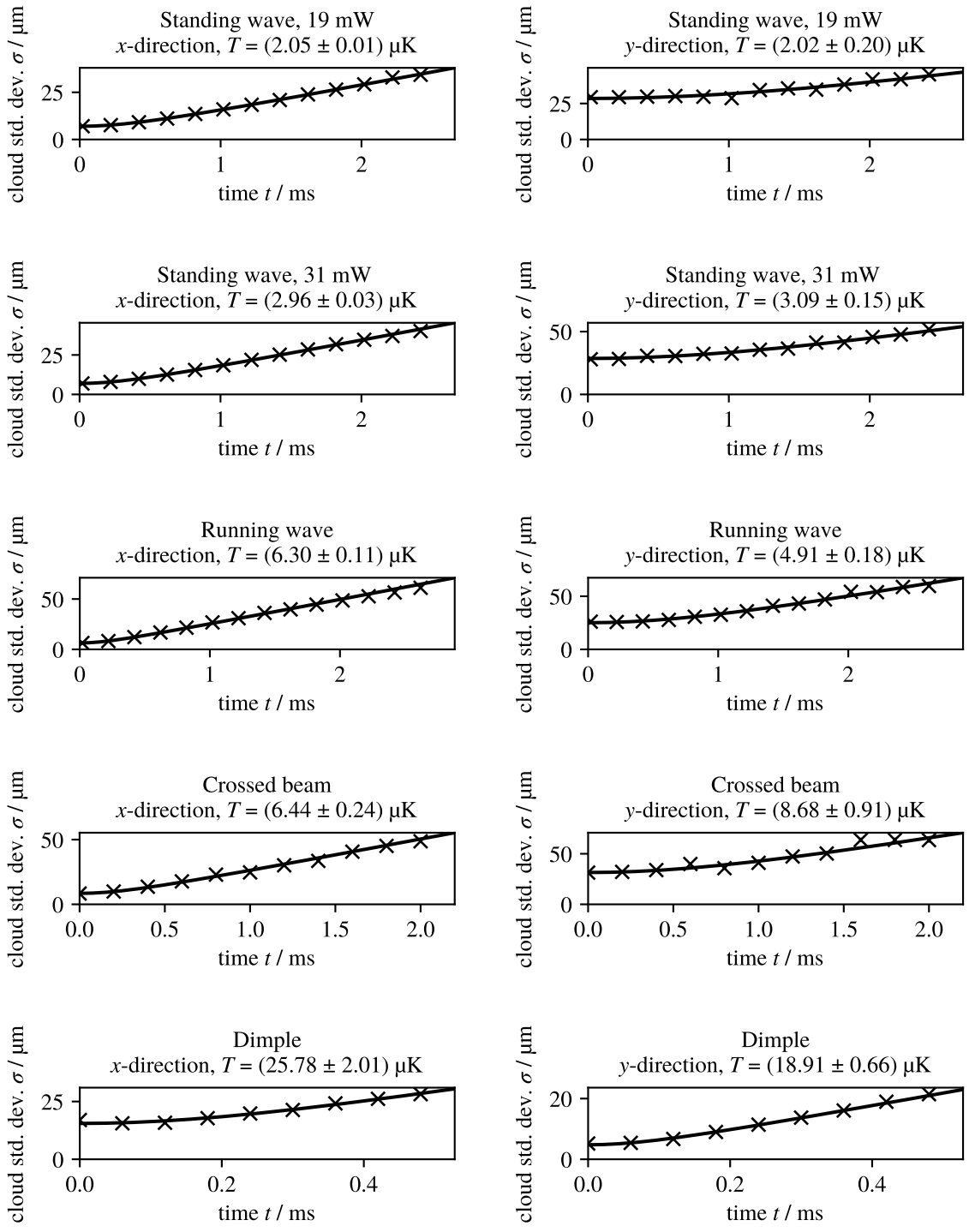

Figure 3.3: Temperature measurements for the standing wave, running wave, crossed beam, and dimple traps. For the standing wave trap, the temperature has been measured for two different beam powers. The size of the cloud in the x- and y-direction is shown. Eq. 3.1 is fitted to the data to extract the temperature.

the two directions differ significantly.

The reasons for the discrepancies of the temperature along the two axes is not clear. If the two temperatures differ, the temperature along the direction in which the cloud is smaller initially is used, because in this direction there are more data points in the linear expansion regime. The reason for doing this is that the temperature information is contained only in the slope σ_v of the asymptote of $\sigma(t) = \sqrt{\sigma_r^2 + \sigma_v^2 t^2}$.

Since experiments in the standing wave trap were done at a trap power of 25 mW, a temperature of (2.5 ± 0.2) µK is used. For the running wave trap, we use (6.30 ± 0.11) µK, for the crossed beam trap we use (6.44 ± 0.24) , and for the dimple trap (18.91 ± 0.66) µK, unless otherwise specified.

Atom number

The atom number is determined from the saturation-corrected cross section $\sigma = \frac{3\lambda^2}{2\pi} \frac{1}{1+I/I_{\text{sat}}}$ [32] for the atom light interaction. The column density of atoms in a region with a given optical density is OD/σ. The number of atoms in a pixel of size $d_x d_y$ is $\text{OD} \cdot d_x d_y / \sigma$. The total atom number is the sum over all pixels.

When there is even a small background of absorption, this can have a significant effect on the atom number when the region over which the optical density is summed is chosen to be significantly larger than the cloud. In this case, it can be advantageous to replace the sum over all pixels by the Gaussian fits already done for the cloud size measurement, which allows subtracting this background. This is done for all atom numbers determined from absorption imaging.

3.1.2 Uncertainties

The imaging setup was designed to monitor the position of the atom cloud in the chamber and to determine the temperature of the cloud, not for precise measurements of the atom number. The small cloud used for superatoms only covers a small part of the sensor area (no more than 10×10 pixels) of the camera, since there is almost no magnification (factor $8/7$). The intensity of the imaging light is not stabilized, and since intensities larger than the saturation intensity are used, this affects the measured optical densities. Since the imaging light does not propagate along the same axis as the excitation light, but the magnetic field must be oriented along this axis to pump the atoms into the stretched states and address the closed probe transition, the imaging light is a mixture of σ^+, σ^-, and π polarized light, so imaging is not done on a single transition, which would be necessary to be able to compute the atom number from the amount of absorbed light.

All of this means that we will only be able to make very qualitative statements about the density dependence of dephasing rates. It is possible to clearly distinguish larger and smaller atom numbers in an individual measurement set, but there is a large systematic error of the atom number that is prone to changing over longer times. Temperature measurements are not affected by the uncertainty of the atom number, since they only depend on the size of the atom cloud.

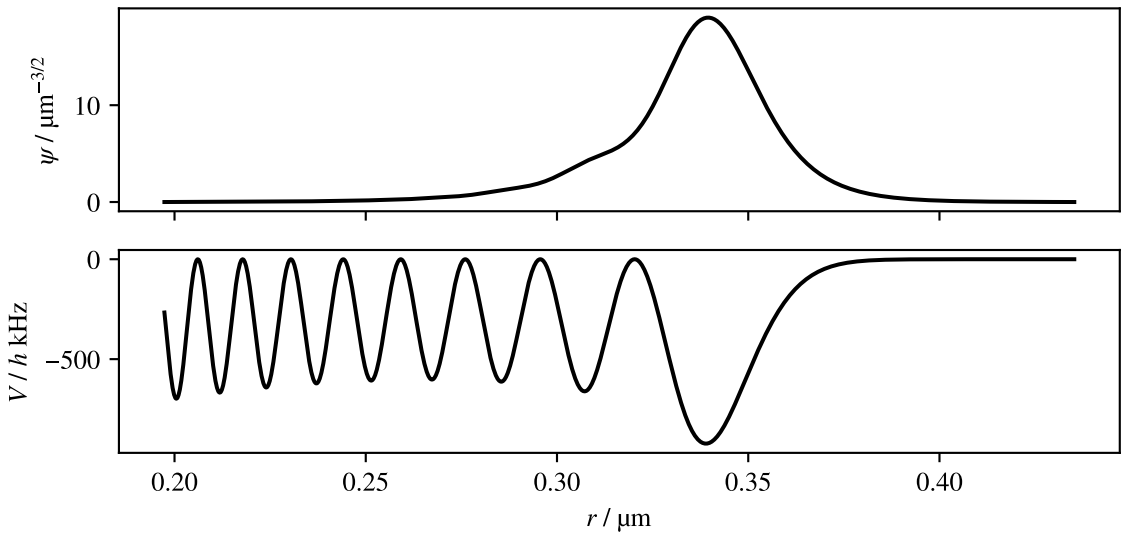

Figure 3.4: Bottom: Molecular potential whose shape is given by the Rydberg electron probability density (eq. 3.2). Top: The molecular wavefunction of the lowest bound state of this the molecular potential. The energy of this state is $-596\ h$ kHz using $a = -15.7\ a_0$

.

3.2 Molecules of a Rydberg atom and ground state atoms

The Rydberg electron can scatter with ground state atoms surrounding a Rydberg atom. This can be described by an interaction potential [33]

$$V(\vec{r}) = \frac{2\pi\hbar^2 a}{m_e}|\psi_n(\vec{r})|^2, \tag{3.2}$$

given for the distance $\vec{r}$ between Rydberg atom core and ground state atom, the scattering length a between an electron and a ground state atom, and the Rydberg electron wavefunction ψ_n. This potential has the same shape as the Rydberg electron probability density, and at very low temperatures, where only s-wave scattering is relevant and the scattering length is negative, it allows bound states. Because we only use Rydberg atoms in S-states, the wavefunction and the molecular potential are spherically symmetric, so V really only depends on the absolute value of the distance between the ion core and the ground state atom, $r = |\vec{r}|$. These states are molecules formed out of one Rydberg atom and one or more ground state atoms. They have been observed previously at the RQO experiment in photon storage experiments [34]. The value of the triplet scattering length between the Rydberg electron and a ground state Rubidium atom is from theory only known to be between $-13\ a_0$ and $-17\ a_0$ [33], but has been determined experimentally from a fit to measured Rydberg molecule binding energies to be $-15.7\ a_0$ [35].

3.2.1 Calculation of wavefunctions and binding energies

The molecular potential from eq. 3.2 is able to host bound states. The wavefunctions and energies of these states may be found numerically, by solving the time-independent Schrödinger equation as an eigenvalue problem using a shooting method.

The time-independent Schrödinger equation

$$\hat{H}\psi(\vec{r}) = \left(-\frac{\hbar^2}{2m}\vec{\nabla}^2 + V(\vec{r})\right)\psi(\vec{r}) = E\psi(\vec{r})$$

may be solved for the central potential eq. 3.2 by solving, for zero angular momentum [36, p. 121],

$$\left(-\frac{\hbar^2}{2m}\frac{\mathrm{d}^2}{\mathrm{d}r^2} + V(r) - E\right)u(r) = 0. \tag{3.3}$$

Then the radial part of the wavefunction is given by $R(r) = u(r)/r$.

For a given energy, equation 3.3 may be solved using any numerical method for integrating ordinary differential equations. We use the function `solve_ivp` from the SciPy Python library. Since we do not know the binding energies yet, we have to solve the eigenvalue problem given by eq. 3.3 and the boundary conditions $u(0) = 0$ and $\lim_{r\to\infty} u(r) = 0$. This is done using a shooting method, integrating inwards since the potential is only zero outside of some radius r_0. It consists of the following steps [37]:

1. Choose an initial guess for the energy that would classically give a bound state of the potential.
2. Choose an integration starting position r_0 that is in a region where the potential is close to 0, so a bound state is not expected to have a significant probability density there.
3. Choose $\psi(r_0) = 0$ and some arbitrary $\mathrm{d}\psi/\mathrm{d}r$, which determines the normalization of the found wavefunction. The normalization can be corrected later.
4. The boundary condition for $r \to \infty$ is fulfilled by the choice of initial values at r_0. Now, iteratively find a value for E for which the boundary condition at $r = 0$ is fulfilled as follows:
   a) Solve the the radial Schrödinger equation 3.3 for the current energy guess using a numerical integrator for ordinary differential equations (ODEs). We use `solve_ivp` from the SciPy Python library [38].
   b) If the value of the solution does not fulfill the boundary condition at $r = 0$ yet, i.e. $\psi(0) \neq 0$, change the energy guess. The energy should not be adjusted blindly, but by using a root finding algorithm, e.g. Newton's method. We use `root_scalar` from the SciPy Python library [38].
   c) Repeat until the boundary condition at $r = 0$ is fulfilled.
5. Normalize the wavefunction.

This procedure is sometimes summarized as using the Numerov method to find binding energies. The Numerov method is a numerical integration procedure that is particularly efficient for ODEs of the form of the time-independent Schrödinger equation, but it is possible to use any other numerical method for integrating ODEs. The crucial part of the algorithm is the shooting method for solving the boundary

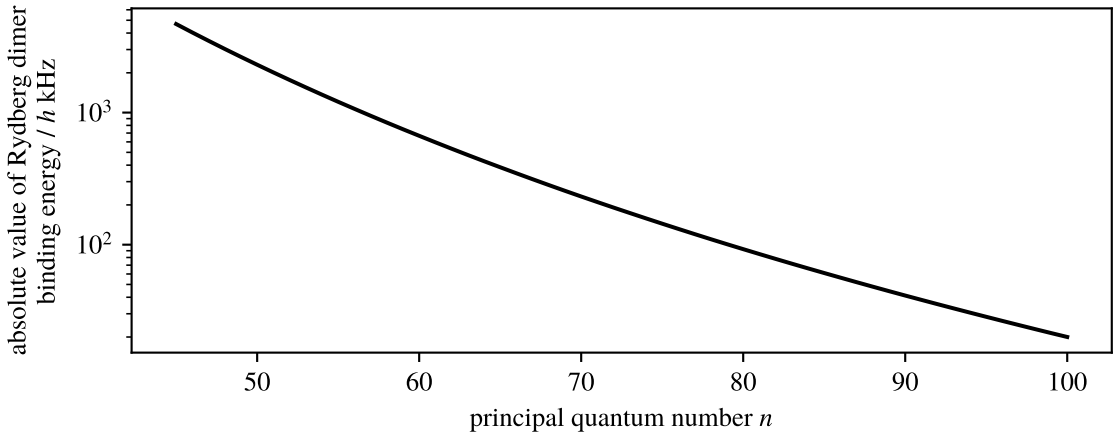

Figure 3.5: This curve shows the Rydberg dimer binding energies computed as described in the main text using the Rydberg wavefunctions and the scattering length $a = -15.7a_0$. The calculated binding energies are approximately consistent with a scaling $\propto n^{-6}$.

value problem. The same method may be used to find Rydberg wavefunctions, but for this calculation, they have been calculated using the ARC Python library [25].

For the Rydberg state 61S, the lowest energy solution has been found using this method. The found wavefunction is shown in figure 3.4. The binding energy of this state is found to be -596 h kHz using $a = -15.7$ a_0.

The dimer binding energy has been computed in this way for Rydberg S-states with n between 40 and 100. The results are shown in figure 3.5, they are consistent with the same calculation done in ref. [39], as well as with the binding energies measured in ref. [34]. The calculation shows the expected scaling of the binding energy with n^{-6} [39], so at high Rydberg states that are suitable for creating superatoms, the binding energy is very small. At high n, Rydberg molecules of one Rydberg atom and multiple ground state atoms, whose binding energy is a multiple of the binding energy of a molecule consisting of a single ground state atom and a Rydberg atom, can be excited. This can lead to a shift and broadening of the Rydberg line, and can cause dephasing (dephasing by inhomogeneous shifts is discussed in detail in section 4.2) [11]. The first case of discrete molecular lines is explored in section 3.2.2, the second case of dephasing in section 3.3.

3.2.2 Measurement of oscillations in storage efficiency due to molecules

In photon storage, the formation of Rydberg dimers is possible when the binding energy of the dimer is smaller than the bandwidth of the EIT peak. In this case, there is a beating of the storage efficiency at the frequency corresponding to the dimer binding energy, as modeled in ref. [34], where these oscillations were measured in free space. We make a slight modification to the model presented there, by taking motional rephasing in the lattice into account. Instead of a Gaussian decay of the storage efficiency, motional rephasing leads to instead an oscillation of the storage efficiency at the trap frequency. The detailed shape $f_{T,\omega_{\text{trap}}}(t)$ of the rephasing has been computed in section 1.2. We simply replace the

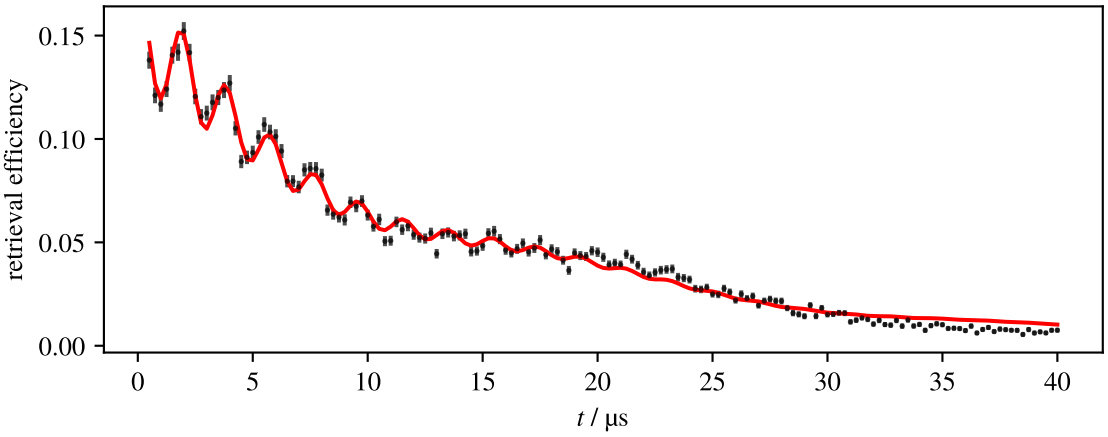

Figure 3.6: The retrieval efficiency for photon storage at principal quantum number $n = 61$ oscillates due to the formation of Rydberg molecules as explained in the main text. The data is fitted with eq. 3.4, where the fitted parameters are the dimer fraction n_D, the lifetimes of Rydberg atoms τ_R and Rydberg dimers τ_D, the amplitude of the signal A, and the dimer binding energy E_b (see main text). The other parameters of the model curve are fixed: Temperature $T = 2.5\,\mu\text{K}$ and trapping frequency $\omega_{\text{trap}} = 2\pi \cdot 50\,\text{kHz}$, which were obtained from independent measurements. The fitted dimer binding energy is $E_b = -h \cdot (518 \pm 2)\,\text{kHz}$.

Gaussian decay in the existing model with this, and obtain

$$\eta(t) = A f_{T,\omega_{\text{trap}}}(t) \left[(1 - n_D) e^{-t/\tau_R} + n_D e^{-t/\tau_D} \cos\left(E_b t/\hbar\right) \right]. \tag{3.4}$$

The binding energy extracted from the fit is $E_b = -h \cdot (518 \pm 2)\,\text{kHz}$, differing from the $E_b = -h \cdot 596\,\text{kHz}$ obtained from the calculation. The fitted binding energy is in decent agreement with previous measurements, which found an oscillation frequency of $(511 \pm 3)\,\text{kHz}$ [34]. The fitted binding energy corresponds to a scattering length of $a = -14 a_0$ to be used in the calculation.

3.3 Effects of shifting and broadening of the Rydberg line at high densities

The necessity of reducing the density to obtain large coherence times in photon storage experiments was noticed while trying to measure the effects of differential light shifts in chapter 2. This motivated a more systematic measurement of the density-dependence of the dephasing rate.

The results of these measurements of the coherence time in photon storage experiments at different peak densities is shown in figure 3.7. The experiments have been performed with a small cloud in the dimple trap, i.e. at conditions where the cloud is fully blockaded and it would be possible to observe single photon Rabi oscillations. The peak density is calculated from the trapping potentials, the temperature, and the atom number. The latter two were determined from absorption imaging. At two Rydberg states with large principal quantum numbers, $n = 89$ and $n = 100$, we find an approximately linear dependence of the dephasing rate on the peak density. When extrapolating the dephasing rate to zero density using a linear fit, we find a dephasing rate due to other mechanisms of $(1.03 \pm 0.09)\,\text{MHz}$

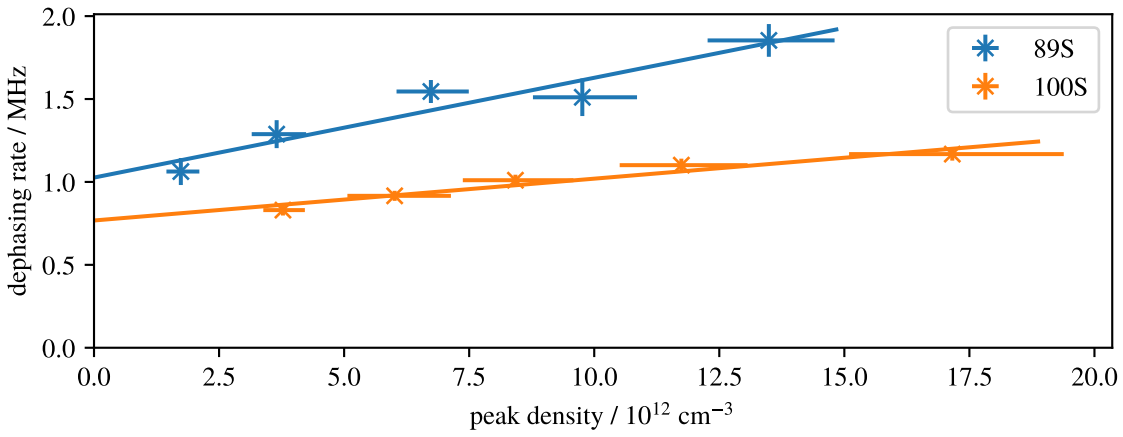

Figure 3.7: Dephasing rate for photon storage experiments performed with a cloud loaded into the dimple trap, at different peak densities, and for two different Rydberg states. A linear fit is performed to extrapolate the dephasing rate to zero density.

for $n = 89$ and of (0.77 ± 0.04) MHz for $n = 100$. The density-dependent dephasing rates extracted from the fits are $(0.06 \pm 0.01) \times 10^{12}$ MHz cm^3 for $n = 89$ and $(0.03 \pm 0.01) \times 10^{12}$ MHz cm^3 for $n = 100$.

A very similar[1] experiment has been performed in ref. [40], which also finds a linear dependence of the dephasing rate on density. It finds a zero-density dephasing rate for $n = 100$ of 0.8 MHz and a density-dependent dephasing rate of 0.17 MHz µm^3. The zero-density dephasing rate found in our measurement for $n = 100$ is compatible with the results of this experiment. This is not necessarily expected, since non-density-related dephasing mechanisms could well give different contributions for these different experiments. The density-dependent contribution is different by a factor of 6. This would require that the density of the cloud used in our experiment is much more homogeneous, to reduce inhomogeneous density shifts of the Rydberg line, or overall much less dense, such that fewer Rydberg molecules lead to less broadening of the Rydberg line. As noted in section 3.1, we expect the atom number measurements to have a large systematic error. If the atom numbers measured within one set of measurements are consistently off by a constant factor, this would only affect the slope, but not the extrapolation to zero density. If there is also a systematic offset of the measured atom number from the real one, this would also affect the extrapolation to zero density. Additionally, the peak density is sensitive to changes of the trap geometry, so an underestimation of the dimple beam waists could lead to overestimating the peak density. It seems likely that these systematic uncertainties explain the deviation.

The difference of the zero-density dephasing rates for $n = 89$ and $n = 100$ may be due to principal quantum number dependent dephasing mechanisms or due to varying systematic offsets of the measured atom number between the two sets of measurements. Possible candidates for fundamental dephasing mechanisms are discussed in detail in section 4.2, but there is no n-dependent mechanism that would be relevant in photon storage experiments. Because all lasers are off during the storage time, the admixture of fast-decaying states cannot play a role. Thus it is most likely that the difference is due to the systematic errors of the atom number measurements.

[1] The experiment performed in ref. [40] also used Rb-87, but the 100S Rydberg state was excited via the $5P_{1/2}$ state instead of the $5P_{3/2}$ state and with copropagating probe and control beams. The relevant measurement is shown in fig. 4 of the paper.

A difference of the density dependent dephasing rate between the two Rydberg states is expected, since the Rydberg molecule binding energy changes. If the number of excited molecular states is limited by the excitation bandwidth, which is smaller at $n = 100$ because of the smaller dipole matrix elements of the optical transition to the Rydberg state, the lower density-dependence of the dephasing rate at $n = 100$ compared to $n = 89$ is expected.

Overall, the large systematic errors of the density make the results obtained in these measurements inconclusive. No quantitative statement regarding the dependence of the dephasing rate on density beyond an increase for larger densities can be made.

3.4 Conclusion

In this chapter, the observation of molecular oscillations of the storage efficiency in photon storage experiments at a principal quantum number of $n = 61$ as evidence of Rydberg atom ground state atom interactions have been presented. The molecular binding energy is consistent with literature values. The simple model for motional dephasing due to classical motion of atoms in the standing wave lattice sites describes an additional observed oscillation of the storage efficiency very well. Measurements of the dephasing rate due to inhomogeneous shifts and broadening of the Rydberg line at higher quantum numbers yielded no conclusive results, only showing that the dephasing rate increases at higher densities, but did not allow making statements of the quantitative dependence on density because of inaccurate measurements of the atom number.

CHAPTER 4

Fundamental limits on the coherence time of Rydberg superatoms

We have investigated the details of minimizing differential light shifts in the standing wave trap and seen an overall increase of coherence times in photon storage experiments in the standing wave trap compared to a running wave trap in chapter 2, but we have also seen the effects of increased density in photon storage experiments in chapter 3. In this chapter, we return to the single-photon Rabi oscillations of Rydberg superatoms and try to give an answer to the question posed in chapter 1: Does the magic wavelength lattice trap lead to an overall decrease of the dephasing rate of single-photon Rabi oscillations?

Measurements of single-photon Rabi oscillations in the standing wave trap and in the dimple trap are described in section 4.1. Because they do not show an improvement of β_{coh}, an attempt is made to give quantitative estimates of different contributions to the dephasing rate. These estimates are presented and compared to measurements in section 4.2.

4.1 Comparison of single-photon Rabi oscillations in the dimple trap and the magic wavelength lattice trap

As described in section 1.1, a Rydberg superatom driven with a few-photon light field performs Rabi oscillations between the collective ground and excited states. The Rabi oscillations of the superatom lead to oscillations of the transmitted power.

We prepare a superatom in the dimple trap at $n = 89$. From an absorption image (section 3.1), the standard deviation of the density distribution of the atom cloud prepared in the dimple trap in the y-direction is measured to be $(4.8 \pm 0.1)\,\mu\mathrm{m}$. The temperature of the cloud is measured to be $(18.5 \pm 0.3)\,\mu\mathrm{K}$, where we use the temperature obtained from the expansion along the y-direction, in which the initial size of the cloud is smaller. In the x- and z-directions, the size of the excited ensemble is limited by the probe waist of $5\,\mu\mathrm{m}$. The chosen principal quantum number is relatively low for a superatom experiment, where typically at least $n = 100$ is used. It was chosen as a compromise between large density-dependent dephasing at high quantum numbers and a sufficiently large blockade radius for the cloud to behave as a superatom. Whether the cloud is fully blockaded will be apparent from the number of absorbed photons.

The transmission of the exciting mode by the superatom is measured at different input photon rates,

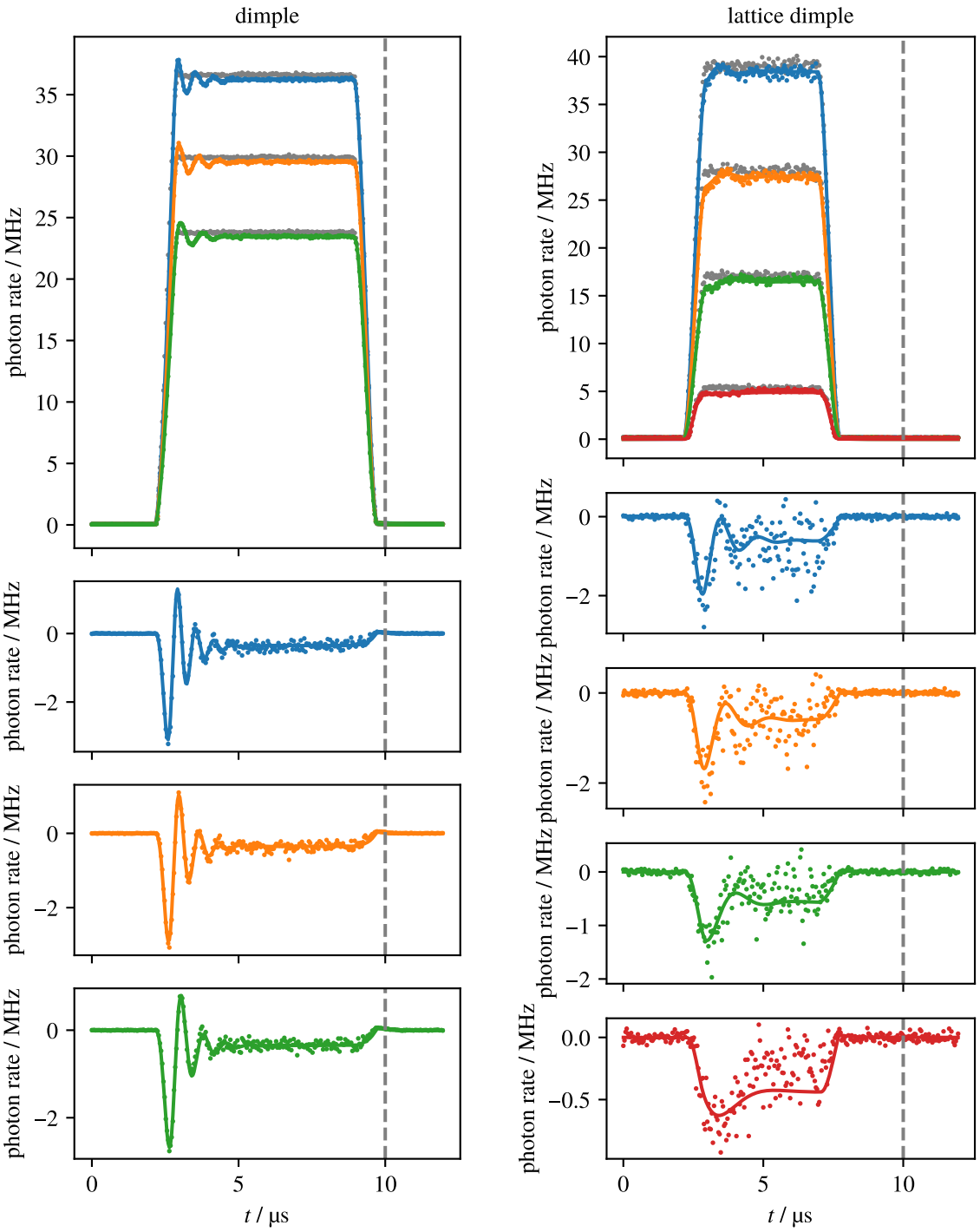

Figure 4.1: This figure shows the transmitted photon rate in single-photon Rabi oscillation experiments, for the dimple (left) and lattice dimple (right) configurations. The parameters of the fitted model are, for the dimple (left): $\kappa = (0.72 \pm 0.01)$ MHz, $\Gamma = (0.41 \pm 0.01)$ MHz, $\gamma_D = (2.11 \pm 0.05)$ MHz, $\beta_{\mathrm{coh}} \approx 0.22 \pm 0.06$, and for the lattice dimple (right): $\kappa = (0.14 \pm 0.01)$ MHz, $\Gamma = (0.97 \pm 0.05)$ MHz, $\gamma_D = (0.97 \pm 0.02)$ MHz, $\beta_{\mathrm{coh}} \approx 0.07 \pm 0.08$. Missing photons in the first half-period of the oscillations are in the dimple (left) 0.85, 0.71, and 0.80, and in the lattice dimple (right) 0.98, 0.89, 0.97, and 0.97 (for increasing photon rates, i.e. from bottom to top)

to be able to measure the photon-rate independent coupling κ. The results are shown in the left panels of figure 4.1. Oscillations of the transmitted photon rate are clearly visible. The effective model from section 1.1 describes the data well, and from a fit we find $\kappa = (0.72 \pm 0.01)\,\mathrm{MHz}$, $\Gamma = (0.41 \pm 0.01)\,\mathrm{MHz}$, and $\gamma_D = (2.11 \pm 0.05)\,\mathrm{MHz}$, which corresponds to $\beta_{\mathrm{coh}} \approx 0.22 \pm 0.06$, comparable to earlier measurements done at the RQO experiment [1].

Summing the difference between the signal with and without atoms up to the time where the Rabi phase reaches π as determined from the fit gives the number of absorbed photons. We find, for the different peak photon rates, 0.85, 0.71, and 0.80 missing photons. This is compatible with the cloud being fully blockaded and absorbing only one photon at a time. The deviation from 1 is due to the quick dephasing of the Rabi oscillations.

A first test measurement of whether there is an immediate improvement of β_{coh} using the magic lattice trap has been made by transferring the atom cloud from the crossed beam trap into the dimple trap, and from there into the standing wave trap. The dimple trap is then turned off. Loading via the dimple trap is necessary to reduce the size of the cloud in the y-direction. While confining the atoms along the x- and z-directions by turning on the crossed beam trap between experiments is necessary in the dimple trap, this is not needed in the standing wave trap. To differentiate this configuration from the large cloud loaded directly from the crossed beam trap into the standing wave trap, we call this configuration lattice dimple.

Absorption images of the lattice dimple cloud yield a standard deviation of the cloud's density distribution in the y-direction of $(5.4 \pm 0.3)\,\mu\mathrm{m}$, and a temperature of $(6 \pm 1)\,\mu\mathrm{K}$ ($(5.7 \pm 0.6)\,\mu\mathrm{K}$ in the x- and $(6.5 \pm 1.1)\,\mu\mathrm{K}$ in the y-direction. The experiment was performed at a principal quantum number $n = 94$, again as a compromise between blockade radius and density-dependent dephasing.

The measurement results for this configuration are shown in the right panel of figure 4.1. The scattering of the datapoints is due to insufficiently many repetitions of the measurement. Oscillations of the transmitted photon rate are visible, but the transmitted photon rate never increases above the input photon rate. The measurement has been performed at four instead of three different input photon rates, which are overall lower than in the measurement in the dimple. The measurement in the dimple shown in the left panels of figure 4.1 was done later than the one in the lattice dimple shown here, when it had been found that three different input photon rates are sufficient to determine the model parameters, allowing more repetitions at these rates to be gathered. The overall higher photon rates lead to more visible oscillations in each measurement, which make the determination of the dephasing rate more accurate. The measurement in the lattice dimple configuration has not been repeated after these improvements were made, which is why this measurement that leaves obvious room for improvements is presented here.

The model fit gives $\kappa = (0.14 \pm 0.01)\,\mathrm{MHz}$, $\Gamma = (0.97 \pm 0.05)\,\mathrm{MHz}$, and $\gamma_D = (0.97 \pm 0.02)\,\mathrm{MHz}$, which corresponds to $\beta_{\mathrm{coh}} \approx 0.07 \pm 0.08$. However, the data is too noisy to perform a confident fit. The large reduction in κ is caused by a much smaller atom number due to losses during the transfer to the standing wave trap. From absorption imaging, we obtain an atom number of $(1.20 \pm 0.08) \times 10^4$ for the dimple and $(1.9 \pm 0.4) \times 10^3$ for the lattice dimple. The reduction of the number of atoms is qualitatively consistent with the observed lower κ.

In summary, a first attempt at measuring single-photon Rabi oscillations in the lattice dimple suggests that β_{coh} is much worse than in the dimple. However, a less noisy measurement would be required to make a definite conclusion. In order to understand whether we expect any improvement of β_{coh} in the lattice dimple, an attempt is made to model expected dephasing rates in the next section 4.2.

4.2 Decoherence mechanisms for single-photon Rabi oscillations

In this section, an overview of the dephasing mechanisms encountered so far is given, and an attempt is made to obtain a quantitative estimate of their contributions to the overall dephasing rate in the dimple and lattice trap at different Rydberg states and densities. We for now only look at dephasing mechanisms that cannot be avoided by technical improvements of the experiment.

In the entire section, we consider a cloud of N atoms at temperature T in an optical trap with ground state potential U_g and Rydberg state potential U_r, driven by control and probe lasers with beam geometries as described in section 1.3.

The atom number density distribution is given by the Boltzmann distribution as

$$n(\vec{r}) = N \frac{e^{-U_g(\vec{r})/(k_B T)}}{\int \mathrm{d}^3 r\, e^{-U_g(\vec{r})/(k_B T)}}.$$

such that $\int \mathrm{d}^3 r\, n(\vec{r}) = N$.

Before looking at dephasing rates, the coupling rate κ is calculated for our experimental conditions, since this is necessary to compute β_{coh} – changing the experimental conditions to reduce dephasing e.g. by lowering the density of the cloud might reduce the coupling rate more than the dephasing rate.

4.2.1 Calculation of the coupling rate κ

The enhancement of the Rabi frequency by $\sqrt{N_b}$ given in section 1.1 assumes that the single-atom Rabi frequency Ω_R for all N_b atoms in the ensemble is the same. Because of the finite size of the beams, this is not the case. This may be taken into account by looking at the collective excited state for the case of inhomogeneous excitation. With $\Omega_R(0)$ the peak Rabi frequency at the center of the overlapping probe and control beams, and $\Omega_{R,i}$ the Rabi frequency at the location of the atom i, the collective excited state is

$$|W\rangle = \frac{1}{\sqrt{\sum_{i=1}^{N} \Omega_{R,i}^2}} \sum_{i=1}^{N} \Omega_{R,i} \, |g_1, \ldots, r_i, \ldots, g_N\rangle \tag{4.1}$$

for which the collective Rabi frequency is $\sqrt{N_{\mathrm{eff}}}\Omega_R(0)$, when defining an effective atom number

$$N_{\mathrm{eff}} = \sum_{i=1}^{N} \frac{\Omega_{R,i}^2}{\Omega_R^2(0)}$$

(compare to ref. [4]). The sum runs over all atoms, not just those in the blockade volume. In the dimple trap, the cloud is smaller than the blockade radius in one direction, but larger in the others. The ensemble is formed only by the atoms that are within the excitation beam. Weighing the superposition state by the Rabi frequencies accounts for this.

For a given atom number density $n(\vec{r})$, the effective atom number can be computed by replacing the

sum by an integral, as

$$N_{\text{eff}} = \int \mathrm{d}^3 r \, n(\vec{r}) \frac{\Omega_R^2(\vec{r})}{\Omega_R^2(0)}.$$

Using this effective atom number, the coupling rate κ can be calculated.

From $2\sqrt{\kappa R_{\text{in}}} = \sqrt{N_{\text{eff}}}\Omega_R$ (see section 1.1), and using the probe-light coupling constant $g_0 = \Omega_p/\sqrt{R_{\text{in}}}$, we find

$$\kappa = \frac{N_{\text{eff}}\Omega_R^2}{4R_{\text{in}}} = \frac{N_{\text{eff}}\Omega_c^2 g_0^2}{16\Delta^2}.$$

4.2.2 Motional dephasing

The rate of motional dephasing has already been calculated in the motivation for the magic wavelength lattice in section 1.2. Since other dephasing rates have turned out to be much larger than the thermal one at the conditions investigated, we can approximate the thermal dephasing rate with the free space Gaussian thermal dephasing even in the lattice for now. If it is managed to reduce the other dephasing rates significantly, the correction for the lattice trap may be used.

4.2.3 Inhomogeneous light and density shifts

We are aware of two sources of inhomogeneous lineshifts: The first one are spatially inhomogeneous differential light shifts of the ground to Rydberg state transition due to the potential created by the trap lasers (as given in chapter 2), but also due to the potential created by the control beam. The second source are spatially inhomogeneous shifts due to the varying density of the cloud (as discussed in chapter 3.3).

In both cases, the dephasing rate may be calculated by considering the time evolution of the $|W\rangle$ state and calculating the overlap with the initial state (in complete analogy to the calculation of thermal dephasing in section 1.2). However, we now use the weighed $|W\rangle$ state

$$|W\rangle = \sum_{i=1}^{N} \sqrt{P_i}\, |g_1, \ldots, r_i, \ldots, g_N\rangle$$

which is a further generalization of eq. 4.1. It is identical with eq. 4.1 for $P_i = \Omega_{R,i}^2/\sqrt{\sum_{j=1}^{N}\Omega_{R,j}^2}$. We first calculate the overlap in this generalized case, and then explain the reasoning for the generalization.

If the ground to Rydberg state transition of atom i is shifted by the energy ΔE_i, the time-evolved state is

$$|\psi(t)\rangle = \sum_{i=1}^{N} \sqrt{P_i} e^{i(E+\Delta E_i)t/\hbar}\, |g_1, \ldots, r_i, \ldots, g_{N_b}\rangle$$

and the overlap is

$$
\begin{aligned}
|\langle W|\psi(t)\rangle|^2 &= \left|\sum_{i=1}^{N}\sqrt{P_i}e^{-iEt/\hbar}\langle g_1,\ldots,r_i,\ldots,g_N|\sum_{j=1}^{N}\sqrt{P_i}e^{i(E+\Delta E_i)t/\hbar}|g_1,\ldots,r_j,\ldots,g_N\rangle\right|^2 \\
&= \left|\sum_{i=1}^{N}P_i e^{i\Delta E_i t/\hbar}\right|^2
\end{aligned}
\tag{4.2}
$$

which may be calculated numerically.

The generalization of the weights of the collective excited state is necessary to take into account lineshifts that are so large that the exciting lasers are not close to resonance. An atom with such a large lineshift does not participate in the collective state. For the natural FWHM linewidth Γ of the transition, this reduced excitation probability for atoms whose transition is shifted out of resonance with the exciting lasers is modeled using the natural lineshape

$$
P_i \propto \frac{1}{1+(2\Delta E_i/(\hbar\Gamma))^2}
$$

which is normalized such that $\sum_{i=1}^{N} P_i = 1$.

If this generalization were not made, the dephasing rate due to inhomogeneous lineshifts would be overestimated, since atoms that in reality do not participate in the collective state would in the calculation lead to large dephasing because of their large lineshifts.

In the extreme case, in an infinitely large cloud in an optical trap in which the lineshift grows from the center, where there is excitation light in the location of all atoms, a calculation without the adjusted weight would predict an infinite dephasing rate, when in reality the atoms sitting further from the trap center than a certain distance would just not be excited.

For the dephasing rate contribution by differential light shifts, eq. 4.2 is evaluated numerically with $\Delta E_i = U_r - U_g$.

Similarly for the contribution due to inhomogeneous density shifts, eq. 4.2 is evaluated numerically with the density shift from ref. [11] $\Delta E_i = \frac{2\pi\hbar^2 a}{m_e}\overline{n}_i$ with $a = -15.7a_0$. Here,

$$
\overline{n}_i = \int \mathrm{d}^3 r\, |\psi_n(\vec{r})|^2 n(\vec{r}-\vec{r}_i)
$$

is the effective ground state atom density for the atom i located at $\vec{r}_i$, which is the ground state atom density weighed by the Rydberg electron wavefunction.

To do this calculation efficiently numerically, the Rydberg electron probability density is calculated on a fine grid (grid spacing below a_0), and the grid is made coarser to match the spacing of the grid on which the densities are calculated, because calculating the entire density distribution on a grid fine enough to capture the fine features of the Rydberg electron probability density is infeasible. This is done by summing all the grid sites of the finer grid within each grid site of the coarser grid. This results in a kernel that may be convoluted with the density distribution to find the effective density distribution. An example of such a kernel is shown in figure 4.2.

For $n = 100$, the radius of the Rydberg wavefunction is about 1 µm, which is larger than the spacing of lattice sites, so not taking this into account would lead to overestimating the dephasing due to density

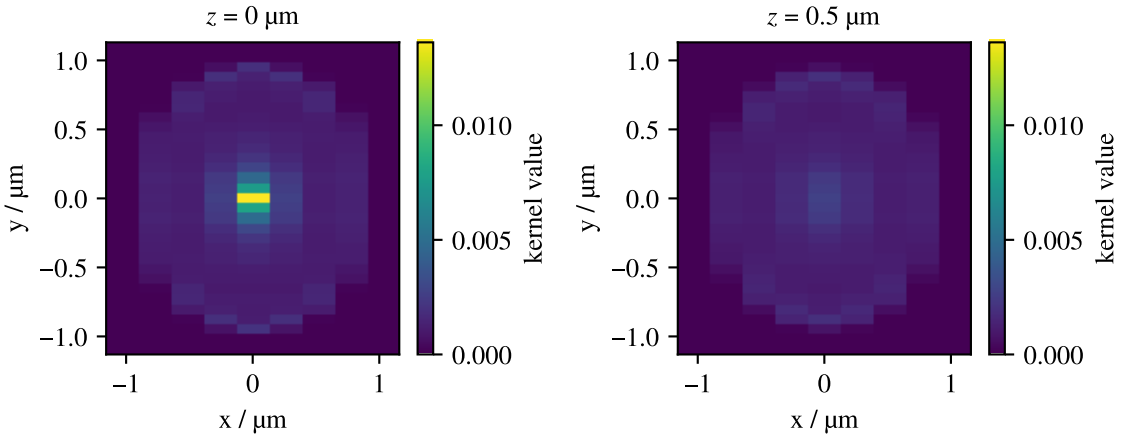

Figure 4.2: Cuts through the 3D convolution kernel given by the probability density of the Rydberg electron at $n = 100$. The kernel has been computed for a grid with different spacings in the y- and x-/z-directions.

inhomogeneities, since the Rydberg wavefunction smoothes out the small-scale variations of the density distribution and reduces its variance.

In figure 4.3, intermediate results of the dephasing rate calculation are shown for the dimple and lattice dimple measurement configurations: The density given by the Boltzmann distribution is shown in the first row. The cloud is smaller in the y-direction than it appears on absorption images. This may be due to the dimple trapping beam waist in the y-direction being larger in reality than is assumed in the calculation. The inhomogeneity of the density in the lattice dimple is clearly much larger than in the dimple, but the effective density is smoothed by the Rydberg wavefunctions for $n = 89$ and $n = 94$. This leads to a reduced variance of the density shifts, which are proportional to the effective density, in the region where the atoms are actually excited, which is given by the weight factor shown in the figure. The differential light shift, whose contributions are weighed with this same factor, is also shown, and it is much reduced in the lattice dimple compared to the regular dimple, especially in the heavily weighed regions, since the optimal lattice detuning as determined in chapter 2 is used.

4.2.4 Rydberg molecules

The formation of molecular states involving one Rydberg atom and one or multiple ground state atoms with small binding energies leads to a broadening of the Rydberg line [11]. This should lead to dephasing, but the contribution is impossible to separate from the density-dependent dephasing due to inhomogeneous density shifts when varying the density in a single trap geometry, as done in the measurements in section 3.3 or in ref. [40]. For this reason, no quantitative estimate of this dephasing rate is made.

4.2.5 Admixture of fast-decaying states

The decay rate Γ of the Rydberg state is increased from its natural decay rate by blackbody-radiation induced decay to adjacent Rydberg states, and by the admixture of the $|e\rangle$ and $|a\rangle$ states by control and

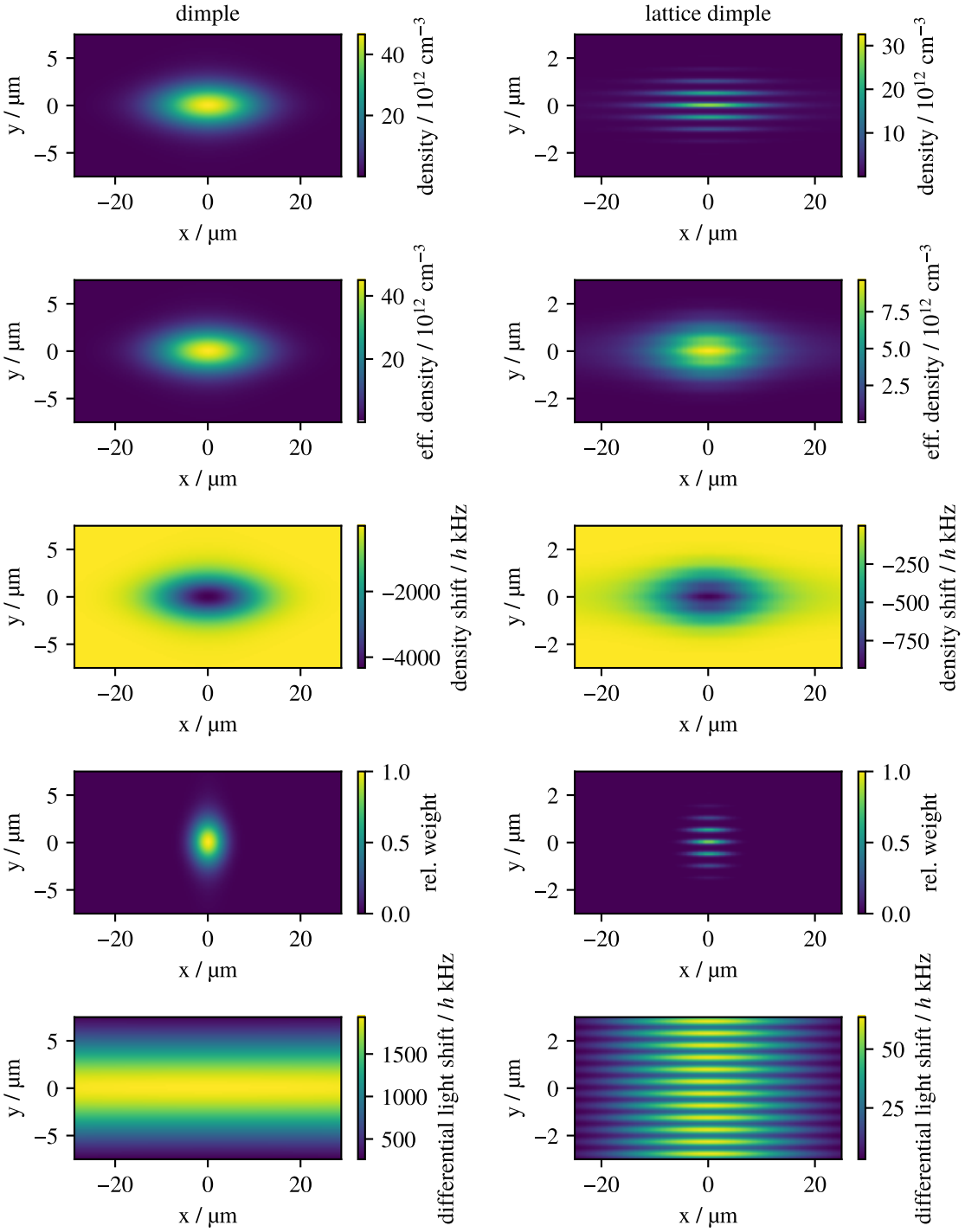

Figure 4.3: Cuts through the full 3D calculated density (first row), effective density (second row), density shift (third row), weight P_i times density (fourth row), and differential light shifts (fifth row) for the cloud in the dimple trap (left column) and the cloud loaded from the dimple trap into the lattice trap (right column).

trap light, respectively. The natural and blackbody decay rates are calculated using the ARC Python package [25].

The admixture of the states $|a\rangle$ and $|e\rangle$ is considered individually by looking at the eigenstates of a two-level system driven with a laser detuned by Δ from the transition leading to a coupling with Rabi frequency Ω. These eigenstates are $|+\rangle = \sin\theta\,|e\rangle + \cos\theta\,|r\rangle$ and $|-\rangle = \cos\theta\,|e\rangle - \sin\theta\,|r\rangle$, with $\tan(2\theta) = -\Omega/\Delta$ [26]. For small Ω/Δ, which is the case for both the trap and the control laser, the state $|+\rangle$ is close to the Rydberg state, $|+\rangle \approx |r\rangle - \frac{\Omega}{2\Delta}|e\rangle$. The total decay rate of the Rydberg state is then given by $\Gamma_r + \frac{\Omega^2}{4\Delta^2}\Gamma_e$.

For the two states $|e\rangle$ and $|a\rangle$, we thus have an increase of the Rydberg level decay rate by $\frac{\Omega_c^2}{4\Delta_c^2}\Gamma_e$ and $\frac{\Omega_t^2}{4\Delta_t^2}\Gamma_a$.

4.2.6 Comparison with measured data

The calculation described in the previous section is carried out numerically for our trap potentials, beam geometries, atom numbers, and temperatures, for the dimple trap and the lattice dimple trap. Because the atom number measurements have been found to be unreliable in section 3.1, the atom number is adjusted to match the measured κ. The results are summarized in figure 4.4. The spikes of the inhomogeneous density shift are due to the discrete calculation, which leads to a large number of grid sites where the density shift is zero, which in combination with the center trap region, where the density shift is largest, lead to a beating of the overlap at the frequency of the largest density shift. The size of these oscillations is reduced when increasing the resolution of the grid, but increasing it much further was impractical.

Both for the dimple and the lattice dimple, dephasing due to inhomogeneous density shifts is the dominant dephasing mechanism at the densities used for superatoms. This is consistent with the experiment, where the density in photon storage experiments had to be reduced to make the differential light shifts the dominant dephasing mechanism. In the dimple, differential light shifts also give a significant contribution to the dephasing rate, while in the lattice, which is tuned to the optimal trap detuning, they do not. It must be noted that the size of the cloud in the y-direction in the calculation as shown in figure 4.3 is smaller than what is observed using absorption imaging, indicating that the inhomogeneity of the density of the cloud is likely overestimated. This may lead to an overestimate of the density dephasing rate.

The expected Rydberg decay rates are much smaller than the dephasing rate, and dominated by the admixture of the $|e\rangle$ state by the control laser. This could be reduced by using more laser power at a larger single-photon detuning, but the contribution compared to γ_D is insignificant.

For the dimple, the calculated decay rate of $\Gamma = 0.07\,\mathrm{MHz}$ is smaller than the measured decay rate $\Gamma = (0.41 \pm 0.01)\,\mathrm{MHz}$, and the calculated dephasing rate $\gamma_D = 2.8\,\mathrm{MHz}$ (ignoring the spikes due to numerical problems) is larger than the measured dephasing rate $\gamma_D = (2.11 \pm 0.05)\,\mathrm{MHz}$. For β_{coh}, the sum $\gamma_D + \Gamma$ is relevant. The calculation of the sum of 2.87 MHz and the measurement of $(2.52 \pm 0.06)\,\mathrm{MHz}$ do not quite agree. A detailed estimate of the errors of the calculation based on how well-known the input parameters are, has not been performed. However, it seems reasonable that the discrepancy can be explained by uncertainties of atom numbers and beam waists.

For the lattice dimple, the quality of the measured data is insufficient to expect detailed agreement with the calculation, however the calculation does show that for an atom number of $N = 1 \times 10^4$ giving $\kappa = 0.12\,\mathrm{MHz}$, the dephasing rate is already a third of that obtained for $\kappa = 0.8\,\mathrm{MHz}$ in the dimple,

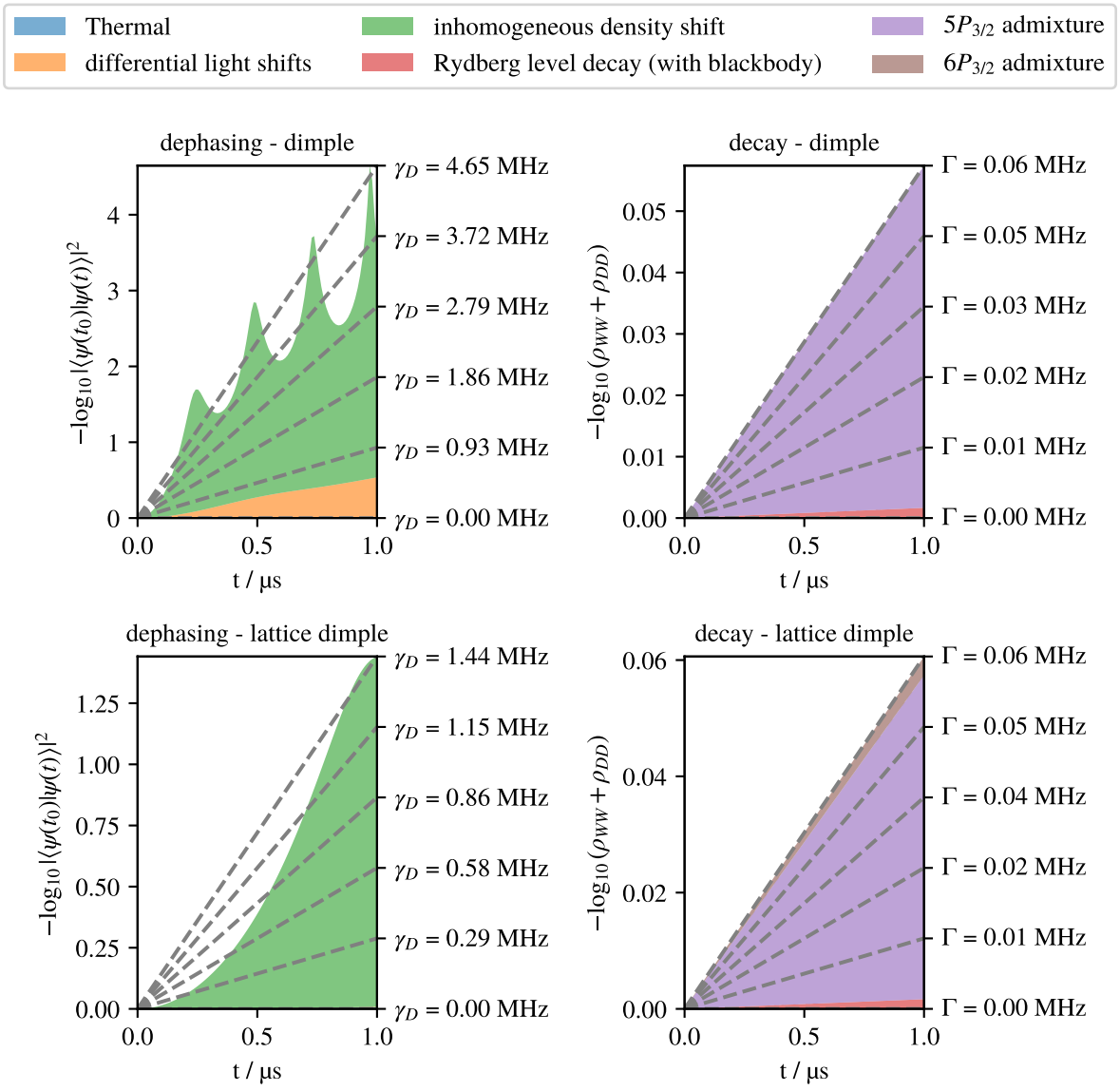

Figure 4.4: Calculation of dephasing rates and decay rates due to different mechanisms for our experimental conditions in the dimple and lattice dimple configurations. The dephasing is given as the overlap of the bright state at time t with the time-evolved initial state. The time-evolution for different dephasing mechanisms is calculated separately and the results are stacked in the plot. For the decay rate, the population in the bright and dark singly-excited states is given.

suggesting that the lattice causes an increase of density dephasing for the same κ compared to the dimple trap.

4.3 Conclusion

In this chapter, an attempt at a quantitative prediction of the known fundamental dephasing rates was made. Comparison to measurements indicates that the discussed dephasing mechanisms may be sufficient to explain the observed dephasing rates, however the confidence in the parameters used for the calculations and in the measurements in the lattice dimple is not high enough to be able to make a definite conclusion on whether the observed dephasing rates are due to under our experimental conditions unavoidable contributions, or whether there is significant technical noise impacting the dephasing rate.

One possible candidate for the latter that has been observed to cause dephasing of Rabi oscillations over a few µs is laser phase noise, which can be reduced using a filtering cavity [41, 42, 42].

CHAPTER 5

Summary and outlook

In this thesis, the suitability of a 1D magic lattice trap for increasing the coherence time of single-photon Rabi oscillations of Rydberg superatoms was characterized. The characterization involved a detailed investigation of three different effects leading to dephasing of the collective bright state of a Rydberg superatom: Differential light shifts in the lattice trap, thermal movement of the atoms, and density-dependent effects, namely the formation of Rydberg molecules and inhomogeneous broadening of the Rydberg line due to density-dependent shifts.

The main result of the investigation of differential light shifts in the lattice trap is the measurement of trap-geometry dependent optimal trap detunings over a wide range of principal quantum numbers of the Rydberg state. The results are in good agreement with calculations of the trap potential that take into account the large extent of the Rydberg electron wavefunction. In this calculation, it was possible to express the geometry-dependence of the trap potential in a very simple and generally applicable way: The geometry-dependent part of the trap potential for the Rydberg state is the average of the ponderomotive potential of the free electron over the Rydberg electron probability density. Such an average is easily evaluated numerically for any trap potential without requiring long analytical calculations, e.g. for a tweezer in appendix C.

Motional rephasing in the magic wavelength lattice could be observed in a photon storage experiment, in agreement with a very simple model of classical motion of atoms in the lattice sites. However, a trade-off between a reduction of thermal dephasing, requiring tight confinement of the atoms, and an increase of density-dependent dephasing, which for a constant number of atoms is reduced at less tight confinement, was identified. At a principal quantum number of $n = 61$, photon storage experiments showed the presence of weakly bound molecular states of Rydberg atoms and ground state atoms.

An attempt was made to characterize the density-dependent dephasing rate at higher principal quantum numbers, which are relevant for Rydberg superatoms, but this measurement did not lead to conclusive results due to inaccurate atom number measurements with absorption imaging.

Finally, a quantitative comparison of different dephasing mechanisms for our experimental conditions was performed. Due to numerical problems and the strong dependence on the waist size of a beam and the overall atom number, the calculations only permit the conclusion that density-dependent dephasing is by far the largest contribution to the overall dephasing rate in the lattice, and that the only other relevant contribution in the dimple are differential light shifts, which are still smaller than the density effects. No improvement of single-photon Rabi oscillations in the magic wavelength lattice could be observed.

A reduction of the dephasing rate of Rydberg superatoms using a lattice trap seems unlikely due to

the increased density compared to a non-lattice trap at constant atom number. However, depending on whether the main contribution to density-dependent dephasing is due to molecular broadening or due to density-shifts, it might be possible to reduce the density-dependent dephasing rate in a cloud with very homogeneous density, trapped e.g. using a flat-top beam or repulsive light sheets. Such a trap would also reduce dephasing due to inhomogeneous differential light shifts, because its intensity would be homogeneous over the volume of the atom cloud. Choosing the right trap will certainly require a detailed quantitative understanding of density-dependent dephasing mechanisms. To check and calibrate such models, some improvements of the absorption imaging system such as intensity stabilization of the imaging laser would have to be implemented in the experiment, to make accurate measurements of the cloud density.

Furthermore, in this thesis only fundamentally unavoidable dephasing mechanisms were investigated in detail, but there could also be relevant technical sources of dephasing, such as laser phase noise. Making sure that these are not limiting factors is another viable path towards possible improvement of the dephasing rate.

APPENDIX A

Perturbation theory for Floquet states

To find the first-order corrections to the quasi-energies, we expand $q_\beta = q_\beta^{(0)} + q_\beta^{(1)}$, and the probability amplitudes as $F_{\alpha\beta}^n = F_{\alpha\beta}^{n(0)} + F_{\alpha\beta}^{n(1)}$. Here the upper indices in brackets give the size in powers of the size of V. One could also make this explicit by introducing a scale λ for V, then $x^{(i)}$ would correspond to a term of order λ^i. Keeping only terms up to first order in equation 2.7, we obtain

$$(q_\beta^{(0)} - E_\alpha^{(0)})F_{\alpha\beta}^{n(0)} + (q_\beta^{(0)} - E_\alpha^{(0)})F_{\alpha\beta}^{n(1)} - n\omega(F_{\alpha\beta}^{n(0)} + F_{\alpha\beta}^{n(1)}) + q_\beta^{(1)}F_{\alpha\beta}^{n(0)} = \sum_{\gamma,k} V_{\alpha\gamma}^{n-k}F_{\gamma\beta}^{k(0)}$$

To zeroth order, the states are not perturbed, so we set $F_{\alpha\beta}^{n(0)} = \delta_{\alpha\beta}\delta_{n0}$, i.e. without a time-dependent perturbation, only the static Fourier component of the unperturbed state is 1, all other probability amplitudes are 0. Also, without a perturbation the quasi-energies are identical with the unperturbed energies, $q_\beta^{(0)} = E_\beta^{(0)}$.

We first look at the case of $\alpha = \beta$:

$$-n\omega(\delta_{n,0} + F_{\beta\beta}^{n(1)}) + q_\beta^{(1)}\delta_{n,0} = \sum_{\gamma,k} V_{\beta\gamma}^{n-k}F_{\gamma\beta}^{k(0)}$$

For the case $n = 0$ we obtain the first-order quasi-energy correction:

$$q_\beta^{(1)} = V_{\beta\beta}^0 \tag{A.1}$$

For the case $n \neq 0$, we find the correction to the probability amplitude of the state itself.

$$-n\omega F_{\beta\beta}^{n(1)} = V_{\beta\beta}^0$$

$$F_{\beta\beta}^{n(1)} = -\frac{V_{\beta\beta}^0}{n\omega}$$

Now we look at the case $\alpha \neq \beta$:

$$(q_\beta^{(0)} - E_\alpha^{(0)})F_{\alpha\beta}^{n(1)} - n\omega F_{\alpha\beta}^{n(1)} = V_{\alpha\beta}^n$$

We obtain the correction to the probability amplitudes for $\alpha \neq \beta$:

$$F^{n(1)}_{\alpha\beta} = \frac{V^n_{\alpha\beta}}{E^{(0)}_\beta - E^{(0)}_\alpha - n\omega}$$

Now, we proceed to the second order. We start again from equation 2.7

$$(q_\beta - E^{(0)}_\alpha - n\omega)F^n_{\alpha\beta} = \sum_{\gamma,k} V^{n-k}_{\alpha\gamma} F^k_{\gamma\beta}, \qquad \text{(2.7 repeated)}$$

this time inserting corrections up to second order, $q_\beta = q^{(0)}_\beta + q^{(1)}_\beta + q^{(2)}_\beta$, and $F^n_{\alpha\beta} = F^{n(0)}_{\alpha\beta} + F^{n(1)}_{\alpha\beta} + F^{n(2)}_{\alpha\beta}$, and keeping terms up to second order:

$$\begin{aligned}(q^{(0)}_\beta - E^{(0)}_\alpha)F^{n(0)}_{\alpha\beta} + (q^{(0)}_\beta - E^{(0)}_\alpha)F^{n(1)}_{\alpha\beta} + (q^{(0)}_\beta - E^{(0)}_\alpha)F^{n(2)}_{\alpha\beta} \\ + q^{(1)}_\beta F^{n(0)}_{\alpha\beta} + q^{(1)}_\beta F^{n(1)}_{\alpha\beta} + q^{(2)}_\beta F^{n(0)}_{\alpha\beta} - n\omega(F^{n(0)}_{\alpha\beta} + F^{n(1)}_{\alpha\beta} + F^{n(2)}_{\alpha\beta}) \\ = \sum_{\gamma,k} V^{n-k}_{\alpha\beta} F^{k(0)}_{\gamma\beta} + \sum_{\gamma,k} V^{n-k}_{\alpha\gamma} F^{k(1)}_{\gamma\beta}\end{aligned}$$

Looking only at the terms of second order:

$$(q^{(0)}_\beta - E^{(0)}_\alpha)F^{n(2)}_{\alpha\beta} + q^{(1)}_\beta F^{n(1)}_{\alpha\beta} + q^{(2)}_\beta F^{n(0)}_{\alpha\beta} - n\omega F^{n(2)}_{\alpha\beta} = \sum_{\gamma,k} V^{n-k}_{\alpha\gamma} F^{k(1)}_{\gamma\beta}$$

We first look at the case $\alpha = \beta$, and insert $q^{(0)}_\beta = E^{(0)}_\beta$, $F^{n(0)}_{\alpha\beta} = \delta_{\alpha\beta}\delta_{n0}$, and from the first order calculation $q^{(1)}_\beta = V^0_{\beta\beta}$ and $F^{n(1)}_{\alpha\beta} = \frac{V^n_{\alpha\beta}}{E^{(0)}_\beta - E^{(0)}_\alpha - n\omega}$.

$$\begin{aligned}q^{(1)}_\beta F^{n(1)}_{\beta\beta} + q^{(2)}_\beta F^{n(0)}_{\beta\beta} - n\omega F^{n(2)}_{\beta\beta} &= \sum_{\gamma,k} V^{n-k}_{\beta\gamma} F^{k(1)}_{\gamma\beta} \\ V^0_{\beta\beta} F^{n(1)}_{\beta\beta} + q^{(2)}_\beta \delta_{n,0} &= \sum_{\gamma,k} V^{n-k}_{\beta\gamma} \frac{V^k_{\gamma\beta}}{E^{(0)}_\beta - E^{(0)}_\gamma - k\omega}\end{aligned}$$

We do not know what $F^{0(0)}_{\beta\beta}$ is from the equations looked at so far, so it has to be determined from the normalization of the wavefunction, set it to zero (see LL for argument?). We use the fact that V is Hermitian, $V_{\alpha\beta} = V^*_{\beta\alpha}$ and that the Fourier components obey $V^k = (V^{-k})^*$ to obtain

$$q^{(2)}_\beta = \sum_{\gamma,k} \frac{(V^k_{\gamma\beta})^2}{E^{(0)}_\beta - E^{(0)}_\gamma - k\omega} \tag{A.2}$$

APPENDIX B

Four-level Hamiltonian in rotating frame in dipole and rotating wave approximation

In this case, the interaction Hamiltonian is given by the dipole interaction energy, $H_{AF} = -\vec{d} \cdot \vec{E}$, with the dipole operator $\hat{\vec{d}}$. The electric field is the sum of the three laser fields at the location of the atoms, $E_i(t) = \mathcal{E}_i \cos(\omega_i t)$ $(i = p, c, t)$. Because only the probe field is σ^+-polarized, it is the only one for which the relevant dipole matrix elements between states $|g\rangle$ and $|e\rangle$ are nonzero. Similarly, only the σ^--polarized control and lattice fields can drive the $|e\rangle$ to $|r\rangle$ and $|a\rangle$ to $|r\rangle$ transitions. Instead of explicitly calculating this, we immediately apply these selection rules and write the atom-field Hamiltonian (with real dipole matrix elements)

$$\begin{pmatrix} 0 & -d_{ge}\mathcal{E}_p \cos(\omega_p t) & 0 & 0 \\ -d_{ge}\mathcal{E}_p \cos(\omega_p t) & E_e & 0 & -d_{er}(\mathcal{E}_c \cos(\omega_c t) + \mathcal{E}_t \cos(\omega_t t)) \\ 0 & 0 & E_a & -d_{ar}(\mathcal{E}_t \cos(\omega_t t) + \mathcal{E}_c \cos(\omega_c t)) \\ 0 & -d_{er}(\mathcal{E}_c \cos(\omega_c t) + \mathcal{E}_t \cos(\omega_t t)) & -d_{ar}(\mathcal{E}_t \cos(\omega_t t) + \mathcal{E}_c \cos(\omega_c t)) & E_r \end{pmatrix}$$

We now want to change to a rotating frame, and will use the unitary transformation

$$U = \begin{pmatrix} 1 & 0 & 0 & 0 \\ 0 & e^{i\omega_p t} & 0 & 0 \\ 0 & 0 & e^{i(\omega_p+\omega_c-\omega_t)t} & 0 \\ 0 & 0 & 0 & e^{i(\omega_p+\omega_c)t} \end{pmatrix}$$

The Hamiltonian in the rotating frame is given by

$$\tilde{H} = UHU^\dagger + i\hbar \frac{dU}{dt} U^\dagger$$

Calculating this yields:

$$\hat{H} = \begin{pmatrix} 0 & -d_{ge}(e^{-2i\omega_p t}+1)\mathcal{E}_p & 0 & 0 \\ -d_{ge}(e^{-2i\omega_p t}+1) & E_2 - \hbar\omega_p & 0 & -d_{er}((e^{-2i\omega_c t}+1)\mathcal{E}_c + (e^{-i(\omega_c+\omega_t)t} + e^{i(\omega_t-\omega_c)t})\mathcal{E}_l) \\ 0 & 0 & 0 & -d_{er}((e^{-2i\omega_c t}+1)\mathcal{E}_c + (e^{-i(\omega_c+\omega_t)t} + e^{i(\omega_t-\omega_c)t})\mathcal{E}_t) \\ 0 & -d_{er}((e^{-2i\omega_c t}+1)\mathcal{E}_c + (e^{-i(\omega_c+\omega_t)t} + e^{i(\omega_t-\omega_c)t})\mathcal{E}_t) & E_a - \hbar(\omega_c-\omega_t+\omega_p) & -d_{ar}((e^{i(\omega_c-\omega_t)t} + e^{-i(\omega_c+\omega_t)})\mathcal{E}_c + (1+e^{-2i\omega_l t})\mathcal{E}_t) \\ 0 & -d_{er}((e^{-2i\omega_c t}+1)\mathcal{E}_c + (e^{-i(\omega_c+\omega_t)t} + e^{i(\omega_t-\omega_c)t})\mathcal{E}_t) & -d_{ar}((e^{i(\omega_c-\omega_t)t} + e^{-i(\omega_c+\omega_t)})\mathcal{E}_c + (1+e^{-2i\omega_l t})\mathcal{E}_t) & E_r - \hbar(\omega_c+\omega_p) \end{pmatrix}$$

Dropping all the terms oscillating at optical frequencies (rotating wave approximation), and substituting

$$\begin{aligned} \hbar\Delta_p &= \hbar\omega_p - E_e \\ \hbar\Delta_c &= \hbar\omega_c - (E_r - E_e) \\ \hbar\Delta_t &= \hbar\omega_t - (E_r - E_a) \end{aligned}$$

as well as

$$\begin{aligned} \Omega_{ge} &= -2d_{ge}\mathcal{E}_p/\hbar \\ \Omega_{er} &= -2d_{er}\mathcal{E}_c/\hbar \\ \Omega_{ar} &= -2d_{ar}\mathcal{E}_t/\hbar \end{aligned}$$

we obtain

$$\tilde{H} = -\hbar \begin{pmatrix} 0 & \Omega_{ge}/2 & 0 & 0 \\ \Omega_{ge}/2 & \Delta_p & 0 & \Omega_{er}/2 \\ 0 & 0 & \Delta_p + \Delta_c - \Delta_t & \Omega_{ar}/2 \\ 0 & \Omega_{er}/2 & \Omega_{ar}/2 & \Delta_c + \Delta_p \end{pmatrix}$$

APPENDIX C

Trapping potential for Rydberg atoms in tweezers

The geometry dependence of the trap potential for Rydberg atoms discussed in chapter 2 applies to any optical trap whose intensity changes significantly over distances smaller than the size of a Rydberg atom. One example of such a trap is a tightly focused Gaussian beam forming an optical tweezer. These traps are used in quantum simulation and quantum computation experiments with Rydberg atoms, because they make it possible to create defect-free single atom arrays [43, 44, 45, 46]. To prevent atom loss, tweezers with a repulsive potential for Rydberg atoms have to be turned off when the atoms are excited from ground to Rydberg states (done e.g. in ref. [45]).

If one wanted to use magic tweezers at the same wavelength as the standing wave trap discussed in this thesis, it would not be possible to find a wavelength where the potentials for the ground and Rydberg states become completely equal. The potential difference for such a tweezer with a power of 1 mW and a waist of 1 µm, which leads to a trap depth of approximately 1 mK, is shown in figure C.1, along with the standard deviation of the differential light shift for an atom at a temperature of 50 µK. The potentials for the ground and Rydberg state are never perfectly equal everywhere, but can be minimized for the atoms trapped in the tweezer. The minimal standard deviation of the light shift is 20 kHz.

The potentials were calculated numerically according to eqs. 2.12 and 2.13, by convolving the 3D intensity distribution with a kernel containing the probability density of the Rydberg electron.

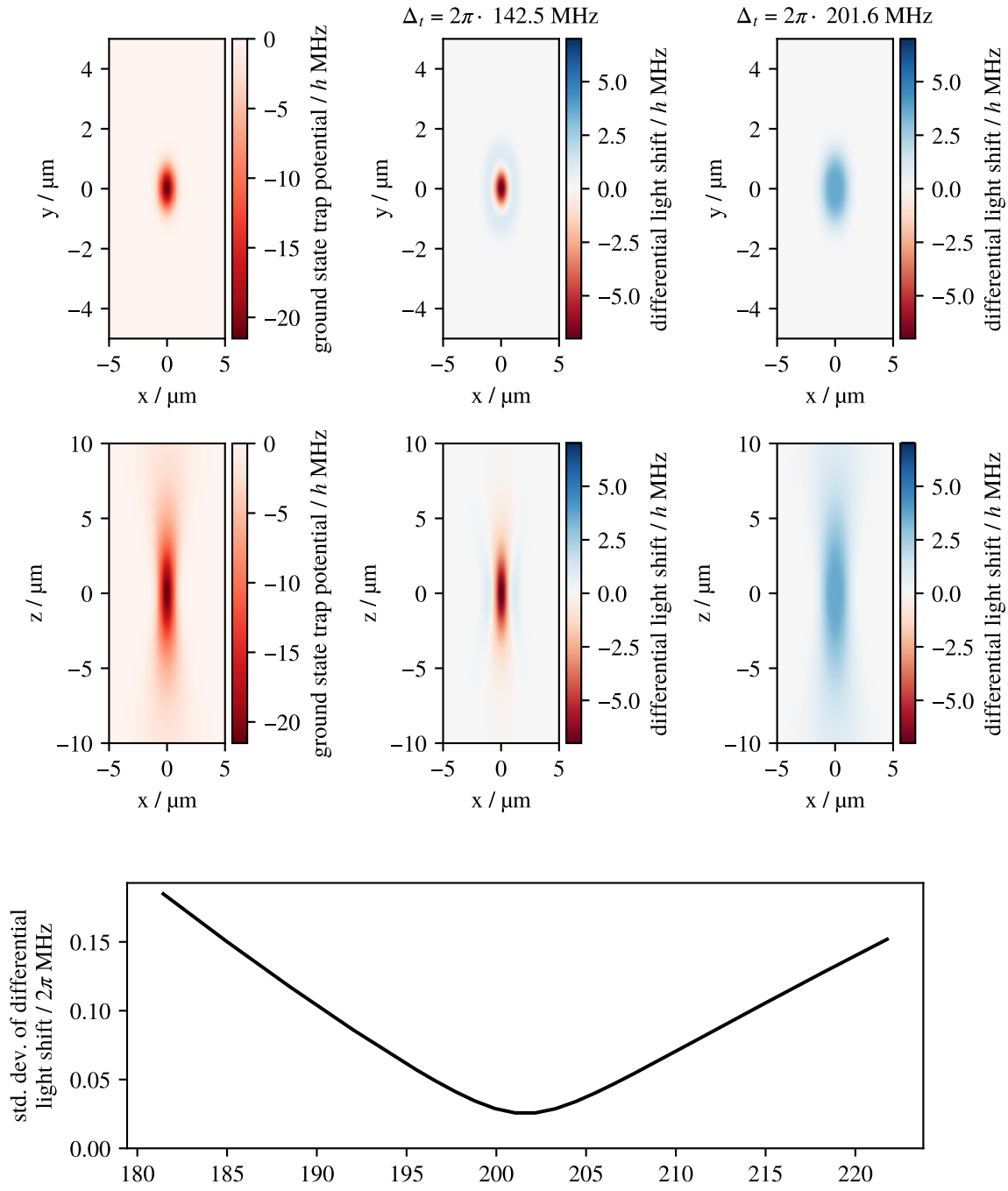

Figure C.1: Differential trapping potentials between the ground state $|g\rangle$ and the Rydberg state $|r_n\rangle$ for $n = 100$ in a magic tweezer with a waist of 1 µm at 1012 nm. The left top two panels show the ground state trap potentials for the tweezer formed by a Gaussian beam propagating along the z-axis. The center panels show the differential light shifts at a trap detuning of $\Delta_t = 2\pi \cdot 142.5\,\text{MHz}$, which is the magic detuning for a trap that does not contain any significant intensity variations over the size of a Rydberg atom. The top right panels show the differential light shifts for $\Delta_t = 2\pi \cdot 201.6\,\text{MHz}$, which minimizes the differential light shifts for an atom at 50 µK. The bottom panel shows the standard deviation of the differential light shift weighed by the thermal distribution of atoms in the tweezer around the optimal trap detuning.

Bibliography

[1] A. Paris-Mandoki et al., *Free-Space Quantum Electrodynamics with a Single Rydberg Superatom*, Physical Review X **7** (2017) 041010.

[2] J. Kumlin et al., *Quantum Optics with Rydberg Superatoms*, J. Phys. Commun. **7** (2023) 052001.

[3] M. Saffman, T. G. Walker, and K. Mølmer, *Quantum Information with Rydberg Atoms*, Reviews of Modern Physics **82** (2010) 2313.

[4] Y. O. Dudin, L. Li, F. Bariani, and A. Kuzmich, *Observation of Coherent Many-Body Rabi Oscillations*, Nature Physics **8** (2012) 790.

[5] J. Kumlin, *Collective Effects of Light-Matter Interactions in Rydberg Superatoms*, PhD thesis: Universität Stuttgart, 2021.

[6] M. O. Scully, E. S. Fry, C. H. R. Ooi, and K. Wódkiewicz, *Directed Spontaneous Emission from an Extended Ensemble of N Atoms: Timing Is Everything*, Physical Review Letters **96** (2006) 010501.

[7] M. D. Lukin et al., *Dipole Blockade and Quantum Information Processing in Mesoscopic Atomic Ensembles*, Physical Review Letters **87** (2001) 037901.

[8] D. Manzano, *A Short Introduction to the Lindblad Master Equation*, AIP Advances **10** (2020) 025106.

[9] J. Johansson, P. Nation, and F. Nori, *QuTiP: An Open-Source Python Framework for the Dynamics of Open Quantum Systems*, Computer Physics Communications **183** (2012) 1760.

[10] J. Johansson, P. Nation, and F. Nori, *QuTiP 2: A Python Framework for the Dynamics of Open Quantum Systems*, Computer Physics Communications **184** (2013) 1234.

[11] A. Gaj et al., *From Molecular Spectra to a Density Shift in Dense Rydberg Gases*, Nature Communications **5** (2014) 4546.

[12] I. Mirgorodskiy, *Storage and Propagation of Rydberg Polaritons in a Cold Atomic Medium*, PhD thesis: Universität Stuttgart, 2017.

[13] C. Tresp, *Rydberg Polaritons and Rydberg Superatoms - Novel Tools for Quantum Nonlinear Optics*, PhD thesis: University of Stuttgart, 2017.

[14] H. M. Gorniaczyk,
Single Photon Transistor Mediated by Electrically Tunable Rydberg-Rydberg Interactions,
PhD thesis: University of Stuttgart, 2016.

[15] F. Christaller, *Construction and Setup of a 3rd Generation Rydberg Quantum Optics Experiment*,
MA thesis: University of Stuttgart, 2017.

[16] C. Tresp et al., *Single-Photon Absorber Based on Strongly Interacting Rydberg Atoms*,
Physical Review Letters **117** (2016) 223001.

[17] J. R. Boon, E. Zekou, D. McGloin, and M. H. Dunn, *Comparison of Wavelength Dependence in Cascade-, L-, and Vee-type Schemes for Electromagnetically Induced Transparency*,
Physical Review A **59** (1999) 4675.

[18] R. Grimm, M. Weidemüller, and Y. B. Ovchinnikov, *Optical Dipole Traps for Neutral Atoms*,
1999, arXiv: physics/9902072, pre-published.

[19] J. Lampen, H. Nguyen, L. Li, P. R. Berman, and A. Kuzmich,
Long-Lived Coherence between Ground and Rydberg Levels in a Magic-Wavelength Lattice,
Physical Review A **98** (2018) 033411.

[20] T. Topcu and A. Derevianko, *Dynamic Polarizability of Rydberg Atoms: Applicability of the near-Free-Electron Approximation, Gauge Invariance, and the Dirac Sea*,
Physical Review A **88** (2013) 042510.

[21] J. H. Shirley, *Interaction of a Quantum System with a Strong Oscillating Field*, 1963.

[22] J. H. Shirley, *Solution of the Schrödinger Equation with a Hamiltonian Periodic in Time*,
Physical Review **138** (4B 1965) B979.

[23] L. D. Landau and E. M. Livshitz, *Quantum Mechanics*, vol. 3, 10 vols.,
Course of Theoretical Physics, Pergamon Press, 1977.

[24] K. Rzążewski and R. W. Boyd,
Equivalence of Interaction Hamiltonians in the Electric Dipole Approximation,
Journal of Modern Optics **51** (2004) 1137.

[25] N. Šibalić, J. Pritchard, C. Adams, and K. Weatherill,
ARC: An Open-Source Library for Calculating Properties of Alkali Rydberg Atoms,
Computer Physics Communications **220** (2017) 319.

[26] D. Steck, *Quantum and Atom Optics (Revision 0.14, 23 August 2023)*, 2023.

[27] M. Fleischhauer, A. Imamoglu, and J. P. Marangos,
Electromagnetically Induced Transparency: Optics in Coherent Media,
Reviews of Modern Physics **77** (2005) 633.

[28] R. Löw et al., *An Experimental and Theoretical Guide to Strongly Interacting Rydberg Gases*,
Journal of Physics B: Atomic, Molecular and Optical Physics **45** (2012) 113001.

[29] L. V. Hau, S. E. Harris, Z. Dutton, and C. H. Behroozi,
Light Speed Reduction to 17 Metres per Second in an Ultracold Atomic Gas,
Nature **397** (1999) 594.

[30] C. Liu, Z. Dutton, C. H. Behroozi, and L. V. Hau, *Observation of Coherent Optical Information Storage in an Atomic Medium Using Halted Light Pulses*, Nature **409** (2001) 490.

[31] T. M. Brzozowski, M. Maczynska, M. Zawada, J. Zachorowski, and W. Gawlik, *Time-of-Flight Measurement of the Temperature of Cold Atoms for Short Trap-Probe Beam Distances*, Journal of Optics B: Quantum and Semiclassical Optics **4** (2002) 62.

[32] G. Reinaudi, T. Lahaye, Z. Wang, and D. Guéry-Odelin, *Strong Saturation Absorption Imaging of Dense Clouds of Ultracold Atoms*, Opt. Lett. **32** (2007) 3143.

[33] V. Bendkowsky et al., *Observation of Ultralong-Range Rydberg Molecules*, Nature **458** (2009) 1005.

[34] I. Mirgorodskiy et al., *Electromagnetically Induced Transparency of Ultra-Long-Range Rydberg Molecules*, Physical Review A **96** (2017) 011402.

[35] F. Böttcher et al., *Observation of Mixed Singlet-Triplet Rb 2 Rydberg Molecules*, Physical Review A **93** (2016) 032512.

[36] F. Schwabl, *Quantenmechanik (QM I)*, Berlin Heidelberg: Springer Verlag, 2005.

[37] U. M. Ascher and L. R. Petzold, *Computer Methods for Ordinary Differential Equations & Differential-Algebraic Equations*, SIAM, 1998.

[38] P. Virtanen et al., *SciPy 1.0: Fundamental Algorithms for Scientific Computing in Python*, Nature Methods **17** (2020) 261.

[39] M. T. Schlagmüller, *A single Rydberg Atom interacting with a Dense and Ultracold Gas*, PhD thesis: Universität Stuttgart, 2016.

[40] S. Baur, D. Tiarks, G. Rempe, and S. Dürr, *Single-Photon Switch Based on Rydberg Blockade*, Physical Review Letters **112** (2014) 073901.

[41] S. De Léséleuc, D. Barredo, V. Lienhard, A. Browaeys, and T. Lahaye, *Analysis of Imperfections in the Coherent Optical Excitation of Single Atoms to Rydberg States*, Physical Review A **97** (2018) 053803.

[42] L. Li, W. Huie, N. Chen, B. DeMarco, and J. P. Covey, *Active Cancellation of Servo-Induced Noise on Stabilized Lasers via Feedforward*, Physical Review Applied **18** (2022) 064005.

[43] M. Endres et al., *Atom-by-Atom Assembly of Defect-Free One-Dimensional Cold Atom Arrays*, Science **354** (2016) 1024.

[44] D. Barredo, S. De Léséleuc, V. Lienhard, T. Lahaye, and A. Browaeys, *An Atom-by-Atom Assembler of Defect-Free Arbitrary Two-Dimensional Atomic Arrays*, Science **354** (2016) 1021.

[45] P. Scholl et al., *Quantum Simulation of 2D Antiferromagnets with Hundreds of Rydberg Atoms*, Nature **595** (2021) 233.

[46] S. J. Evered et al., *High-Fidelity Parallel Entangling Gates on a Neutral-Atom Quantum Computer*, Nature **622** (2023) 268.

List of Figures

Acknowledgements

Many people have contributed to the work in this thesis. In particular, I would like to thank Lukas, Daniil, and Nina for offering me the opportunity to work at the experiment with them, for teaching me how to run and debug its many intricate parts, for all their guidance and help, and for making every day in the lab a good day. Especially I would like to thank Lukas for allowing me to work with him on the characterization of the magic wavelength lattice he built. I would like to thank Sebastian for the opportunity to work in the group, for his guidance, and also for sending me to the DPG spring meeting and to YAO. I would like to thank Wolfgang for his crystal-clear explanations, Chris Nill for his explanations of the calculation of the trap potential, Simon for the short but nice time working together on the experiment, the entire NQO group, my parents, and all of my friends. Finally, I would like to thank everyone who has proofread parts of this thesis.